The physics of discharge lamps

G. G. Lister*

Osram Sylvania, Beverly, Massachusetts 01915, USA

J. E. Lawler

Department of Physics, University of Wisconsin, Madison, Wisconsin 53706, USA

W. P. Lapatovich and V. A. Godyak

Osram Sylvania, Beverly, Massachusetts 01915, USA

(Published 1 June 2004)

The physics of gas discharge lamps is reviewed, with particular emphasis on new developments in the field. In addition to the most important light sources (fluorescent and high-pressure discharge lamps), a number of less common sources are also discussed. The review covers not only the physics of the discharges themselves, but also their interactions with lamp materials and external driving circuits. Important historical steps in lamp product development are described and special sections are devoted to the properties of light, diagnostics, and modeling of the discharges. A detailed, but not exhaustive, review of the published literature is provided and some possible future directions for research in the subject are discussed.

CONTENTS

*Electronic address: Graeme.Lister@sylvania.com

I. INTRODUCTION

The development of electric lamps dates from the second half of the nineteenth century. The first commercial electric lamps were incandescent light sources, introduced after Thomas Edison in the USA and Joseph Swan in England separately developed a lamp in 1878 in which electric current was passed though a filament made from carbon thread. At that time there was also considerable interest in the use of electrical discharges through mixtures of gaseous vapors (gas discharges) for lighting, but it was not until the 1930s that fluorescent lamps and high-pressure mercury lamps first achieved commercial success. Today there are approximately nine billion incandescent lamps, 4 billion fluorescent lamps and 500 million high-pressure discharge lamps in service around the world. They consume ~25% of worldwide electric energy production.

Gas discharges, the main topic of this article, are used for a variety of lighting applications and cover a wide range of plasma parameters. These discharges include both LTE and non-LTE plasmas, where LTE refers to local thermal equilibrium and implies that the collision frequency between plasma constituents is sufficiently high for all species to be at the same temperature, i.e., the plasma is thermalized. Lighting examples can be found in each of the major classifications of low-temperature plasmas: "thermal" or LTE plasmas (high-intensity discharge or HID lamps) operating at gas pressures of 1–300 atm; low-pressure or non-LTE plasmas (e.g., fluorescent, low-pressure sodium lamps) operating at gas pressures between a few hundred millitorr and a few torr; and "nonthermal" plasmas (dielectric-barrier discharge lamps), operating at pressures of 100 torr to 1 atm.

When an electric current is passed through a gaseous medium, it produces a weakly ionized plasma. Electrical power then both heats the gas, walls, and electrodes of the discharge and gives rise to radiation, some of which escapes from the discharge. Radiation is emitted by atoms and molecules of the gas that have been excited into electronic levels above the ground state and then lose their energy by radiative decay to lower electronic levels. The fraction of electrical power converted to visible radiation, either directly or by use of a phosphor, determines the efficiency or *luminous efficacy* of the discharge as a light source (see Sec. II).

The principle of the electric arc was discovered by Humphry Davy around 1802. In 1808, he demonstrated a continuous luminous arc, passing a current in air between two pieces of charcoal. The carbon arc was formed by connecting two carbon electrodes to the terminals of a current source, bringing the two carbon electrodes momentarily together, and then separating them. The bright light formed was due to incandescence of the carbon electrodes.

Although the first observations of electric discharges in rarefied gases date back to the seventeenth century, it was not until the end of the nineteenth century that attempts were made to apply these discharges to lighting. Experiments were conducted with evacuated glass tubes containing small amounts of gases. Nitrogen produced a pinkish light, while the light from discharges in carbon dioxide was close to daylight.

The first low-pressure mercury discharge lamps made use of the greenish-blue visible spectrum of the mercury atom, but the discovery by a group of German scientists in 1926 that the hard ultraviolet (UV) radiation produced by the lamp could be converted to visible light by means of a phosphor led directly to the introduction of the fluorescent lamp in the 1930s. Today, fluorescent lamps (Sec. VI) are used for indoor commercial, industrial, institutional, and retail applications, and it has been estimated that 80% of the world's artificial light is fluorescent (Abeywickrama, 1997).

The first HID lamps, produced in 1906 and now almost obsolete, were arc discharges containing mercury vapor at atmospheric pressure (see Sec. VII). These

lamps also use a phosphor to convert UV to visible light, but the ratio of visible to UV radiation in the discharge is much greater than in a fluorescent lamp, resulting in a bright greenish-blue light suitable only for outdoor applications.

High-pressure sodium (HPS) lamps are produced by adding sodium metal to the mercury lamp. However, the light from these highly efficient lamps is principally the strongly broadened yellow emission from sodium atoms, which also restricts their use to outdoor applications. Efficient "white"-light HID lamps are produced by adding metal halide salts to the mercury lamp. This type of lamp, known as the MH lamp, will be discussed in Sec. VII. Due to their high power, HID lamps are particularly suited to outdoor floodlighting and use on streets and highways while lower-wattage lamps are used for indoor industrial and commercial applications. Mercury lamps operating at very high pressures (150–300 atm) are used for video and data-projection applications.

The quality of a light source is assessed using a set of specifically defined parameters, which are listed in Sec. II. Historically, lamp developers have concentrated on properties required for a particular application—for example, "white" or "natural" light is less important for outdoor applications than for indoor lighting. However, in recent years, highly efficient white-light sources have been developed for most applications.

Fluorescent and HID lamps are by far the most important commercial gas discharge light sources and are thus the main topics of discussion in this article. In order to make the article accessible to as many readers as possible, we have separated the discussions of the underlying physics, diagnostics, theory, and modeling into relatively independent sections. Section III considers the general properties of gas discharge lamps. Sections IV and V discuss how these light sources are measured and modeled. Fluorescent and HID lamps are then analyzed in some detail in Secs. VI and VII, respectively.

While most discharge lamps contain mercury, a number of mercury-free non-LTE gas discharges have been used or investigated. Low-pressure sodium lamps contain sodium vapor and are the most efficient light sources currently available. Unfortunately, the yellow sodium radiation results in very poor color rendition, limiting their use to outdoor applications. Rare-gas discharges emit principally in the vacuum ultraviolet (vuv) at wavelengths $\lambda = 70–170$ nm, and conversion by a phosphor to visible light is inefficient. However, the red line from neon has been used for brake lights on some automobiles. Dielectric-barrier discharges (or silent discharges) have been used since 1850 for ozone and large-scale UV production, and this technology is currently applied to large flat-panel xenon discharges for backlighting of liquid-crystal display (LCD) screens. Mercury-free non-LTE gas discharges for lighting, including recent research activities, are reviewed in Sec. VIII.

II. LIGHT-SOURCE PARAMETERS

Luminous efficacy (hereafter abbreviated to *efficacy*) is defined in terms of the photopic response $V\_$ (i.e., response in bright viewing conditions) of the average eye to light over the visible spectra [380 nm (violet) to 780 nm (red)]. The eye response is a maximum for green light at wavelength 555 nm, and 1 W of radiated power at this wavelength is defined as 683 lm. The spectrum of any light source may thus be measured and folded with the photopic response curve to provide a total lumen output for the lamp. Efficacy of a light source is measured in lm/W, the number of lumens produced per watt of electrical power in the discharge, while system efficacy includes the power dissipated in the mechanisms used to run the lamp, such as the electronic circuit (ballast).

The *correlated color temperature* (CCT) is the temperature of the blackbody whose visual color most closely represents that of the light source and is thus a measure of the appearance of the operating lamp. "Natural" light generally refers to daylight, which has a CCT of 5000–7500 K.

The *color-rendering index* (CRI) is a measure of the degree of change in the *apparent* colors of standardized pigments perceived when they are illuminated by the source in question, in comparison to their apparent colors when they are illuminated by a standard source of a matching CCT. For CCT less than 5000 K, the reference source is a blackbody; for CCT greater than 5000 K, it is a standard daylight source.

Linear fluorescent lamps at a rated power of 40 W have efficacies of 80–100 lm/W, with a CRI between 60 and 85 and a range of CCT from 3000 to 6000 K, depending on the phosphors used. Similar wattage MH lamps produce 85 lm/W with a CRI around 80 and a CCT of 3000 K, while 1000-W high-pressure sodium lamps produce 140 lm/W, but with a CRI of 22 and a CCT of 2000 K. A 60-W incandescent bulb is limited to about 17 lm/W on 110-V electric circuits (at higher voltages lm/W is lower because of lifetime considerations) with a CRI close to 100 and a CCT of 3000 K. For a detailed discussion of these and other parameters used by the lighting industry, see Coaton and Marsden (1997) or Lister and Waymouth (2001).

III. GENERAL PROPERTIES OF DISCHARGE LAMPS

A. Discharge characteristics

1. Electrical characteristics

The electric current density $\vec{j}$ in a discharge is related to the local electric field $\vec{E}$ through the electrical conductivity of the plasma. Lighting discharges are generally unmagnetized and the electrical conductivity may be represented by a scalar quantity σ_e, such that

$$\vec{j} = \sigma_e \vec{E} \tag{3.1}$$

and the discharge current I is the integrated current density passing through a cross section of the lamp, i.e., $I = \int \vec{j} \cdot d\vec{A}$. Since the discharge voltage is simply the

value of the electric field integrated between the lamp electrodes, σ_e determines the relationship between lamp voltage and current.

The electrical conductivity (see Sec. V.F) depends on electron density and the electron momentum-transfer collision frequency with atoms and molecules in the gases in the discharge, ν_m. In standard fluorescent lamps, elastic electron collisions with rare-gas atoms provide the major contribution to ν_m, while electron density is dependent on the mercury vapor pressure. In most HID lamps, the major contribution to ν_m is from electron collisions with mercury atoms, while metal atoms (mercury in mercury lamps, sodium in high-pressure sodium lamps, and metals dissociated from the salts in MH lamps) are the principal source of electron density.

During steady-state operation, most gas discharges have a "negative differential resistance"—as discharge current increases, the voltage required to maintain the discharge decreases. This situation is inherently unstable when driven by a constant-voltage source and would allow the current to grow unimpeded. The electric circuit device that supplies the necessary impedance to restore stability is called a *ballast*. An overview of ballasts used for lighting discharges is given in Sec. III.B, and further details on the use of ballasts for fluorescent and HID lamps are given in Secs. VI.E and VII.E, respectively.

2. Power balance

In all gas discharges, the total electrical power W_{elec} is dissipated through radiation (W_{rad}), heat conduction (W_{heat}), acceleration of ions in the sheaths at the walls and electrodes (W_{sheath}), and diffusion of particles from the discharge (W_{diff}), i.e.,

$$W_{elec} = W_{rad} + W_{heat} + W_{diff} + W_{sheath}. \tag{3.2}$$

Clearly, gas discharges for lighting are designed to maximize the fraction of electrical power leaving the lamp as visible radiation. An overview of the power dissipation mechanisms and their relative importance in discharge lamps is given in the following sections.

3. Radiation mechanisms

The principal processes that contribute to absorption and emission of radiation in the UV and visible regions of the electromagnetic spectrum are electronic transitions of atoms, atomic ions, and molecules. Infrared (IR) emission and absorption arises from transitions between Rydberg levels and from vibrational transitions in molecular species. Recombination of ions and electrons is thought to be responsible for some visible, UV, and IR radiation in HID lamps.

In most electric discharge lamps, emission and absorption by electronic transitions in atoms (and atomic ions in MH lamps) are the dominant processes. Absorption and emission lines in the radiation spectrum from such transitions are usually broadened by a variety of perturbing influences, such as

(a) collisional or pressure broadening due to collisions between radiating and nonidentical perturbing atoms,
(b) collisional Stark broadening from the electric fields of nearby electrons and ions,
(c) collisional resonance broadening as a result of perturbation of an atom radiating to the ground level by an identical atom in the ground level, and
(d) Doppler broadening as a result of thermal motion of the radiating atoms.

As a result of this line broadening, many of the atomic lines are strongly self-reversed. This self-reversal occurs because the radiation emitted at frequencies near line center tends to get reabsorbed by ground-level atoms of the radiating species before it escapes from the discharge, while radiation emitted sufficiently far into the spectral line wings from any part of the discharge freely escapes.

In addition to atomic transitions, electronic, vibrational, and rotational transitions in molecules contribute to absorption and emission in some discharges. Radiation in the extreme wings of atomic lines from high-pressure lamps has a molecular character. Free-free and free-bound transitions of free electrons, which result in absorption and emission of radiation over wide ranges of frequency (continuum emission), are generally less important than other radiation processes in discharge lamps. However, in some lamps bound-free transitions form the basis for visible and UV excimer emissions. Electron-atom bremsstrahlung plays an important role in the ultrahigh-pressure (150–300 atm) lamps used for video and data projection applications.

In general there is a mismatch of indices of refraction at the interface between the discharge gas and the wall, leading to a reflection loss, so that a portion of the internally generated radiation does not escape. In discharge lamps, the reflection losses are relatively small, approximately 4–5 % at each of several surfaces.

4. Particle diffusion and cataphoresis

Density and temperature gradients in gas discharges lead to the diffusion of both energetically excited and electrically charged particles to the walls and electrodes. Diffusion of ions to the walls can be a significant loss mechanism in fluorescent lamps but is negligible in HID lamps in comparison to the other energy channels. Charged-particle diffusion can play an important role in all discharge lamps by influencing the spatial distribution of atoms and molecules. Electrons are much more mobile than ions, and the ambipolar space charge field is established to maintain an equal radial flow of ions and electrons to the walls and preserve charge neutrality. Ions are thus accelerated away from the center of the discharge, while the electron motion is retarded.

Most lighting discharges include a "buffer gas," which retards ion loss, and an "active species," which is more easily excited to produce light and more readily ionized. The preferential ionization of Hg and Na in low-pressure Hg-Ar (fluorescent lamp) and Na-Ne (low-

pressure sodium) discharges, respectively, and of additive metal atoms in high-pressure MH lamps leads to a "demixing" of the active species from the buffer gas. This occurs when ions of the active species leave the discharge at a faster rate than they can be replaced by diffusion of neutral atoms or molecules through the buffer gas.

This *cataphoresis* phenomenon has been well studied in gas discharges (Chanin, 1978). In fluorescent lamps, cataphoresis leads to depletion of mercury at the center of the discharge, while depletion of sodium in low-pressure sodium lamps is a major limitation to efficacy (van Tongeren, 1975). In HID lamps, ions from the radiating species in the center of the arc diffuse to the mantle and are caught in the convection flow near the walls, which may result in species redistribution and color separation at different ends of the lamp.

5. Electrodes

Gas discharge lamps usually operate on an ac supply, which means that each electrode acts alternatively as an anode and as a cathode during each cycle.

Electrons are emitted from the cathode principally by thermionic emission. The electron current density at the cathode j_e is proportional to $T_k \exp(-\phi_{\text{eff}}/k_B T_k)$, where ϕ_{eff} is the effective work function of the cathode material (the potential barrier that electrons must overcome in order to leave the surface), k_B is Boltzmann's constant, and T_k is the cathode temperature. Efficiency of electron emission can thus be increased by increasing the cathode temperature or choosing a cathode material with a lower work function. Lower-work-function materials have the advantage that the cathodes can operate at lower temperatures, resulting in longer electrode life. In fluorescent, high-pressure mercury, and high-pressure sodium lamps, cathodes are coated with an electron-emitting activator material, while the tungsten electrodes in MH lamps are impregnated with thorium oxide to reduce the work function. This hot-cathode operation distinguishes these discharges from classical "glow discharges," which operate with cold cathodes.

During steady-state operation, the cathodes are maintained at the required temperatures for thermionic emission by the passage of current through them and by bombardment of ions from the discharge. The ion current in the main discharge (positive column) is too small to provide sufficient heating, so a positive space charge sheath develops at the cathode to accelerate the ions and enhance the ion flux in the near-cathode region. The cathode surface is thus maintained at a negative electric potential to the discharge, the *cathode fall*, which also accelerates electrons into the discharge.

The area of the cathode surface from which electrons are emitted is referred to as the *attachment area* of the discharge to the cathode. If emission takes place over the whole surface of the cathode (and even the upper parts of the rod or support structure), the lamp is traditionally said to operate in the *diffuse mode*, while if the current channel shrinks to an area that is small compared to that of the cathode, the lamp operates in a *spot mode*.

Electrons emerge from the cathode sheath in a current channel with an area much smaller than that in the main discharge (typically one-quarter to one-half of the cross section of the discharge tube in HID lamps and much less in fluorescent lamps). Further, the electric current in the sheath includes a large fraction of ions, whilst in the main discharge the current is overwhelmingly ($>99\%$) carried by electrons. The physical processes occurring in the transition region between the sheath edge and the main discharge are different in LTE and non-LTE discharges and are discussed in appropriate subsequent sections.

Since the anode does not emit ions, all the current crossing the anode surface must be carried by the electrons. If the required current to the anode I is more than the random electron current at the anode surface I_T, the anode must charge positively with respect to the main discharge in order to extract the necessary current. Conversely, if I_T is more than I, the anode charges negatively (Waymouth, 1971). The anode potential with respect to the plasma (the *anode fall*) depends on the physical properties of the anode. Power dissipated in the cathode and anode sheaths reduces the efficiency of the lamp and must be minimized.

B. Electrical circuit (ballast)

Breakdown of the insulating gas to create a plasma is generally achieved in discharge lamps by applying a high voltage across the electrodes, so that a single initial electron gains sufficient energy to ionize a gas atom. The electron created is then accelerated in the high electric field near the cathode and creates further ion-electron pairs, eventually generating an avalanche, which produces sufficient free electrons in the gas to carry the current required by the complete circuit, including the discharge (or, more exactly, to satisfy Kirchoff's laws for the circuit).

The required breakdown and starting (ignition) potential is always higher than the operating voltage of the lamp. If the circuit had no current-limiting feature, the electron avalanche would grow exponentially (runaway) and the resulting lamp (arc) current would destroy the lamp. The ballast must therefore provide a high open-circuit voltage for ignition, but limit the current to the value required to supply the lamp operating voltage during steady-state operation, with minimum consumption of electric power and no adverse effect on lamp life.

In principle, the current-limiting impedance provided by the ballast could be resistive; however, the power dissipated in the resistance R_B due to the electric current I is $I^2 R_B$, which adds to power consumption of the circuit, thus reducing system efficacy. The necessary impedance in the ballasts of discharge lamps operated on ac is predominantly reactive, with inductive and capacitive components, minimizing power dissipation.

A conventional magnetic ballast consists of a coil of wire wound on a ferromagnetic core and operates at the supply line frequency; it may be either an inductive type or a transformer type with considerable leakage inductance. Typical magnetic ballasts have a power-transfer efficiency of about 85%. Characteristics that limit ballast efficiency include wire/winding losses, core magnetizing current losses, core eddy current losses (gauss-related), and fringe-field/core-gap losses.

An electronic ballast is a ballast utilizing high-frequency switching that is controlled by active components (transistors, thyristors, etc.), with the lamp ballasting impedance provided by a series capacitive or inductive reactance appropriate for the high switching frequency.

Understanding the interaction between lamp electrical requirements and ballast efficiency requires a thorough understanding of the lamp starting mode, glow-to-arc transition, and steady-state operating mode.

C. Electrodeless lamps

While the first demonstration that light could be produced in the presence of a high-frequency electromagnetic field was by Tesla in 1891, almost a century elapsed before electrodeless lamps could be exploited commercially. The main obstacle to this development was the size, cost, and reliability of the driving electronics, but since the late 1980s progress in semiconductor electronics and power-switching technology have led to a number of new lamp products, primarily in fluorescent lighting.

There are four distinct types of excitation possible for electrodeless lamps (Wharmby, 1993, 1997; Lister, 1999; Godyak, 2002), all of which are described below. However, only two of these methods (inductive and microwave discharges) have been successfully applied to commercial light sources.

(1) *Inductive or H discharges:* The discharge current through the plasma of an *H* discharge acts as a single-turn secondary loop of a transformer, excited with a primary coil which may be placed in or around the discharge. Provided sufficient power is applied to maintain the *H* discharge, high coupling efficiencies may be achieved at low frequencies, with the benefits of reduced electromagnetic interference and less expensive electronics. A number of inductively coupled fluorescent lamps have been introduced into the market in the last decade (see Sec. VI.C.1).

(2) *Capacitive or E discharges:* The simplest *E* discharge is created in a gas-filled vessel placed between the plates of a capacitor. Capacitive radio-frequency (rf) discharges are, in principle, electroded discharges, although the rf electrodes can be placed outside the discharge vessel. Coupling of the applicator to the discharge is principally through the sheaths next to the electrodes, resulting in a strong dependence of discharge characteristics on frequency. In contrast to *H* discharges, higher power densities are achieved only at higher frequencies, where the cost of electronics and electromagnetic interference issues are more serious.

(3) *Microwave discharges:* The wavelength of the electromagnetic field in microwave discharges is comparable to the dimensions of the exciting structure and vessel. The only microwave discharges for lighting that have been introduced commercially are specialized high-power devices (Turner *et al.*, 1995).

(4) *Traveling-wave discharges:* The plasma in a traveling-wave discharge (such as a surface wave) is created by an electromagnetic wave traveling along a slow-wave structure formed by the plasma column itself. There was considerable interest in the potential of surface waves for application to fluorescent lighting in the late 1980s, but these were found to suffer from some of the problems of capacitive discharges (see Sec. VI.C.3).

IV. DISCHARGE LAMP DIAGNOSTICS

A. Emission spectroscopy

Emission spectroscopy is the most important diagnostic technique for lamp discharges, because the primary purpose of any lamp discharge is to produce light. A long list of important questions can be addressed using emission spectroscopy, including the following: What impurities, if any, are present in the lamp? What atoms or ions are radiating? Where in the discharge are they radiating? What is the total density of radiating atoms or ions? What is the excitation rate in a non-LTE discharge, or excitation temperature in a LTE discharge of the radiating atoms or ions? What is the gas-kinetic or translational temperature in a non-LTE discharge? What are the densities of perturbing atoms, ions, and electrons in a LTE discharge? What is the temporal structure of the radiation from a lamp operated with ac excitation? Are the important spectral lines optically thin or thick? What is the angular distribution of radiation from the lamp? What fraction of the electrical input power is released as radiation in each spectral range from the UV to the IR? If, or when, important molecular discharge lamps are developed, emission spectroscopy will be used to address a similar list of questions on radiating molecules.

Spatially resolved emission spectroscopy, like absorption spectroscopy, is a line-of-sight diagnostic. Measurements of "side-on" intensity for various chords through a cylindrically symmetric plasma can be converted into radially resolved data using an Abel inversion (see the recent review by Buie *et al.*, 1996). Figure 1 shows a spatially resolved emission spectroscopy experiment with a provision for comparing an experimental lamp to a radiometric standard lamp.

Emission spectroscopy with radiometrically calibrated instruments is essential for determining the overall power balance of a low- or high-pressure discharge plasma, a task more easily accomplished in the visible

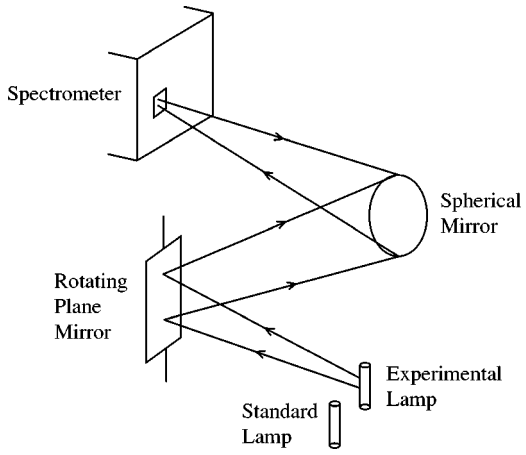

FIG. 1. Emission spectroscopy experiment with a provision for comparison to a radiometric standard lamp for intensity calibration. Emission intensity is recorded as a function of wavelength, time, location in the lamp, or other parameters using a grating spectrometer equipped with a detector array or a Fourier-transform spectrometer.

than in the UV or IR but never trivial (see, for example, Moore, 1980; Wharmby, 1980). An accurate measurement of the total light emission requires proper averaging over the spatial and angular distributions of light from the lamp. In principal this averaging can be accomplished with a projection radiometry set up as shown in Fig. 1, but in practice it is rather difficult, since angular distributions vary between optically thick and thin wavelengths. It is usually better to enclose the lamp in an integrating sphere for total output measurements. Integrating spheres and standard lamps with known power output per spectral interval are highly developed for the visible region, but are less developed in the UV and IR. Incandescent (tungsten filament) lamps are typically used as standards in the visible. Detectors, usually with appropriate filtering, are calibrated to measure lumens directly. For the purpose of this discussion we consider the direct measurement of total lumen output using an integrating sphere to be a low-spectral-resolution, absolutely calibrated, spatially averaged emission spectroscopy measurement. A luminous efficacy determination is a key measure of lamp performance, but it does not provide a complete picture of the power balance.

Spectra of low-pressure Hg-Ar (fluorescent lamp) discharges with modest spectral resolving power ($\lambda/\Delta\lambda = 5000$) and even a rough relative radiometric calibration yield much valuable information. The Hg resonance lines at 254 and 185 nm dominate the spectra by a large factor. Rare-gas emission lines are nearly absent except possibly near the electrodes or in cases of strong radial cataphoresis (Bakker and Kroesen, 2000). If such discharges are operated in ac mode at line frequency, then the radiation output oscillates at twice the line frequency. At modest power densities, the excited atom density as a function of radius mimics the radial distribution of electrons.

Great care is required for meaningful radiometrically calibrated emission measurements, as demonstrated in the classic spectroscopy study of Koedam *et al.* (1963) on low-pressure Hg-Ar discharges. In addition to quantifying the dominance of the Hg resonance lines at 254 and 185 nm, they demonstrated that proper treatment of the angular distribution of radiation from a small aperture in the side of a positive column is essential for radiometrically calibrated emission spectroscopy. The "Koedam beta factor," which characterizes the angular distribution of light from a small aperture in the side of positive column, is influenced by discharge and lamp wall parameters (Lawler *et al.*, 2002). Dorleijn and Jack (1985) performed a power balance study on an expanded set of fluorescent lamps including some small-diameter lamps and lamps operated with 25-kHz electronic ballasts.

The classic emission study on the low-pressure Na-Ne lamp (cf. Sec. VIII.A) by van Tongeren and Heuvelmans (1974) and van Tongeren (1975) also revealed much valuable information. Most importantly, the Na resonance multiplet at 589 nm (*D* lines) completely dominates the spectrum and neon emission is absent except possibly near the electrodes. Under some conditions spectral lines other than the dominant resonance multiplet are scarcely detectable. The temporal variation of the output radiation at twice the line frequency, and absence of axial cataphoresis, are observed during ac operation.

Emission spectra of higher spectral resolving power ($\lambda/\Delta\lambda = 50\,000$) on low-pressure Hg-Ar or Na-Ne discharges reveal that the dominant resonance lines in each case are severely self-reversed from radiation trapping, which reduces the effective decay rates of the resonance levels. Both Hg-Ar and Na-Ne lamp discharges in typical geometries run most efficiently with a few millitorr of metal vapor and a few tenths to a few torr of inert buffer gas. The few millitorr of metal vapor result in very large optical depths at the center of the strongest resonance lines. Enhancing the abundance of the rare Hg 196 isotope was shown to reduce radiation trapping (Maya *et al.*, 1984; Grossman *et al.*, 1986), but the resulting increase in lamp efficiency is insufficient to warrant commercialization.

Extremely-high-resolution ($\lambda/\Delta\lambda = 500\,000$) emission spectra of Hg-Ar or Na-Ne discharges reveal more details of the line profiles in addition to the severe self-reversal of the dominant resonance lines. The hyperfine structure of Na and Hg lines as well as the isotopic structure of Hg lines are largely resolved. The Voigt profiles of optically thin line components are visible in extremely-high-resolution spectra, and the Doppler-broadened Gaussian core of these Voigt profiles can be used to measure the translational temperature of gas in the discharge. This can be done using classical emission spectroscopy with a very-high-resolution Fabry-Perot etalon, but a laser-induced fluorescence technique with a single-frequency laser is typically used now for such measurements.

Emission spectroscopy has also been used in efforts to find an environmentally friendly substitute for Hg in fluorescent lamps. Among the candidates studied have been low-pressure Xe discharges (Doughty and Fobare,

1995; Sommerer and Doughty, 1998), low-pressure S_2 discharges (Gibson and Lawler, 1996), and low-pressure Ba discharges (Laski *et al.*, 2002; Peng *et al.*, 2002).

Emission spectroscopy is also used to address questions in high-pressure LTE discharges. While the spectrum of a pure Hg arc plasma at several atmospheres resembles that of a low-pressure Hg-Ar discharge, close inspection reveals important differences (Elenbaas, 1951). The relative intensities of the near-UV and visible lines connecting lower excited levels of Hg are greater in high-pressure LTE discharges than in low-pressure discharges. The spectral radiance of a Hg ultraviolet resonance line from a LTE arc discharge is limited by the second law of thermodynamics to the blackbody radiance at the arc core temperature, which is typically in the range of 6000 K. The Hg ultraviolet resonance lines and many of the prominent visible lines are self-reversed in emission spectra of LTE discharges due to the temperature gradient from the arc core ($\sim$6000 K) to the arc tube wall ($\sim$1200 K). Spectral line profiles are far broader than for low-pressure lamps and are dominated by broadening from neutral-atom and charged-particle collisions. High-pressure lamps operating in an ac mode at line frequency show a modulation of twice the line frequency, as in low-pressure lamps. The modulation tends to be less deep than in low-pressure discharges because the arc temperature responds more slowly to changing current due to the thermal inertia of the high-pressure discharge (Stormberg and Schäfer, 1983).

The spectrum of a MH lamp reveals much additional information. A metal iodide additive containing a transition metal such as Sc or a rare-earth metal such as Dy will result in a spectrum with thousands of additional emission lines. Typically, the strongest additive metal atom and ion lines are self-reversed like most Hg lines, but many additive lines are optically thin. The additives also tend to reduce the arc temperature.

Emission spectroscopy was used to study the power balance of pure Hg and MH lamps containing iodides of Na, Tl, In, Dy, and Sn (Jack and Koedam, 1974) and of a MH lamp with NaI and ScI_3 additives (Keeffe, 1975). There are also several thorough emission studies of MH lamps with NaI and ScI_3 additives. These include the study of Dakin and Gilliard (1987), who used rapid rotation to suppress convection, Dakin *et al.* (1989), who included axial segregation effects caused by a combination of convection and radial cataphoresis, and Rogoff *et al.* (1987). Dakin *et al.* included detailed comparisons of their experimental results to a model of their MH lamp.

Emission studies of spectral line profiles are more frequently performed on high-pressure lamps than on low-pressure lamps, in part because high-pressure profiles are much broader and thus easier to measure. Emission spectra, together with models for self-reversed lines developed by Bartels (1949a, 1949b) and others, are widely used to determine the axial temperature and radial variation of temperature near the axis of high-pressure LTE discharges. Zwicker (1968) provides a lucid explanation of Bartel's method, and Karabourniotis (1986) reviews various models used for interpreting self-reversed spectral line profiles.

Resonance collisional broadening is often observed in lamp emission spectra, as exemplified by two Hg visible lines: 492 and 577 nm. Both are connected to the $6\,^1P_1$ resonance level, which would be the true resonance level of Hg if not for the relativistic breakdown of Russell-Saunders coupling, which mixes the $6\,^3P_1$ and $6\,^1P_1$ levels. Even with this mixing, the radiative transition probability of the 185-nm line from the $6\,^1P_1$ level to the ground level is about 100 times larger than that of the 254-nm line from the $6\,^3P_1$ level to the ground level. All transitions connected to the $6\,^1P_1$ level have very large broadening coefficients due to resonance collisions—collisions in which an Hg atom excited to the $6\,^1P_1$ level interacts with a ground-state Hg atom and the two quantum mechanically share the available excitation energy. This resonance interaction leads to a long-range, $1/r^3$, dipole-dipole potential curve and to the resonance collisional broadening seen in the emission spectra. Such broadening is well understood (Corney, 1977) and can be used to measure absolute Hg atom densities in high-pressure arc discharges (Asselman *et al.*, 1992).

New possibilities for emission spectroscopy diagnostics are afforded by very powerful Fourier-transform spectrometers (Adler *et al.*, 2001), such as the 1-m spectrometer at the U.S. National Solar Observatory on Kitt Peak, AZ. This instrument provides very broad UV-to-IR wavelength coverage, extraordinary (1 part in 10^8) wave-number accuracy, a very small ($0.01\ \mathrm{cm}^{-1}$) spectral limit of resolution, and a massive data collection rate. All such instruments also have an intrinsic advantage for spectroradiometric measurements over large wavelength ranges due to the fact that an interferogram is a simultaneous measurement of an entire spectrum. Because all intrinsic spectral features can be fully resolved, spectra from Fourier-transform spectrometers have the potential to provide fundamental data for modeling radiation transport in MH lamps and important insight on the relative role of atomic/ionic versus molecular radiation from MH lamps.

B. Laser-induced fluorescence, Raman scattering, and Rayleigh scattering

The development of good tunable lasers in the 1970s opened the way for laser-induced fluorescence (LIF) experiments in lighting plasmas. Tunable or fixed-frequency lasers are used for laser Raman-scattering and Rayleigh-scattering experiments in these discharges. In the following discussion we shall use rather simple distinctions between LIF, Raman-scattering, and Rayleigh-scattering experiments. Experiments using LIF are distinguished from the other two by the excitation of real levels instead of virtual levels. Experiments using Rayleigh scattering are distinguished from those using Raman scattering by whether the final atomic (electronic) level after the scattering process is the same or different from the starting level. Under some conditions, with

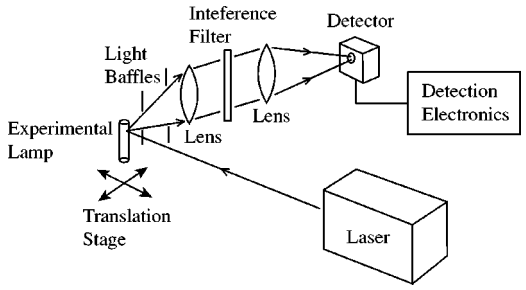

FIG. 2. Laser-induced fluorescence (LIF) experiment. Note the use of an interference filter for spectral filtering, and either a gated detection system in a pulsed-laser experiment or phase-sensitive detection system in a modulated continuous-wave laser experiment. Light baffles are also important in limiting the amount of background light from the discharge that reaches the detector. Fluorescence signals are recorded as a function of wavelength, time, location in the lamp, or other parameters, using a tunable dye, diode, or Ti:sapphire laser.

carefully chosen differences between the laser frequency and atomic resonance frequency and with optimal dephasing collision rates, it is possible to simultaneously observe all these. Such experiments tend to be more focused on the physics of the scattering process (Burnett, 1985) than on the physics of the discharge. In high-pressure discharges, LIF experiments are effectively local heating experiments, because the laser-excited atoms are collisionally thermalized in far less than a radiative lifetime. Due to small scattering cross sections, Rayleigh and Raman scattering are used more in high-pressure discharges than in low-pressure discharges.

Laser scattering and LIF experiments complement emission spectroscopy by providing access to the lower levels of transitions, especially metastable and ground levels of both atoms and ions, which do not radiate. The metastable levels are very important in both the power balance and the ionization balance of low-pressure lighting discharges. LIF also provides better spatial and temporal resolution than emission spectroscopy. It is easier to achieve very high spectral resolving powers, which are needed to directly observe a Stark or Doppler width, with LIF than with classical emission techniques. LIF can also be used in pump-probe experiments to measure time-resolved data and determine rates.

Figure 2 shows a LIF experiment. The interference filter in Fig. 2 would probably need to be replaced by a more sophisticated spectroscopic filtering system for a laser scattering experiment.

The excellent spatial resolution possible in LIF experiments on low-pressure discharges is illustrated by the work of Bhattacharya (1989a, 1989b) and van de Weijer and Cremers (1985a, 1985b, 1985c). In low-pressure discharges, the spatial distribution of ground-level atoms of the dominant buffer gas is usually almost uniform, but the spatial distribution of excited atoms and additive species may be nonuniform. Loss of the emission mix, Ba-Sr-Ca oxide, from the electrodes of fluorescent lamps is a common failure mechanism, and gas-phase Ba atoms or ions from the hot spot on the cathode are concentrated near the electrode. Alkaline earths such as Ba are ideal for LIF experiments, since neutral Ba and Ba^+ have very convenient wavelengths for laser excitation (553.5 and 455.4 nm, respectively). Bhattacharya (1989a, 1989b) used LIF to map the density of Ba atoms and ions in the electrode region of a low-pressure Hg-Ar discharge. Fluorescence from the resonance level of Ba^+ is detectable at 614.2 nm, which is even more convenient, since this fluorescence is easily isolated from laser light scattered from the lamp wall or windows. Bhattacharya proposed using an absorption measurement to provide an absolute calibration of the LIF measurements. Detailed spatial (near the electrode) and temporal (during the ac period) maps of the Ba and Ba^+ densities from his experiment were compared with a model to gain a more quantitative understanding of the loss of emission mix from the electrode of a fluorescent lamp.

LIF measurements have provided important tests of radiation-trapping calculations for low-pressure Hg-Ar lighting dischanges. For example, van de Weijer and Cremers (1985a, 1985b, 1985c) measured the trapped decay rate of the Hg $6\,^3P_1$ resonance level in Hg-Ar positive-column discharges for a wide variety of conditions. They used a laser at 404.7 nm to excite Hg atoms from the $6\,^3P_0$ metastable level to the $7\,^3S_1$ level. The laser-excited atoms in the $7\,^3S_1$ level do not all decay back to the $6\,^3P_0$; some decay to $6\,^3P_1$ and $6\,^3P_2$ levels. The relaxation time of the excess population in the $6\,^3P_1$, which is the trapped decay rate of the resonance $6\,^3P_1$ level, was measured by observing the 254-nm fluorescence.

The use of semiconductor laser systems in LIF experiments eliminates some of the cost and complexity of organic dye lasers. A good example is work by Yuasa *et al.* (1997). Many strong Ar lines from the lowest excited $3p^5 4s$ configuration, which includes the metastable and resonance levels, to the next-highest $3p^5 4p$ configuration are accessible with GaAs/AlGaAs and similar diode lasers (wavelength$>$630 nm). Diode laser technology will probably soon be applied to important Hg lines in diagnostic experiments on lighting discharges since GaN diode lasers ($388<\lambda<450$ nm) can now reach Hg lines in the blue and near UV.

LIF has also been used to measure Stark broadening and shifts in a low-pressure Na-Ne discharge (Cornelissen and Burgmans, 1982). This experiment involved Doppler-free two-photon excitation of the $3s$-$4d$ sodium transition with laser radiation at 578.3 nm, followed by detection of $4p$-$3s$ cascade fluorescence at 330 nm. Doppler-free excitation from counterpropagating laser beams yielded very small linewidths and an ability to measure Stark shifts as small as 10 MHz. Stark shifts and broadenings due to Holtzmark fields in the plasma were measured and used to determine the local plasma density. Cornelissen and Burgmans measured electron densities as small as 10^{18} m^{-3} with submillimeter spatial resolution.

Even the ground-level Hg^+ ions in a Hg-Ar fluorescent lamp discharge have been studied by LIF, using

194-nm vuv radiation produced via nonlinear optical techniques (Wamsley *et al.*, 1991)

Like LIF, electronic Raman scattering has been used in the study of low-pressure lighting discharges (Bigio and Johnson, 1991), but it has been used more to study high-pressure discharges. Numerous laser scattering and LIF experiments have been done on high-pressure LTE lighting discharges and a few examples are cited below.

To measure the radial variation of gas density and temperature in an Ar arc discharge, Vriens (1973) employed a powerful ruby laser with pulse energies sufficient to distinguish the Rayleigh scattering from the arc emission itself. Using LIF in high-pressure arc discharges both of pure Hg and of Hg with metal-halide and Na additives, van den Hoek and Visser (1981) examined the rapid thermalization of the absorbed laser energy. They also used LIF to measure spectral line shapes and shifts and atom density ratios and determined electron densities from Stark broadening. Adriaansz and Vriens (1976) demonstrated the utility of electronic Raman scattering in a study of Al and In atoms in MH arc plasmas. Vriens and Adriaansz (1974) discussed using these diagnostics to explore deviations from local thermal equilibrium in arc discharges.

Kramer (1990a, 1990b, 1991a) used saturated LIF to map densities of ground-state Sc, Sc^+, and excited Hg $6\,^3P_1$ atoms in a metal halide arc discharge. Saturation of a LIF transition with an intense laser pulse reduces the effect of spatial variations on the fluorescence quantum efficiency. Kramer derived and used corrections for radiation trapping of the fluorescence and explored the time variation of parameters during the ac cycle of MH lamps.

The examples cited above illustrate the utility of LIF, laser Raman scattering, and laser Rayleigh scattering diagnosing both low- and high-pressure lighting discharges. In general, LIF and laser scattering diagnostics provide superb spatial and temporal resolution, but are somewhat less suited than absorption spectroscopy for determining absolute densities.

C. Absorption spectroscopy and the Hook method

Absorption spectroscopy and the related Hook (anomalous dispersion) method for large column densities provide absolute column densities without any radiometric calibration, provided accurate absolute transition probabilities are available. This is a significant advantage, since reliable absolute measurements provide a more demanding test of a model than relative measurements. Absorption spectroscopy has become easier and less expensive due to improved technologies including diode lasers and detector arrays.

Classic absorption experiments on low-pressure lighting plasmas, such as the experiment by Koedam and Kruithof (1962), used line emission from one discharge to observe absorption in another discharge. This is a sound technique, but it requires very detailed knowledge of the spectral line profile from the source discharge and in the sample or absorbing discharge. Isotopic and hyperfine structure, Doppler and collisional broadening, as well as any effects from radiation trapping must be understood and modeled with both precision and accuracy when using this method.

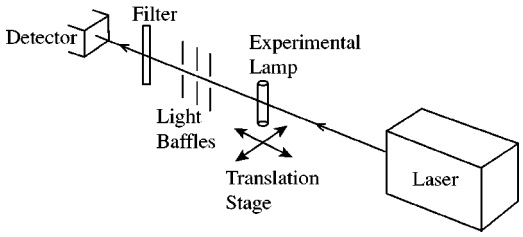

FIG. 3. Laser absorption experiment. Typically the spectral radiance of a laser is so many orders of magnitude greater than a lamp that the signal from the transmitted laser light will overwhelm the light from the experimental lamp with relatively simple spatial and spectral filtering. Transmittance is recorded as a function of wavelength, time, location in the lamp, or other parameters.

Figure 3 shows an absorption experiment using a tunable laser. Cornelissen and Merks-Eppingbroek (1986) used a continuous-wave dye laser to perform absorption spectroscopy on the ground-level Na atoms in a Na-Ne discharge. They set the laser frequency using a temperature-stabilized cell containing Na and Ne, and their measurements were made in the pressure-broadened Lorentzian wings of the line profile. This approach works well, but it is important to include effects from spatial and temporal variation in the spectral line profiles in the data analysis. Cornelissen and Merks-Eppingbroek mapped the radial variation of the ground-level Na density and used this information to deduce the electron density and temperature.

Experiments by Bigio (1988) and Bigio and Dakin (1989) illustrated the utility of two different methods for determining absolute column density in low-pressure Hg-Ar fluorescent lamp discharges. Their studies of radial variations of excited Hg atom densities involved measurements of very large column densities, since they were measuring along axial sight lines. A traditional curve-of-growth analysis, which involves computing a relation between the equivalent width and column density, is insensitive for some ranges of column densities in low-pressure discharges, due to the dominance of Doppler broadening (Thorne *et al.*, 1999). One approach to overcoming this problem is the saturated laser absorption method, in which the total energy absorbed from a high-energy laser pulse is determined. Another approach used by Bigio (1988) is the Hook method, which involves setting up an interferometer around the discharge to observe the anomalous dispersion near a strong transition. Both methods are useful for accurately measuring large column densities. The use of a laser source in the Hook method provides better spatial and temporal resolution than can be achieved using incoherent sources.

The experiments cited above illustrate the utility of dye lasers in performing absorption and Hook experiments on low-pressure lighting discharges. The development of modern detector arrays also opened up interest-

ing possibilities for absorption spectroscopy experiments on lighting plasmas.

Wamsley *et al.* (1990) developed a very simple and low-cost absorption experiment using a Xe arc lamp as a continuum source, a mechanical chopper, and a lock-in amplifier. Their phase-sensitive detection system was used to discriminate against light from a low-pressure discharge, which served as an absorbing sample, while detecting only light from the continuum source with absorption features from the low-pressure discharge. They applied this experiment to Hg-Ar fluorescent lamp discharges and were able to measure column densities of excited Hg atoms and ground-level Hg^+ ions using the traditional curve-of-growth analysis method. Wamsley *et al.* also studied the axial variations of excited Hg atom and ground-level Hg^+ ion densities near the electrode.

Wamsley *et al.* (1993a) further developed this simple approach to absorption spectroscopy on low-pressure discharges by replacing the phase-sensitive detection system with a charge-coupled device (CCD) detector array. In this improved experiment, precise gating of the detector array, together with a digital subtraction technique, were used to discriminate against light from the low-pressure discharge, which served as an absorbing sample, while detecting only light from the Xe arc lamp. Although their experiment did not have the temporal resolution of pulsed laser absorption experiments, it achieved remarkable sensitivity. The use of a modern detector array made the experiment insensitive to nonquantum fluctuations, which often limit the sensitivity of sequentially scanned single-channel absorption experiments.

Sequentially scanned experiments using an arc lamp as a continuum source and a grating spectrometer are often limited in sensitivity by flicker in the arc lamp. This flicker is mapped directly onto the absorption spectrum and makes it difficult to detect small fractional absorptions. Pulsed lasers, needed for deep UV or vuv experiments, suffer from "shot-to-shot" fluctuations, which are often an equally serious problem limiting the sensitivity of absorption experiments. By recording an entire absorption spectrum at once, a detector array is largely immune to nonquantum noise. Furthermore, the detector array also suppresses quantum or Poisson statistical noise by simultaneously collecting good photon statistics in all spectral resolution elements. Signal-to-noise ratios of 3×10^5 can be achieved using this method (Anderson *et al.*, 2000).

Wamsley *et al.* (1993a) first used an image-intensified CCD array for precise gating of exposures, but it is now realized that a photodiode array is adequate for most high-sensitivity absorption spectroscopy experiments, as shown in Fig. 4. Wamsley *et al.* (1993b) used their improved absorption experiment to study the role of excited Ar atoms in the ionization balance of the negative glow region of a low-pressure Hg-Ar discharge. Curry *et al.* (2002) used the same method with a photodiode array to measure excited Hg atom densities in a Hg-Ar

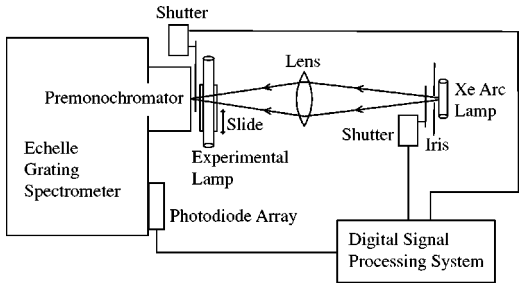

FIG. 4. High-sensitivity absorption spectroscopy experiment using an arc lamp continuum and echelle spectrometer equipped with a detector array. In this experiment digital processing is used to eliminate the light from the low-pressure experimental lamp and detect the continuum from the arc lamp with absorption features from the low-pressure lamp. A spectrum of the low-pressure lamp is subtracted from a spectrum of the arc lamp plus the low-pressure lamp, and the resulting difference spectrum is divided by a dark signal-corrected spectrum of the arc lamp continuum. Transmittance is recorded as a function of wavelength, time, location in the lamp, or other parameters.

fluorescent lamp discharge under high-power-density conditions, and compared their experimental results with model predictions.

The preceding examples illustrate the utility of absorption spectroscopy as a diagnostic for low-pressure lighting discharges. Absorption spectroscopy has been equally useful in studies of high-pressure lighting discharges. Schäfer and Stormberg (1986) used a frequency-doubled Ar^+ ion laser to measure ground-level Hg densities in high-pressure Hg lamps. They used the second harmonic of the 514.5-nm Ar^+ ion laser line to study absorption in the wings of the 254-nm Hg resonance line. Allen *et al.* (1987) used a tunable dye laser to measure the ground-level Na atom density in a MH lamp. Although they used the 589-nm resonance multiplet of Na, which is optically thick at line center, they were able to get reliable column densities from the Lorentzian line wings of the absorption feature to study demixing of the Na in a MH lamp.

Recently Bonvallet and Lawler (2003) performed optical/UV absorption spectroscopy on a MH lamp using synchrotron radiation as a continuum, using the High Sensitivity Absorption Spectroscopy facility at the Synchrotron Radiation Center in Stoughton, WI. This facility includes a large 3-m focal-length vacuum echelle spectrometer equipped with a UV-sensitive CCD array. Bonvallet and Lawler mapped the density of ground-level Sc atoms, excited Sc atoms, ground-level Sc^+ ions, and ground-level Na atoms as part of a project to study IR losses from MH lamps (Smith *et al.*, 2003). An analysis of local thermal equilibrium was used to extract a radial temperature map and electron density map from atom and ion density maps. The use of synchrotron radiation as a continuum source in the optical, UV, and vuv has advantages and disadvantages in comparison to using laser radiation. Laser experiments are more convenient because they can be performed "in-house," but synchrotron radiation experiments provide great flex-

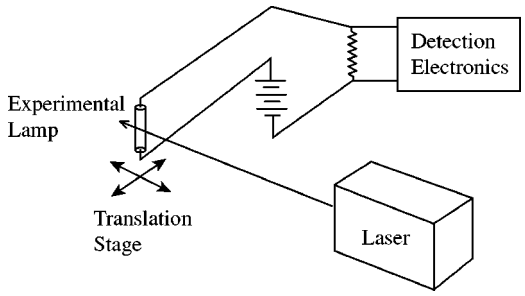

FIG. 5. Optogalvanic effect experiment. The perturbation to the discharge current or voltage is recorded as a function of wavelength, time, location in the lamp, or other parameters.

ibility with respect to wavelength and superb signal-to-noise ratios in the UV and vuv.

D. Laser optogalvanic effects

Optogalvanic effects are perturbations to the electrical characteristics of a discharge due to absorption of radiation at a wavelength corresponding to an atomic or molecular transition. Figure 5 shows a simple optogalvanic-effect experiment. Such experiments are particularly useful for observing transitions that do not fluoresce. Lawler and Doughty (1994) reviewed techniques for mapping electric fields in glow discharges using optogalvanic detection of Rydberg atoms and other methods. Collisional quenching of the Rydberg atoms in a typical discharge suppresses fluorescence, and Rydberg atoms experience large and easily measured Stark effects. Techniques for mapping space-charge fields have been quite useful in studies of a variety of discharges, but the techniques have not yet been extensively used to study lighting discharges. The cathode region of cold cathode discharges at pressures of 10 torr or below has a spatial extent of 1 mm or more with a large and rapidly varying electric field. Optogalvanic detection is ideal for studying the nonhydrodynamic behavior of electrons in this region (Doughty and Lawler 1984; Den Hartog *et al.*, 1988). Cold cathode discharges are never used for general illumination because they are lossy, but they are used for back-lit displays. Typically more than half of the electrical power dissipated in the cathode region of cold cathode discharges is consumed by moving ions to the cathode surface.

Although optogalvanic detection of Rydberg atoms has not been used extensively to study lighting plasmas, there is another way to use optogalvanic effects for this purpose. They can be used to test a model of an unperturbed discharge by applying linear perturbation theory to the model and comparing model predictions to experimental results. For a low-pressure discharge it is usually advantageous to focus on the ionization balance when modeling an optogalvanic effect. However, in high-pressure discharges absorbed laser energy is quickly thermalized, and thus it is best to focus on the power balance. It is simplest to think of an optogalvanic effect as a shift in the current voltage characteristics of the discharge and then to use a load line analysis to determine whether the shift results primarily in a voltage perturbation or in a voltage and current perturbation. A large ballast resistor forces the optogalvanic effects to become perturbations to the discharge voltage and thus E/N (reduced field). A smaller ballast resistor results in optogalvanic effects that are significant perturbations to the discharge current. In a low-pressure discharge, the ballast resistor helps determine how electron energy and density perturbations are coupled, which affects the temporal response of the optogalvanic effect. An interesting experiment by van de Weijer and Cremers (1985a, 1985b) explored changes in the temporal characteristics of an optogalvanic effect due to varying the ballast resistor of a low-pressure Hg discharge.

Doughty and Lawler (1983) measured the absolute magnitude of optogalvanic effects in a low-pressure Ne positive column for comparison to a model. Similar Ne discharges are used in specialty products for automotive tail lights. It is not difficult, starting from a model of an unperturbed discharge, to apply first-order perturbation theory and generate a model of an optogalvanic effect. Optogalvanic effects are almost always linearly proportional to the absorbed laser power. Saturation of such an optogalvanic effect is usually due to saturation or "bleaching" of the atomic transition, while the discharge perturbation continues to be linear with absorbed laser power (Lawler, 1980). A direct comparison of absolute measurements of optogalvanic effects to predictions from a discharge model is a stringent test of the model.

Stewart, Borthwick, *et al.* (2000) and Stewart, Smith, *et al.* (2000) demonstrated a powerful new diagnostic approach for low-pressure discharges based on combining optogalvanic effect data with LIF and laser-induced collisional fluorescence data in low-pressure Ne positive-column discharges.

Kramer (1988, 1991b) explored the utility of laser optogalvanic diagnostics in high-pressure Hg and MH discharges. In such discharges, optogalvanic effects generally correspond to an increase in discharge current. This is in contrast to in low-pressure discharges, in which these effects can be either positive (increased current) or negative (decreased current). Kramer studied radial variations of optogalvanic signals and compared these to LIF signals. Optogalvanic effects, in combination with other diagnostics, have significant potential for studies of high-pressure lighting discharges.

E. X-ray methods for high-pressure lamps

The relatively high densities of heavy or "high-Z" atoms in high-pressure lighting discharges make x-ray diagnostic methods quite useful in these systems. Unlike optical and UV techniques, x-ray techniques have spatial resolutions that are not limited by refraction and scattering from the arc tube and can obtain spatial information through translucent materials, such as the increasingly common Al_2O_3 polycrystalline alumina arc tubes. New diagnostic experiments have been facilitated by important advances in x-ray detection systems and

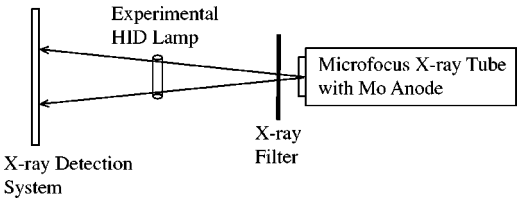

FIG. 6. X-ray transmission experiment on a HID lamp using a modern, highly linear detection system, either a phosphor image plate or two-dimensional diode array. The use of an x-ray tube with a Mo anode at a tube voltage of about 25 kV and a thin Mo filter yields a good flux of Mo K-line x rays near 18 keV. Enough of the 18-keV x rays will penetrate the arc tube and interact with the Hg vapor to yield good-quality data. The transmission signal is recorded for the entire lamp to yield the density of Hg as a function of position in the lamp.

sources, including phosphor image-plate detection systems, CCD detectors, and large-format two-dimensional diode arrays such as those developed for medical imaging. Synchrotron radiation sources for hard x rays, including the Advanced Photon Source at Argonne National Laboratory also have created new opportunities for x-ray diagnostic experiments on high-pressure lighting discharges.

X rays from a synchrotron radiation source were first used by Fohl *et al.* (1993) to diagnose both Hg and MH arc lamps. Their experiment used a gas-filled proportional counter for detecting the transmitted x rays to study the warmup and cooldown of an arc lamp. They calibrated their experiment using a water solution of Hg^{+} in dilute HNO_3.

Modern phosphor image-plate detection systems permitted Curry *et al.* (1998) to make a two-dimensional map of the Hg density in an entire arc lamp. They used a conventional x-ray tube with a Mo anode as a source. The K lines of Mo in the 17–20-keV range have a good overlap with the L-shell absorption peak of Hg and are sufficiently penetrating so that the arc tube absorption is tolerable. Their 2D map of the Hg density showed that these imaging techniques could be used to determine the arc temperature from the core to the wall and to provide some information on convective cells in arc lamps. Figure 6 shows an x-ray absorption/transmission experiment using a microfocus x-ray tube to produce magnified images of arc lamps.

X-ray fluorescence can also be used to map additive densities in operating MH lamps (Curry *et al.*, 2001). Fluorescence experiments had been attempted in the past, but success was first achieved with the extraordinary x-ray flux available at the Advanced Photon Source ring. The cryogenically cooled, double-crystal monochromator of the Synchrotron Radiation Instrumentation Collaborative Access Team (SRI-CAT) beam line at the Advanced Photon Source delivers photon energies of 40–300 keV with a flux density of about 10^{12} photons/(s mm^2) in a fractional bandpass of 10^{-3}. Figure 7 is a schematic of the x-ray fluorescence experiment reported by Curry *et al.* (2001). There are now interesting possibilities for combining optical/UV measurements of atomic and/or ionic densities with x-ray measurements of elemental densities and inferring densities of additive atoms tied up in molecules and radicals. This could be accomplished by subtraction of atomic/ionic density measurements from elemental density measurements (Bonvallet and Lawler, 2003).

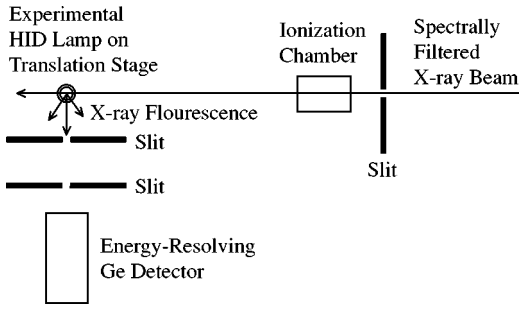

FIG. 7. X-ray fluorescence experiment on a metal halide lamp. The x-ray beam needs to be extremely intense and highly monochromatic. Such x-ray beams are available at the Advanced Photon Source synchrotron radiation facility at Argonne National Laboratory near Chicago, IL. The ionization chamber in this experiment is to monitor the x-ray-beam flux. The cyrogenically cooled Ge detector energy resolves the detected fluorescence x rays. Slit assemblies should be constructed using a dense material such as lead or tungsten.

F. Microwave interferometry

Electron column density measurements using microwave interferometry are reliable and relatively straightforward (Chen, 1974) and are routinely used in fusion plasma research (Gentle, 1995). Figure 8 is a schematic of a microwave interferometry experiment. Microwave interferometry is well suited to large-volume, low-pressure lighting discharges, with typical electron densities in the 10^{17}–10^{19}-m^{-3} range. The choice of microwave frequency involves a compromise between sensitivity and spatial resolution. An electron density of 10^{18} m^{-3} corresponds to an electron plasma frequency of $\nu_{pe}=9$ GHz, which suggests an interferometer design frequency in the range of $\nu=30$–70 GHz. The momentum-transfer collision frequency in a typical low-pressure lighting plasma is in the range of a few GHz and thus can be neglected. The corresponding wavelength for $\nu=70$ GHz is 4.3 mm, which sets the spatial

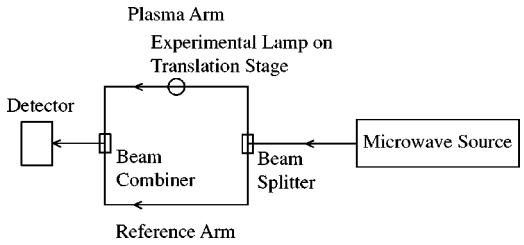

FIG. 8. Schematic of a microwave interferometer for electron column-density measurements. The phase shift between the plasma arm and reference arm due to the lamp is measured as a function of position, time, or other parameters.

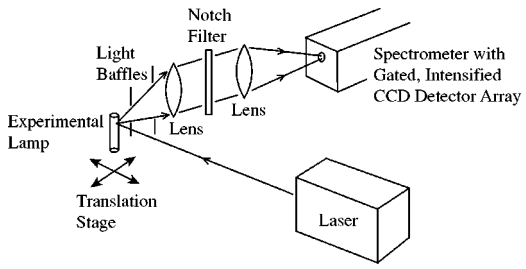

FIG. 9. Thomson scattering experiment. Extraordinary care is required to reduce backgrounds from several sources, including light scattered from various surfaces. The Thomson-scattered light is measured as a function of wavelength (Doppler shift) to yield the electron distribution function.

resolution scale of the interferometer. Clearly one can trade off spatial resolution for sensitivity, since the index of refraction is $n^2=1-\nu_{pe}^2/\nu^2$. Frequencies close to ν_{pe} yield larger phase shifts, which can be measured more accurately. Higher frequencies provide better spatial resolution.

Hebner *et al.* (1988) described electron density measurements with an 8.4-GHz microwave interferometer in an electrodeless discharge plasma that was in some respects similar to lighting discharges. They also described microwave radiometric measurements of average electron energies in their plasmas.

The possibility of using an IR interferometer for diagnosing high-pressure arc plasmas is worth considering. Electron densities in arc lamps range up to about 10^{22} m^{-3}, which corresponds to a plasma frequency of 900 GHz. The momentum-transfer collision frequency in a typical HID discharge is in the range of a few hundred GHz. Unfortunately arc-tube opacity may be a serious problem for IR interferometry.

G. Thomson scattering

Thomson scattering has been used for many years to measure electron temperatures or distribution functions in fusion plasmas (see, for example, Gentle, 1995), and recently it has been used to study processing plasmas (Muroka *et al.*, 1998; Moshkalyov *et al.*, 2000). Figure 9 shows a Thomson-scattering experiment. Many developments in Thomson scattering for fusion and nonfusion plasmas are described in a conference series on laser-aided plasma diagnostics (Muroka, 2001). Improvements in Q-switched laser performance, in intensified CCD detector arrays, and especially in optical filtering systems have expanded the utility of Thomson scattering to rather low electron densities that are well within the range found in low-pressure lighting discharges.

Bowden *et al.* (1999) described a Thomson-scattering experimental system with a lower detection limit of 5×10^{16} m^{-3}. Their multipass system was based on a high-repetition-rate Nd:YAG laser, a double monochromator for filtering, and an intensified CCD camera as a detector. The blocking of Rayleigh-scattered light and light scattered from windows and other surfaces is a crucial issue in almost all Thomson-scattering experiments, simply because the feeble Thomson scattering from free electrons is easily overwhelmed. Moshkalyov *et al.* (2000) described a Thomson-scattering experimental system with a lower detection limit of 5×10^{15} m^{-3}. Their system was also based on a high-repetition-rate Nd:YAG laser and an intensified CCD camera. Direct observation of non-Maxwellian distribution functions in low-pressure plasmas is now possible using Thomson scattering (Muroka *et al.*, 1998).

Thomson scattering has been used (van de Sande and van der Mullen, 2002) to map the electron density and electron temperature in a modified Philips QL® electrodeless lamp, an inductively coupled Hg-Ar discharge at high power density (see Sec. VI.C.1), with a detection limit of 1×10^{16} m^{-3}.

Vriens and Adriaansz (1974) discussed the potential of Thomson scattering as a diagnostic for high-pressure lighting discharges, but did not succeed in observing the scattering. It may be an opportune time to retry Thomson scattering in HID discharges in view of the major improvements in lasers, optics, and detectors since 1974.

H. Langmuir probes

Langmuir probes have been widely used to study plasma parameters in low-pressure discharges in fluorescent lamps since the early 1950s (see the review by Waymouth, 1989, and references therein). Relatively simple Langmuir-probe diagnostic techniques permit a number of basic plasma parameters (plasma density, electron temperature, and plasma potential) to be inferred from the measured current/voltage dependence (probe characteristic) of a small wire or disk metal probe, immersed into plasma. Although insertion of the probe in the plasma and collection of charged particles by the probe disturb the plasma, these disturbances (in some limiting conditions) are localized in the thin space-charged layer (sheath) around the probe, and undisturbed plasma parameters can be inferred from the probe characteristics. A typical probe characteristic on a linear scale is shown in Fig. 10.

The classic probe diagnostic developed by Langmuir has been modified to measure the probe characteristic $I_p(V_p)$ over a wide range of the probe voltage and extract the electron current $I_e(V_p)$. The section of the probe characteristic corresponding to electron repulsion ($V_p\leqslant V_0$, where V_0 is the plasma potential) plotted versus the probe voltage on a semilog scale for a Maxwellian plasma, is a straight line, whose slope is inversely proportional to the electron temperature,

$$T_e=\frac{e}{k_B}\left(\frac{d}{dV_p}\ln I_e\right)^{-1}, \tag{4.1}$$

where k_B is the Boltzmann constant and e is the unit charge. The electron density n_e can be calculated from the electron saturation current (the electron current to the probe when $V_p=V_0$)

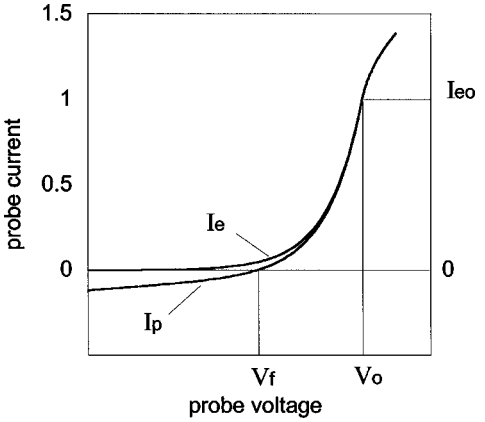

FIG. 10. Typical Langmuir-probe characteristic—linear scale.

$$I_{e0}=en_e s_p\left(\frac{k_B T_e}{2\pi m_e}\right)^{1/2}, \tag{4.2}$$

where m_e is the electron mass, and s_p is the area of the probe collecting surface.

Some plasma parameters can be found from sections of the probe characteristics where charged particles are attracted to the probe (Godyak *et al.*, 1993); $V_p>V_0$ corresponds to the electron saturation part of the probe characteristic, where electrons are attracted, while $V_p<V_f$, where V_f is the floating potential (for which the net probe current is zero) corresponds to the ion saturation part, where ions are attracted. In both cases, there is no real saturation for the small probes commonly in use.

The most significant development of probe diagnostics since Langmuir's time has been the technique for measuring the electron energy distribution function (EEDF). In-low pressure gas discharge plasmas, the EEDF is almost never Maxwellian and calculation of the rates of inelastic processes such as excitation and ionization using the electron temperature obtained with the classic Langmuir method can be in serious error. This is because inelastic collisions of electrons with atoms cause the EEDF to be depleted in the inelastic energy range compared to that in the elastic energy range. Druyvesteyn (1930) showed that any arbitrary but isotropic EEDF, $f_0(\varepsilon)$, where ε is the electron kinetic energy, can be determined from the second derivative of the electron repulsion part of the probe characteristic $V_p\leqslant V_0$. The actual form of this relationship depends on the normalization chosen for $f_0(\varepsilon)$. In the present paper we define the EEDF such that

$$\int_0^\infty \varepsilon^{1/2} f_0(\varepsilon)d\varepsilon=1, \tag{4.3}$$

in which case (Hershkowitz, 1989)

$$f_0(\varepsilon)=\frac{4}{n_e s_p e^3}\left(\frac{m_e}{2}\right)^{1/2}\frac{d^2 I_e}{dV_p^2}, \tag{4.4}$$

with $\varepsilon=e(V_p-V_0)$. This definition of the EEDF corresponds to the electron energy probability function.

Techniques for measuring the EEDF were developed in the 1960s and 1970s and further refined in the 1980s and 1990s (taking advantage of progress in semiconductor and digital electronics) to the point that these are now routine laboratory experiments, with high-resolution EEDF measurement possible over a wide dynamic range of three to four orders of magnitude (Godyak, 1990).

There are a variety of precautions and conditions for correct measurement and interpretation of Langmuir-probe data, which are addressed in numerous reviews (Chen, 1965; Cherrington, 1982; Hershkowitz, 1989; Waymouth, 1989; Godyak, 1990).

Langmuir probe theory is based on the following assumptions:

(a) The EEDF is Maxwellian.
(b) There are no electron collisions within the sheath that surrounds the probe. Since the sheath thickness is of the order of the Debye length λ_D, this condition corresponds to $\lambda_e\gg\lambda_D$, where λ_e is the electron mean free path.
(c) The plasma perturbation around the probe does not exceed that assumed in probe theory. The consequence of this requirement for a typical cylindrical probe of radius R_p and length L_p is the condition $\lambda_e\gg R_p\ln(L_p/2R_p)$.
(d) The maximum probe current $\sim I_{e0}$ is negligible compared to the discharge current.

The earliest Langmuir-probe measurements on lamps were by Druyvesteyn (1934), in low-pressure Na-Ne discharges. van Tongeren (1975) also made Langmuir-probe measurements on low-pressure sodium lamps. Easley (1951) was the first to apply Langmuir probes to measure the EEDF and electron densities in the positive column of mercury–rare-gas discharges, and Waymouth (1959) applied the technique in the negative glow region near an oxide-coated cathode.

Verweij (1961) conducted an extensive series of Langmuir-probe measurements of electric field and electron temperatures and densities in Hg-Ar fluorescent lamp discharges of internal diameter ID=36 mm, to complement the emission spectroscopy experiments of Koedam *et al.* (1963). Langmuir-probe measurements were recently performed on an electrodeless fluorescent lamp (ID=50 mm) similar to the Osram Sylvania ICETRON® (Godyak *et al.*, 2001; see Sec. VI.C.1.c). The wide parameter space covered by these experiments has enabled extensive comparisons of experimental measurements with model predictions (see Sec. VI.D.1).

V. DISCHARGE LAMP MODELING

A. Introduction

All gas discharges for lighting include a number of complex phenomena, and numerical models have been developed for close to half a century to assist in the understanding of the relationships between the different physical processes. Broadly speaking, there are three main classification of numerical models used for lighting: thermal models, power-balance models, and models of the electrode region. In general, these were developed

as stand-alone models, although there have been attempts to combine two or more of them into a single model.

A number of models have also been developed to describe the electric ballast, treating the lamp as a circuit component (Zissis *et al.*, 2001). These models generally use sophisticated commercial software to represent the ballast components, together with a rather empirical description of the discharge. Interesting results have been reported for fluorescent (Vos *et al.*, 1998) and HID (Antón *et al.*, 2002) lamps, but much of this work is company proprietary and details of such models are beyond the scope of this text.

Thermal models treat the discharge as a source of heat, often making empirical estimates of the components of the power balance [Eq. (3.2)] in order to estimate the heat flux to the walls and electrodes and thereby the temperatures in these regions. These models are particularly important for HID discharge lamps, which require arc tube temperatures of order 1000 K and above to maintain the correct metal-halide vapor pressure in the discharge, but which must avoid local overheating, with resultant damage to lamp materials and premature failure. Standard fluorescent lamps have a much larger aspect ratio (ratio of length to diameter) than HID lamps, with lower power density, and are much less susceptible to thermal problems. Compact fluorescent lamps, in which thin standard fluorescent lamps are bent to fit into a smaller fitting (Sec. VI.A), can be susceptible to "hot spots." The glass used in fluorescent lamps is much less tolerant of high temperatures than the fused silica or ceramic used in MH lamps.

Power-balance models endeavor to quantify all the components of Eq. (3.2) for a particular class of lamp, in order to predict the electrical characteristics and the efficiency of converting electrical power to useful radiation. They do this by solving a set of fluid equations for the main discharge (e.g., the positive column in fluorescent lamps, the arc region beyond the direct influence of electrodes in HID lamps). The choice of equations will depend on the lamp type and may include some or all of the following: Ohm's law [Eq. (3.1)], particle balance, fluid flow, and heat equations, as discussed in Secs. V.B, V.C, and V.D, respectively. For convenience, the discussion in these sections is limited to steady-state operation, i.e., time-dependent effects are ignored. The majority of lamp models (including those for rf lamps) fall into this category, and time-dependent behavior will be discussed in the appropriate sections later in the text. In order to solve these equations, some knowledge is required of the way radiation is transported in the discharge (Sec. V.E) and of rate and transport coefficients such as the electrical and thermal conductivity and viscosity (Sec. V.F). Models of electrodeless lamps (Sec. V.G) may also include the coupling between the rf or microwave source to the discharge through Maxwell's equations.

The arc region in HID lamps is close to local thermal equilibrium, which greatly simplifies models, since the particle energies of each species satisfy a Maxwell-Boltzmann distribution with approximately the same temperatures. The EEDF for most fluorescent lamps deviates strongly from a Maxwellian for the high-energy electrons (or "tail"), and in order to compute the appropriate rate coefficients, either a kinetic model or an adequate analytic approximation must be included (Sec. VI.D.1.d).

Models of the electrode region are important because energy losses in this region can represent a significant fraction of electrical power, particularly in short HID lamps. Models must therefore treat the electropositive sheath at the cathode and the thermal balance between the discharge and electrode.

The fundamental equations used for lamp models are presented below, and the way they are used in models of different lamp types is described in the appropriate sections.

B. Particle balance and diffusion

Each neutral species j with local density n_j diffuses through the discharge according to (Hirschfelder *et al.*, 1954)

$$\nabla \cdot N D_j \nabla \left(\frac{n_j}{N} \right) + S_j = 0, \tag{5.1}$$

where N is the total gas number density, D_j is the diffusion coefficient for species j through the gaseous mixture, and S_j is a term incorporating the rates of production or depletion of species j by interactions between electrons, ions, atoms, and molecules and radiation processes in the discharge. Equation (5.1) is fundamental to the modeling of the positive column in all low-pressure discharge lamps. In HID lamps, diffusion represents a small deviation of densities about the LTE values; direct solution of Eq. (5.1) is inappropriate and an alternative approach must be employed (Dakin *et al.*, 1989).

Electrons and ions must diffuse to the walls at equal rates to maintain charge neutrality, despite the higher mobility of the electrons (Sec. III.A.4). The influence of the resultant ambipolar field may be represented by the diffusion equation for electrons (for constant gas density),

$$\nabla \cdot D_a \nabla n_e + S_e = 0, \tag{5.2}$$

where D_a is the ambipolar diffusion coefficient and

$$D_i \ll D_a \approx \mu_i k_B (T_e + T_i)/e \ll D_e . \tag{5.3}$$

Here D_e and D_i are the electron and ion diffusion coefficients, T_e and T_i are the electron and ion temperatures, and μ_i is the ion mobility. Once again, Eq. (5.3) is an important component in fluid models of low-pressure discharges, but ambipolar diffusion requires special treatment in HID lamp modeling. [Note: Eq. (5.2) is strictly only applicable to systems with only one ionic species. The equations for multi-ion systems are more complex (Rogoff, 1985).]

C. Fluid flow and convection

Convective flows are described by the Navier-Stokes equation,

$$\rho\vec{v}\cdot\nabla\vec{v}+\nabla p+\rho\vec{g}=\nabla\cdot\eta_g\nabla\vec{v}, \tag{5.4}$$

where ρ and $p=Nk_BT_g$ are the gas density and pressure, T_g is the gas temperature, $\vec{v}$ is the fluid (or gas) velocity, $\vec{g}$ is the acceleration due to gravity, and η_g is the coefficient of viscosity. Convective flows are relatively unimportant in fluorescent lamps, but help determine the temperature distribution on the walls of HID lamps; Eq. (5.4) is an essential component in thermal models. Modeling of horizontally burning HID lamps must include the gravitational term, responsible for the bowing of the arc, which destroys axial rotational symmetry and hence requires a 3D representation. The gravitational term is also responsible for convective cells in vertically burning lamps.

D. Gas heating and thermal balance

The gases in all discharge lamps are heated by collisions between the constituent electrons, ions, atoms, and molecules, described by the heat equation

$$\nabla\cdot\kappa_g\nabla T_g+S_H-\rho C_p\vec{v}\cdot\nabla T_g=0, \tag{5.5}$$

where κ_g is the coefficient of thermal conductivity of the gas, S_H is the energy per unit volume dissipated as heat in the discharge, and C_p is the specific heat at constant pressure.

In fluorescent lamps, the source term S_H is calculated from the collision rates of electrons with ions and atoms in the discharge (see Sec. VI.D.1.e). The situation is more complex in HID lamps, where S_H is represented as the difference between the joule heating σE^2 and the net energy transported by radiation from or to each point in the discharge U_{rad},

$$S_H=\sigma_eE^2-U_{rad}. \tag{5.6}$$

When Eq. (5.6) is substituted in Eq. (5.5), the resulting equation is known as the Elenbaas-Heller equation. In principal, U_{rad} could be calculated from the radiation transport equations in the discharge (see Sec. V.D), but this is computationally intensive and in many models this term is estimated from experimental measurements or incorporated into an "effective thermal conductivity" (see Sec. VII.D.1.6).

E. Radiation transport

The discussion of radiation transport in lighting discharges is divided into two parts in this section. Trapping or imprisonment of resonance radiation in low-pressure discharges is described first, followed by a short overview of radiation transport in high-pressure discharges. The low-pressure case is simpler. Typically, a modeler is primarily interested in one or two resonance lines and in determining an effective or trapped decay rate for the upper level(s) of the resonance line(s). The spectral line shape, the density of absorbing atoms, and thus the absorption coefficient of a resonance can usually be approximated as independent of position in low-pressure discharges. If the spatial distribution of excited or resonance atoms can be approximated as a radiation transport equation with a fundamental-mode solution, then the radiation transport problem in a low-pressure discharge can be decoupled from the discharge model. Spectral line shapes, densities of absorbing atoms, and absorption coefficients are always strongly dependent on position in high-pressure discharges, and the modeling of radiation transport is tightly coupled to the total discharge model. For a more comprehensive discussion of various approaches to modeling radiation transport, see Molisch and Oehry (1998).

Treatments of resonance radiation trapping in low-pressure discharges starts from the Holstein-Biberman equation

$$\frac{dn_u(\vec{r},t)}{dt}=S_u(\vec{r},t)-n_u(\vec{r},t)/\tau_\nu - \int n_u(\vec{r}',t)(4\pi R^2)^{-1}\frac{\partial T}{\partial R}d^3r'/\tau_\nu, \tag{5.7}$$

where $n_u(\vec{r},t)$ is the density of atoms in the upper level of a resonant transition at location $\vec{r}$ and time t, $S_u(\vec{r},t)$ is the production rate per unit volume, τ_ν is the vacuum radiative lifetime of the excited level, and $\vec{R}=\vec{r}-\vec{r}'$ (Biberman, 1947; Holstein, 1947). The Holstein transmission function $T(R)$ is

$$T(R)=\int_0^\infty g(\nu-\nu_0)\exp[-\alpha_0Rg(\nu-\nu_0)/g(0)]d\nu, \tag{5.8}$$

where ν is the frequency, ν_0 is a line-center frequency, $g(\nu-\nu_0)$ is a normalized spectral line shape,

$$\int_0^\infty g(\nu-\nu_0)d\nu=1, \tag{5.9}$$

and α_0 is the line-center absorption coefficient.

This integro-differential transport equation is nonlocal in real space, which means that the concept of diffusion is of rather limited utility in describing the transport of resonance radiation except at very low opacity. Normal-mode solutions are well known for this equation, with several standard spectral line shapes and standard, highly symmetric geometries. In addition to the early work by Holstein (1947, 1951), we mention publications by van Trigt (1969, 1970, 1971, 1976a, 1976b) and by Irons (1979a, 1979b, 1979c) as examples of thorough work on plane-parallel and cylindrical geometries. Spherical geometry has been treated in some detail by Molisch *et al.* (1993). Analytic expressions for the trapped decay rate and fundamental-mode shape are available for cylindrical, plane-parallel, and spherical geometries with a pressure-broadened Lorentzian line shape, Doppler-broadened Gaussian line shape, and a few other line shapes. Many of the early results on radiation trapping were derived using analytic theory.

In most low-pressure discharges, the spatial profile of the production rate per unit volume is approximated by the spatial profile of the electron density. This often enables one to assume that only the fundamental-mode solution to the Holstein-Biberman equation is excited. For example, in cylindrical geometry the zero-order Bessel-function profile of the electron density is sufficiently close to the spatial profile of the fundamental-mode solution to the Holstein-Biberman equation that one may assume the excited atoms have a fundamental-mode spatial distribution with a unique trapped decay rate. This approximation is particularly convenient, since it decouples the radiation transport from the plasma model. The modeler need only replace the vacuum decay rate of the resonance level by the trapped decay rate of the fundamental mode.

Treatments of radiation trapping in a more complex geometry can be can be derived using either Monte Carlo methods (see, for example, Vermeersch and Wieme, 1991) or the "propagator function" method (Lawler *et al.*, 1993; Parker *et al.*, 1993). The self-reversed emission profile of a trapped resonance line can also be determined using these and other methods.

In the case of low-pressure discharges operated at high power density, as is the case in some electrodeless discharges, there is a possibility that the resonance atom excitation or production rate per unit volume may not mimic the fundamental-mode solution to the Holstein-Biberman equation and that higher modes may be excited. Research is continuing on radiation trapping in these conditions. If higher-mode solutions are important, this couples the radiation transport more strongly to the complete-discharge model. The propagator function method (Lawler *et al.*, 1991; Parker *et al.*, 1993) has a major speed advantage over Monte Carlo methods in a highly coupled model.

Higher-power-density lighting discharges also produce significant radial cataphoresis, which violates the assumption of a spatially uniform density of ground-level absorbing atoms. This effect changes the shape and decay rate of the fundamental-mode solution to the Holstein-Biberman equation (Curry *et al.*, 1999).

Payne *et al.* (1974) made an important contribution when they demonstrated that the assumption of complete frequency redistribution in the tradition of the Holstein-Biberman approach led to serious errors in a particular pressure regime, which is typically in the range of 0.1–1.0 torr. The physics of the radiation trapping is changed by the fact that the photon frequency may not be completely randomized across the spectral line shape during each absorption-emission cycle. The trapping is therefore more severe than predicted by the complete-frequency-redistribution approximation. Payne *et al.* constructed a modified, and more general, Holstein-Biberman equation that included the effects of partial frequency redistribution.

The problem of partial frequency redistribution has an additional dimension of complexity due to the fact that photon frequency must be tracked during the trapping simulation or calculation. This makes this problem much more difficult and less amenable to analytic techniques than that of complete frequency distribution. Post *et al.* (1986) solved for the fundamental mode of the more general transport equation, including partial frequency redistribution by using the Jefferies-White (1960) approximation. Partial frequency redistribution is particularly important for the 185-nm resonance line of Hg in many low-pressure lighting discharges, because of the short vacuum lifetime of the $6\,^1P_1$ upper level. For comparison to theory, Post *et al.* (1986) reported numerous experimental measurements of trapping of Hg 185-nm radiation. Some recent work has used Monte Carlo methods in a cylindrical geometry over a broad range of parameter spaces and distilled these results to analytic expressions for fundamental-mode trapped decay rates (Lawler and Curry, 1998; Lawler *et al.*, 2000; Menningen and Lawler, 2000). In these simulations, a more realistic treatment than the Jefferies-White (1960) approximation was used for the partial frequency redistribution, based on exact angle-dependent Doppler shifts in the absence of randomizing collisions (Lee, 1974, 1977, 1982). The resulting analytic expressions for the fundamental-mode decay rate were designed to connect smoothly to "exact" decay rates from analytic theory for certain limiting conditions and to reproduce Monte Carlo results at pressures where partial frequency redistribution is important. The expressions are applicable for Voigt line shapes from a combination of natural or radiative broadening, resonance collisional broadening, foreign or buffer-gas broadening, and Doppler broadening.

The modeling of radiation transport in high-pressure discharges is not as advanced as in low pressure discharges. One does not have to worry about partial frequency redistribution, since the photon energy is thermalized after each absorption. The additional complexities due to the position dependence of spectral line shapes, densities of absorbing atoms, and absorption coefficients have hindered progress, as has the need for a great deal more basic spectroscopic data in the case of MH lamps. We anticipate that major progress will be made in the next decade in modeling radiation transport and even in synthesizing complete emission spectra of various high-pressure lamps (see Sec. VII.D).

In modeling radiation transport in high-pressure discharges, one typically emphasizes the radiation field and determines the spectral radiance as a function of position, direction, and frequency. Spontaneously emitted photons are emitted with equal probability in all directions, such that the fraction of the photons emitted within a given solid angle $d\Omega$ is $d\Omega/4\pi$. This process is quantized by the radiation transport equation, which describes the variation in spectral radiance $\Gamma(\nu,s)$ (i.e., the power per unit area, per unit solid angle, per unit frequency ν) along a line of sight s in the discharge (Cayless, 1986):

$$\frac{d\Gamma(\nu,s)}{ds} = \alpha'(\nu,\mathrm{s})\left\{\frac{2h\nu^3}{c^2}\frac{n_u(s)g_l}{n_l(s)g_u} + \left(\frac{n_u(s)g_l}{n_l(s)g_u} - 1\right)\Gamma(\nu,s)\right\}, \tag{5.10}$$

where $\alpha'(\nu,s)$ is the effective spectral absorption coefficient, $n_u(s)$ and $n_l(s)$ are the density of particles in the upper and lower levels of the transition between levels u and l, g_u and g_l are the respective dengeneracies, h is Planck's constant, and c is the speed of light. The effective absorption coefficient $\alpha'(\nu,s)$ is the product of the position-dependent optical absorption cross section and the position-dependent lower level density. The position dependence of the optical cross section is due to spatially dependent spectral line broadening.

In an infinite medium in which the temperature is independent of position, global thermal equilibrium exists, and $d\Gamma(\nu,s)/ds \approx 0$. The blackbody or ideal-radiator law, in units of energy per second, per unit area, per steradian, and per hertz of bandpass is

$$\Gamma_{BB}(\nu) = \frac{2h\nu^3}{c^2}\left[\exp\left(\frac{h\nu}{k_B T}\right) - 1\right]^{-1}. \tag{5.11}$$

Therefore the radiation transport equation can be rewritten for systems in local thermal equilibrium in terms of the local temperature and the local blackbody spectral radiance:

$$\frac{d\Gamma(\nu,s)}{ds} = \alpha'(\nu,s)\left[1 - \exp\left(-\frac{h\nu}{k_B T}\right)\right] \times [\Gamma_{BB}(\nu) - \Gamma(\nu,s)]. \tag{5.12}$$

An important parameter is the *local optical depth* in the discharge, defined along a ray by the dimensionless parameter

$$\tau(\nu) = \int_0^D \alpha'(\nu,s')ds', \tag{5.13}$$

where D is the distance traversed by the ray. Simplifications to the theory may be obtained in two limiting cases, optically thick, $\tau(\nu) \gg 1$, and optically thin, $\tau(\nu) \ll 1$, but in general some form of averaging must be used to obtain this parameter, depending on the type of discharge.

F. Transport and rate coefficients

1. Electrical conductivity

The electrical conductivity in a dc discharge is defined through the second-order approximation to the Boltzmann equation (Shkarowski *et al.*, 1966),

$$\sigma_e = -\frac{2n_e e^2}{3m_e}\int_0^\infty \frac{\varepsilon^{3/2}}{\nu_m(\varepsilon)}\frac{\partial f_0}{\partial \varepsilon}d\varepsilon, \tag{5.14}$$

where $\nu_m(\varepsilon) = (2\varepsilon/m_e)^{1/2} N q_t(\varepsilon)$ is the collision frequency for electron momentum transfer,

$$N q_t(\varepsilon) = \sum_s n_s[q^s_{em}(\varepsilon) + q^s_{inel}(\varepsilon)] + n_e\frac{q_e(\varepsilon)}{\gamma_E}, \tag{5.15}$$

$q_t(\varepsilon)$ is the total electron transport cross section, n_s, $q^s_{em}(\varepsilon)$, and $q^s_{inel}(\varepsilon)$ are the density, elastic electron momentum-transfer cross section, and inelastic cross section for neutral species s, $q_e(\varepsilon)$ is the electron-ion momentum-transfer (Coulomb) cross section,

$$q_e(\varepsilon) = \frac{\pi}{\varepsilon^2}\left(\frac{e^2}{4\pi\varepsilon_0}\right)^2 \ln\Lambda,$$

$$\ln\Lambda = -\frac{1}{2}\ln\left(\frac{n_e e^6}{9(4\pi)^2(\varepsilon_0 k_B T_e)^3}\right), \tag{5.16}$$

ε_0 is the permittivity of free space, and γ_E is the ratio of the conductivity in a fully ionized plasma to that in a Lorentz gas (Spitzer, 1962). For a gas containing only singly charged ions, $\gamma_E = 0.582$ (Spitzer and Härm, 1953).

2. Thermal conductivity and viscosity

In the absence of experimental measurements, thermal conductivity and viscosity in a gas are determined from the intermolecular potentials between the molecules in the gas. For the particular case of the Lennard-Jones potential,

$$\Psi(r) = 4\varepsilon_{ij}\left[\left(\frac{\sigma_{ij}}{r}\right)^{12} - \left(\frac{\sigma_{ij}}{r}\right)^6\right] \tag{5.17}$$

[or in fact any potential of the form $\Psi(r) = \varepsilon f(r/\sigma)$], where ε_{ij} is the potential parameter and σ_{ij} is the effective collision diameter for species i colliding with species j, the transport coefficients may be defined in terms of so-called omega integrals $\Omega^{(k,l)*}(T^*)$, which are functions of a single dimensionless parameter $T^*_{ij} = k_B T/\varepsilon_{ij}$ and are therefore independent of the species in the gas. Tables of $\Omega^{(k,l)*}(T^*)$ are found in Hirschfelder *et al.* (1954).

The thermal conductivity and viscosity for a monatomic gas are given by (Hirschfelder *et al.*, 1954)

$$\kappa_g = \frac{75k_B\sqrt{k_B T/\pi m}}{64\sigma^2\Omega^{(2,2)*}(T^*)}, \tag{5.18}$$

$$\eta_g = \frac{5\sqrt{m k_B T/\pi}}{16N_A\sigma^2\Omega^{(2,2)*}(T^*)}, \tag{5.19}$$

where m is the mass of the gas atoms and N_A is Avogadro's constant. Note that the subscripts on σ, m, and T^* have been suppressed for a single-component gas. The coefficients for two-component gases are obtained by replacing m by $\bar{m}_{ij} = (m_i + m_j)/2m_i m_j$ in Eqs. (5.18) and (5.19), and those for multicomponent gases are obtained from linear combinations of these coefficients (Hirschfelder *et al.*, 1954; Muckenfuss and Curtiss, 1958).

Diffusion coefficients in a binary gas mixture, for species i diffusing thorough species j, are given by (Hirschfelder *et al.*, 1954)

$$D_{ij} = \frac{3\bar{m}_{ij}\Omega^{(2,2)*}_{ij}}{5N\Omega^{(1,1)*}_{ij}}\eta_{ij}. \tag{5.20}$$

G. Modeling of the electrode region

1. Electron emission at the cathode

The electron current density emitted at any point k on the cathode includes components due to thermal and field emission, i.e.,

$$j_e = j_{Th}(E_k, T_k) + j_{FE}(E_k, T_k), \tag{5.21}$$

where E_k and T_k are the electric field and temperature. The current density due to thermal emission $j_{Th}(E_k, T_k)$ (Nottingham, 1956) is

$$j_{Th}(E_k, T_k) = \frac{A_R T_k}{k_B} \int_{\phi_{\text{eff}}}^{\infty} \ln\{1 + \exp(-\varepsilon/k_B T_k)\} d\varepsilon, \tag{5.22}$$

where

$$\phi_{\text{eff}} = \phi - \Delta\phi \tag{5.23}$$

is the effective work function of the cathode, ϕ is the work function, and A_R is the Richardson coefficient of the cathode material, respectively, and the correction to the work function $\Delta\phi$ (Schottky, 1923) is

$$\Delta\phi = e\left(\frac{eE_k}{4\pi\varepsilon_0}\right)^{1/2}. \tag{5.24}$$

The current density due to field emission $j_{FE}(E_k, T_k)$ (Dyke and Dolan, 1956) is

$$j_{FE}(E_k, T_k) = \frac{A_R T_k}{k_B} \int_{-\infty}^{\phi - \Delta\phi} \ln\{1 + \exp(-\varepsilon/k_B T_k)\} \times \exp\left\{-\frac{6.83\times 10^9 (\phi - \varepsilon)^{3/2} \nu(y)}{e^{3/2} E_k}\right\} d\varepsilon, \tag{5.25}$$

where $y = \Delta\phi/(\phi - \varepsilon)$, and $\nu(y)$ is the Fowler-Nordheim function, originally tabulated by Nordheim (1928) and corrected by Burgess *et al.* (1953).

If the electric field E_k is insufficient to cause appreciable field emission current, $\Delta\phi \ll \phi$, Eq. (5.21) reduces to the Richardson equation

$$j_e = A_R T_k^2 \exp\left(-\frac{\phi_{\text{eff}}}{k_B T_k}\right). \tag{5.26}$$

2. Characterization of the cathode sheath

The form of the positive space-charge sheath determines the relationship between the electric field at the cathode E_k and the cathode fall voltage V_c. The small amount of ionization in the cathode sheath is neglected in the following discussions of inertia and collision-limited space-charge sheaths.

a. Collisionless sheath

If the ion mean free path in the sheath $\lambda_i \gg \delta_c$, where δ_c is the width of the sheath, the ion motion in the sheath may be treated as collisionless (Langmuir, 1929). Ions enter the sheath with the Bohm velocity (Bohm, 1949) corresponding to an energy $\varepsilon_{is} = k_B(T_e + T_i)$, where T_e and T_i are the electron and ion temperatures, respectively, at the sheath boundary and gain kinetic energy according to the change in electric potential across the sheath. Since $E_k^2 \gg E_s^2$, where E_s and E_k are the electric fields at the plasma-sheath boundary and cathode, respectively,

$$E_k^2 \approx 4\left(\frac{m_i}{2e\varepsilon_0^2}\right)^{1/2} j_i[(V_c + \varepsilon_{is})^{1/2} - \varepsilon_{is}^{1/2}], \tag{5.27}$$

where m_i is the ion mass. Since typically $T_i \ll 1$ eV and $T_e \leqslant 1$ eV, in general $\varepsilon_{is} \ll V_c$. The corresponding sheath width is

$$\delta_c^2 = \frac{4}{9}\left(\frac{2e\varepsilon_0^2}{m_i}\right)^{1/2} \frac{V_c^{3/2}}{j_i}. \tag{5.28}$$

b. Collisional sheath

In the limit $\lambda_i \ll \delta_c$, collisional sheath theory is appropriate. For the high values of E_k/N encountered at the cathode of discharge lamps, the cross section for ion collisions becomes independent of ion velocity and charge exchange collisions dominate. In this limit, the ion velocity $v_i = k^+ E^{1/2}$ where (Wannier, 1953; Davies *et al.*, 1966)

$$k^+ = \left(\frac{2e\lambda_{cx}}{\pi m_i}\right)^{1/2}, \tag{5.29}$$

λ_{cx} is the ion mean free path for charge exchange, and (Warren, 1955)

$$E_k^{5/2} = \frac{5 j_i V_c}{3\varepsilon_0 k^+}, \tag{5.30}$$

$$\delta_c^5 = \frac{500}{243}\frac{(k^+\varepsilon_o)^2 V_c^3}{j_i^2}. \tag{5.31}$$

In order to model the near-cathode region, some assumption must be made about the relationship of the electron and ion currents at the cathode, e.g.,

$$j_i = \beta j_e, \tag{5.32}$$

where β may be a function of the other parameters of the discharge, in particular the cathode fall voltage V_c (see Sec. III.A.5). The simplest assumption for this presheath region is that the electrons do not lose energy due to collisions in crossing the cathode sheath and enter the presheath with energy $\varepsilon = eV_c$. Assuming that losses due to radiation in the presheath region are negligible and all of this energy is converted to ionization of the background gas (Waymouth, 1982), then

$$j_e V_c = j_i \varepsilon_i / e, \tag{5.33}$$

where ε_i is the (average) ionization energy of the atoms in the discharge.

Equations (5.21), (5.32), and either Eq. (5.27) or Eq. (5.30) are a set of three equations in five variables, T_k, E_k, V_c, j_e, j_i. The total discharge current I is

$$I = \int (j_e + j_i) dA, \tag{5.34}$$

where the integration is over the current-emitting area of the cathode, which is a sixth independent variable. Self-consistent models of the electron region, therefore, couple the sheath region to the plasma equations and constitute a model for power dissipation in the cathode. The application of these models to particular lamps is discussed in the relevant sections.

H. Electrodeless lamp modeling

All electrodeless fluorescent lamp discharges are "overdense"—i.e., the applied frequency ω is smaller than the plasma frequency ω_{pe}, with electron densities 10^{17}–10^{18} m^{-3}, for which $\omega_{pe} \geqslant 2\times10^{10}$ s^{-1} ($\sim$3 GHz). These discharges also operate with electron momentum-transfer collision frequencies ν_m that are higher than the applied frequency (typically $\nu_m \approx 10^8$–10^9 s^{-1}). Therefore the particle kinetics of these discharges can be adequately treated by steady-state dc models, while their electrodynamics must take into account the inhomogeneity of the electromagnetic field, mostly due to the "skin effect." The collisional *skin depth* δ_s is (Weibel, 1967)

$$\delta_s = \frac{c}{\omega_{pe}}\left(\frac{2\nu_m}{\omega}\right)^{1/2}. \tag{5.35}$$

In all commercially available electrodeless lamps, the skin depth is of order of the lamp dimensions. In order to determine the coupling between the high-frequency source and the discharge, one solves Maxwell's equations in addition to the fluid equations. If the electric field $E \propto e^{i\omega t}$, then the electrical conductivity has both a resistive and a reactive component and Eq. (5.14) can be replaced by (Shkarowsky *et al.*, 1966)

$$\sigma_e = -\frac{2n_e e^2}{3m_e}\int_0^\infty \frac{\varepsilon^{3/2}}{[\nu_m(\varepsilon)+i\omega]}\frac{\partial f_0}{\partial \varepsilon}d\varepsilon. \tag{5.36}$$

VI. FLUORESCENT LAMPS

A. Introduction

Fluorescent lamps (see Waymouth, 1971; Abeywickrama, 1997) are low-pressure discharges, filled with a noble gas (usually argon, krypton, or neon, or some combination thereof) at a pressure of a few torr, with a minority of mercury (typically a few millitorr). They operate at gas temperatures of 300–700 K, with electron temperatures $\sim$11 000 K ($k_B T_e \sim 1$ eV). Up to 60–70 % of electrical power in these discharges is converted to UV radiation by mercury atoms.

Mercury vapor pressure is maintained at the optimum for maximum UV output by controlling the temperature of the coldest point on the lamp (the "cold spot"). In conventional fluorescent lamps, which utilize pure mercury, the optimum vapor pressure is $\sim$7 mtorr, corresponding to a cold-spot temperature $\sim$42 °C (Waymouth, 1971; Maya and Lagushenko, 1989). Alternatively, a mercury amalgam is often used, with its optimal vapor pressure at a different (usually higher) cold-spot temperature.

A phosphor is used to convert the UV to visible light, resulting in a total conversion efficiency of electrical power to visible light of $\sim$20–25 %. There is a wide range of available phosphors, which may be used in combination or in layers to provide any desired color temperature with CRI $\sim$80 (Soules, 1997).

Fluorescent lamps are typically long, thin cylinders—a standard T12 40-W fluorescent lamp is 120 cm long and 3.6 cm in diameter. Very short fluorescent lamps are inefficient because the energy loss in the electrode region is significant compared to energy converted to radiation. Compact fluorescent lamps are made by folding the discharge tube; the electronic ballast is often built into the lamp itself, with a base designed to fit into a regular incandescent lamp socket. Fluorescent lamps with a rectangular or oval cross section show some gains in efficacy over cylindrical lamps (Aicher and Lemmers, 1957, 1960), but due to manufacturing difficulties, such lamps have never been exploited commercially.

Standard fluorescent lamps operate at discharge current densities of typically 40 mA/cm^2. Recent developments in the lighting industry have led to the introduction of "highly loaded lamps" with up to a factor of 10 or more increase in current density. These include compact fluorescent lamps, narrow (5-mm ID) lamps for laptop computer backlighting, and some electrodeless lamps.

Inductively coupled (electrodeless) fluorescent lamps (see Sec. VI.C) have been developed in the last decade with considerable increase in lamp life due to the absence of electrodes. These lamps operate at lower buffer-gas pressures (where efficiency is higher) and higher electrical power density than would be sustainable in a lamp with electrodes.

B. Physics of electroded fluorescent lamp discharges

1. Energy and particle balance

Electrons emerging from the cathode are accelerated through the cathode fall into a region of relatively weak electric field, the *negative glow*. There is an overproduction of ions in the negative glow, which is compensated by a dark region of low ionization, the *Faraday dark space*. Following the Faraday dark space is a region of constant electric field, the *positive column*, and a bright anode glow is separated from the positive column by an anode dark space.

The positive column is the major source of UV radiation in fluorescent lamps. Electrons gain energy in the axial electric field, which is dissipated by collisions with atoms and ions in the gas, establishing a steady-state electron energy distribution (EEDF) with an effective electron temperature typically $\sim$11 000 K ($k_B T_e \sim 1$ eV).

The outstanding efficiency of Hg discharges in producing resonance radiation is in part due to the low excitation energy of the first excited configuration, which includes the resonance level (4.89 eV, slightly less than half the ionization energy of 10.4 eV). Excitations to the radiative level or neighboring metastable levels from the ground state thus provide channels for both radiation and two-step ionization to maintain the discharges. In contrast, rare gases have first-excitation configurations with resonance levels at excitation energies much greater than half the ionization potential. The densities of resonance atoms in rare-gas discharges tend to satu-

rate with increasing current, in part due to ionizing collisions between pairs of excited atoms (Miller *et al.*, 1971; Doughty and Lawler, 1983). Resonant atom densities in Hg rare-gas discharges also saturate with increasing current, but at a value that still allows greater than 50% conversion of electrical power to radiation.

An electron of any energy can have a superelastic collision (or collision of the second kind) with an excited mercury atom, in which the excited atom relaxes to a lower electronic level, and the colliding electron gains the kinetic energy corresponding to this transition. Inelastic collisions between excited atoms and other atoms and molecules (such as chemi-ionization) can also play an important role in the energy balance.

The efficiency of conversion of electrical power to UV radiation depends on the fraction of high-energy electrons in the EEDF, while the electrical characteristics are governed by the electrical conductivity, which is principally determined by the low-energy electrons. Elastic collisions of electrons with atoms and ions couple the electric power to the discharge through the electrical conductivity and provide gas heating, while electron-electron collisions redistribute the electron energy. In standard florescent lamps under normal operating conditions, the axial electron density is $n_e \sim 5\times 10^{17}$ m^{-3} (Verweij, 1961) and the ratio of electron density to gas density is $n_e/N \sim 5\times 10^{-6}$. Under these conditions, electron-ion collisions play a minor role in establishing the electrical conductivity, but the situation is radically different at higher currents, particularly in electrodeless discharges, in which rare-gas pressures are typically an order of magnitude lower than in standard fluorescent lamps and electron densities are up to an order of magnitude higher, such that $n_e/N \sim 5\times 10^{-4}$. Under these conditions, the extremely high cross section for Coulomb collisions at low energies ensures that they play an important role (see Sec. VI.D.1.b).

Electron-electron collisions ensure that the EEDF is close to a Maxwell distribution for energies below the threshold of the first excited state of mercury for standard operating conditions (Lister *et al.*, 2002). For higher electron energies, the tail of the EEDF is depleted by inelastic collisions. As power in the discharge increases, electron density increases, and electron-electron collisions may be sufficient for the EEDF to be Maxwellian even for higher electron energies (Maya and Lagushenko, 1989). This is illustrated in Fig. 11, which shows Langmuir-probe measurements of the EEDF in a Hg-Ar discharge of ID=5 cm as a function of discharge current (Godyak *et al.*, 2001). For a current of 0.5 A (somewhat below the current density in a standard fluorescent lamp) the EEDF has a Druyvesteyn character for low electron energies. At medium current densities, the EEDF is Maxwellian for electron energies less than 5 eV, while for discharge currents greater than 6 A the EEDF is seen to be close to Maxwellian for electron energies up to 9 eV, the limit of the probe measurements.

The noble gas in a fluorescent lamp serves a number of functions:

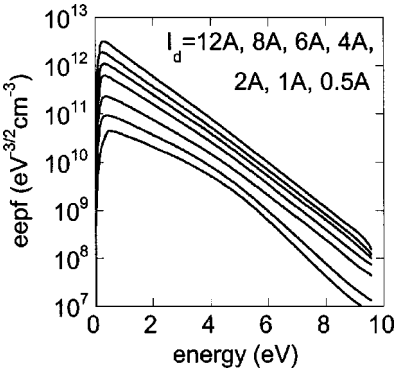

FIG. 11. Langmuir-probe measurements of the electron energy distribution function as a function of discharge current in an ICETRON-like discharge (ID=5 cm, p_{Ar}=300 mtorr, p_{Hg}=6.1 mtorr). From Godyak *et al.*, 2001.

(i) it controls the ambipolar diffusion rate, which in turn establishes the required balance between ionization of mercury atoms to maintain the discharge and excitation of mercury to provide UV radiation,
(ii) it acts as a buffer to reduce ion bombardment on electrodes and the phosphor coating, and also reflects and redistributes sputtered material back on the cathode, prolonging lamp life,
(iii) it helps in lamp starting by reducing the voltage required to initiate the discharge.

Radial cataphoresis (Sec. III.A.4) is important at low mercury vapor pressures and high discharge currents (Waymouth, 1971; Lister, 2003). The depletion of mercury atoms near the axis influences the performance of fluorescent lamps in three ways:

(i) the electrical conductivity of the discharge is reduced,
(ii) the spatial profile of the production rate per unit volume of resonance-level atoms is changed, influencing the production of 254- and 185-nm radiation,
(iii) radiation trapping near the axis is reduced, increasing the probability of photons' reaching the phosphor and being converted to visible light.

Axial cataphoresis occurs if fluorescent lamps are operated with direct current, causing the accumulation of mercury near the cathode. For this reason, fluorescent lamps must be operated on ac with no dc component.

Because gas pressures are a small fraction of an atmosphere, the principal loss process for ions and electrons is ambipolar diffusion to the walls, where they recombine to form neutral atoms. In standard lamps, operating at buffer-gas pressures of 3–5 torr, ionization losses are typically ~5% (Koedam *et al.*, 1963) and the principal nonradiative channel for energy dissipation is gas heating due to elastic-electron/neutral-atom collisions. As discharge current increases, these losses also increase and become greater than the radiation output at around 2 A (Kreher and Stern, 1988). Elastic-electron/neutral-

atom collisions are less important in electrodeless lamps, which typically operate at 300 mtorr buffer-gas pressures, and ionization losses may become significant. Elastic ion collisions with neutral atoms as they pass through the high ambipolar field near the boundary of the discharge also heat the gas. This effect is small ($<1\%$) in standard fluorescent lamps but can be significant in electrodeless lamps (Sec. VI.C.1.c).

For a given discharge current there is a unique value of the axial electric field in the positive column, and hence a unique discharge voltage at which the rate of ionization exactly equals the charged-particle diffusion losses to establish steady-state operation. The balance of diffusion losses and ionization may be influenced by the choice of noble gas, gas pressure, and discharge radius. Diffusion losses increase with decreasing molecular weight of the noble gas, decreasing gas pressure, and decreasing tube radius. Thus, for steady-state operation, the discharge voltage tends to be lower for krypton than for argon or neon, and lower for higher pressure and for larger tube radius. The situation is further complicated by the fact that there is an optimum gas pressure for maximum efficiency of UV production.

The design of a fluorescent lamp is subject to a number of constraints; the current must be sufficiently low to maximize lamp efficiency and minimize ballast losses, the length of the lamp should be minimized, and the lamp voltage must be sufficiently low that the lamp will restrike during brown-out conditions. The electric field in a standard fluorescent lamp operating with 400 mA in argon is a little less than 100 V/m (Verweij, 1961), which implies a length of a little over 1 m for a 40-W lamp. Electric fields are higher in the narrower discharges used in compact fluorescent lamps, but these lamps run at lower discharge currents and have a comparable total voltage.

The efficacy of the discharge is principally determined by the fraction of the total electrical power dissipated in the discharge that reaches the phosphor in the form of 254-nm radiation. For a standard 40-W fluorescent lamp operating at 400 mA discharge current and 3 torr argon pressure, 55% of the electrical power in the positive column is converted to 254-nm resonance radiation, 9% to 185-nm resonance radiation, 5% to visible and near-UV radiation, 20% dissipated through elastic collision loss, and 5% dissipated as diffusion (wall) losses (Koedam *et al.*, 1963). Electrode losses are typically $\sim 10\%$, so approximately 50% of the electrical power in the discharge is converted to 254-nm radiation. The efficiency of conversion of UV to visible light at near-unity quantum efficiency is about 50%, leading to luminous efficacies of 80–100 lm/W in commercial fluorescent lamps (Lister and Waymouth, 2001).

The radiation efficiency of circular-cross-section discharges decreases with increasing radius, primarily because the electron temperature also decreases (Ingold, 1991a). Gains in efficacy can be obtained by using oval or rectangular shapes (Aicher and Lemmers, 1957, 1960), such that the electron temperature is maintained as the cross section is increased. However, for aspect ratios greater than 3:1, the discharge is observed not to fill the tube, apparently due to an increase in ambipolar diffusion losses near the walls caused by two-step ionization (Ingold, 1991a). This would appear to preclude the use of fluorescent lamps in flat-panel applications.

Most fluorescent lamps operate on an ac (50/60 Hz) ballast. The anode fall (see Sec. III.A.5), and hence power losses near the electrodes, can be reduced by operating the lamp at a frequency above the ambipolar diffusion frequency (Dorlijn and Jack, 1985), typically 1 kHz. High-frequency operation also enhances the high-energy tail of the EEDF (Polman *et al.*, 1975), leading to increased radiation efficiency in the positive column. In practice, the gain of efficacy with increasing frequency appears to saturate at 15 kHz (Guest and Mascarenhas, 1997).

2. Radiation

UV resonance radiation at 254 nm is emitted from the $6p\,^3P_1$ energy level of mercury atoms, which has an excitation energy from the ground level, $6\,s^1S_0$, of 4.89 eV. This process is enhanced by mixing between the resonance level and two neighboring metastable levels—$6\,^3P_0$ (4.67 eV) and $6\,^3P_2$ (5.46 eV). A second resonance level ($6p\,^1P_1$) emits UV radiation at 185 nm, and there are a number of visible emissions (mainly in the blue and green) from higher excited levels radiating down to lower levels. These additional lines are particularly important in discharges at high power loading, such as the Philips QL® and Osram Sylvania ICETRON®, and attention must be given to the choice of phosphor to ensure optimum efficacy and color temperature.

There is generally little or no excitation of the noble-gas atoms under standard operating conditions, although this is not true in cases of strong cataphoresis. Mercury depletion in Hg-Ne lamps is a way of changing the emission spectrum (Bakker and Kroesen, 2000) by utilizing the red visible emission from neon, which is excited in the center of the discharge when mercury is absent.

Doppler broadening is the principal process that determines spectral linewidths in fluorescent lamps (Sec. III.A.3). The discharge has an optical depth τ of 50–100 at the center of the 254-nm resonance line, about unity for some of the stronger visible and near-UV lines, and much less than unity for other emission lines.

As mercury pressure increases, the number of atoms in resonance levels increases, but the imprisonment time of radiation also increases, and a greater fraction of the energy used in creating excited mercury atoms is dissipated in nonradiative transitions. The situation is complicated by the presence of seven isotopes in natural mercury, and the isotopic and hyperfine structure of the resonance lines plays an important role in radiation transport, reducing the trapping of the 254-nm radiation by a factor of 5 compared to the case of a single isotope (Walsh, 1957; Maya and Lagushenko, 1989). As noted in the previous section, radiation trapping is also reduced by radial cataphoresis.

Increases in lamp efficacy ~2–5 % have been obtained by isotopic altering of the Hg in fluorescent lamps (Maya *et al.*, 1984; Grossman *et al.*, 1986). The process involves adding the ^{196}Hg isotope, found only as a trace in natural mercury, but this has not been used commercially.

3. The electrode region

The cathodes in a fluorescent lamp are multicoiled helices of tungsten, the interstices of which are impregnated with alkaline-earth oxides for enhanced electron emission. During normal operation, they are heated by the passage of current through the tungsten wire of the helices and by ion bombardment from the plasma. The presence of excess barium dissolved in the mixed oxide crystals and at the surface makes the oxides semiconducting at typical operating temperatures and reduces the work function of the cathodes (Herrmann and Wagener, 1951), allowing them to supply current to the discharge at an operating temperature of 1200–1400 K. The cathodes operate in the spot mode, the position of the spot varying during the life of the lamp as the emissive material is locally evaporated and sputtered.

In the absence of a discharge, heated electrodes emit electrons in a process referred to as zero-field thermionic emission. For the alkaline-earth oxide cathodes this process depends on the pressure and type of buffer gas. The emission of an oxide cathode varies as the square root of the excess barium content at the surface of the BaO coating (Herrmann and Wagener, 1951). The excess barium content is in turn determined by the balance between a constant rate of production, through a classical reaction between BaO and the tungsten substrate, and a loss rate determined by evaporation and diffusion away from the cathode through the rare gas. The heavier the gas or higher the pressure, the slower the diffusion and the higher the barium pressure at the cathode for better emission.

When the discharge is operating, the positive space-charge sheath results in a high value of the electric field at the cathode surface. This is not sufficient for any significant field emission, nor is secondary emission due to electrons released by ion bombardment important. However, thermionic emission is enhanced by the *anomalous Schottky effect* (Nottingham, 1956; also known as the "patch effect") in addition to the normal Schottky effect described by Eq. (5.24). The patch effect is due to the inhomogeneity of the work function in the presence of a surface electric field. The zero-field work function ϕ may vary by ~2 eV from one crystal to another. If two neighboring crystals have work functions ϕ_1 and ϕ_2, the energy required for an electron in zero field to overcome the potential barrier is $(\phi_1+\phi_2)/2$. However, in the presence of an accelerating electric field at the cathode surface, the effective work function of the surface can approach the lesser of ϕ_1 and ϕ_2, leading to much more efficient emission than would be expected from the normal Schottky correction.

Visual observation of the cathode region shows the negative glow extending for about one tube radius on either side of the cathode and the Faraday dark space extending for a length slightly smaller than the tube diameter (Waymouth, 1971). No cathode dark space is visible, because the cathode sheath is extremely thin (~0.1 mm) and electrons from the cathode (referred to as *beam electrons*) enter the negative glow with the full energy of the cathode fall.

Waymouth (1971) deduced from Langmuir-probe measurements that the ion current represents about 30% of the total current at the cathode surface. In order to supply this current, the electron density must be significantly higher in the negative glow than in the positive column. There is a field reversal in the negative glow, which is established to balance the diffusion of ions and electrons in the region and to maintain constant current along the discharge (Druyvesteyn and Penning, 1940). The dependence of plasma density on discharge current is nonlinear, possibly due to variation in the ambipolar diffusion coefficient as a result of changes in the temperature of the cold trapped negative-glow electrons as the discharge current is varied (Wamsley *et al.*, 1991).

The buffer gas has a different role in the cathode region than in the positive column. The cathode-fall voltage in fluorescent lamp discharges is somewhat dependent on operating conditions, including the amount of auxiliary heating, but its maximum value never exceeds the excitation potential of the buffer gas by any appreciable amount. Buffer-gas excitation in the negative glow of Hg-Ne discharges is easily observable from a simple visual observation of the red color of this region and is readily observed in many Hg-Ar discharges by using a spectrometer (Walmsley *et al.*, 1993b).

Wamsley *et al.* (1990, 1993b) studied the role of buffer-gas excitation in the negative glow of a low-pressure Hg-Ar T-12 fluorescent lamp discharge at 400 mA current. Absorption measurements showed the absolute Hg^+ density in the negative glow to be a factor of 5 above that in the positive column, in reasonable agreement with published probe measurements (Waymouth, 1959; Coe *et al.*, 1993), while Hg^+ density in the Faraday dark space was a factor of 2 lower than in the positive column. This is consistent with the view of the negative glow and Farady dark space as "overshoot" and "undershoot" regions, respectively.

In contrast, the emission intensity from excited Hg was a factor of 2 lower in the negative glow than in the positive column, indicating that different mechanisms are important in different regions. Wamsley *et al.* (1993a, 1993b) modeled their spatial maps to explore the role of Penning ionization of Hg by excited Ar (see Sec. VI.D.1.a), but results were inconclusive, due to uncertainties in available Penning ionization rates.

These observations demonstrate that there remains a considerable lack of understanding of the physics of the near-cathode region. Excitation of buffer-gas resonance levels, followed by transport of the resonance radiation and eventual Penning ionization of Hg by the excited Ar, together with spatial redistribution of Hg due to the

intense localized ionization near the cathode hot spot, are processes that may have a large influence in this region, requiring further experimental and numerical investigation.

The anode sheath is typically ~ 0.25 mm, but for operation below 1 kHz the anode fall is subject to sawtooth oscillations (Waymouth, 1971). Fast electrons may cause significant ionization in the anode sheath, increasing the plasma density sufficiently for the anode to collect all the necessary current without the need for an anode fall. The anode fall collapses and the plasma diffuses away from the anode, causing the anode fall to become positive again, and the process repeats itself. For lamp operation above the ambipolar diffusion frequency (typically ~ 1 kHz), the negative glow formed during the cathode cycle does not have time to diffuse away during the anode cycle, and the pool of plasma remaining provides the required electron current without an anode fall. This phenomenon leads to an efficacy gain for lamps operated on an electronic ballast.

In fluorescent lamps operated at high currents, probes are sometimes attached to the electrodes, reducing the anode heating and increasing the area available for current collection. Another solution is to surround the electrode with a close-fitting shield to reduce the current channel and increase current density. The plasma density is thus enhanced, reducing the anode fall (Waymouth, 1971).

4. Role of impurities

The performance of all discharge lamps is adversely affected by the presence of water vapor, since it dissociates in the discharge, liberating hydrogen and oxygen. Hydrogen attacks the phosphor, while oxygen reacts with the electron emission coating, "poisoning" the cathode, and with mercury vapor, which forms solid deposits of dark mercury oxides on the phosphor surface. Hydrogen and water vapor also provide extra channels for power dissipation, through quenching of radiation by molecular interactions, or electron attachment, increasing the lamp ignition voltage in early life and in extreme cases preventing the lamp from igniting. As the lamp ages, however, ignition voltages are reduced due to reactions of impurities with the phosphor and electrodes.

C. Electrodeless fluorescent lamps

1. Inductive fluorescent discharge lamps

Inductively coupled discharges are currently the only form of electrodeless fluorescent lamp to be exploited commercially. As in other industrial applications, the discharge starts as a capacitively coupled E discharge, until sufficient toroidal electric field is present to create the high-density H discharge required to provide adequate light output. The starting phase in these lamps lasts only a few milliseconds and is therefore effectively instant for the user (Wharmby, 1993, 1997).

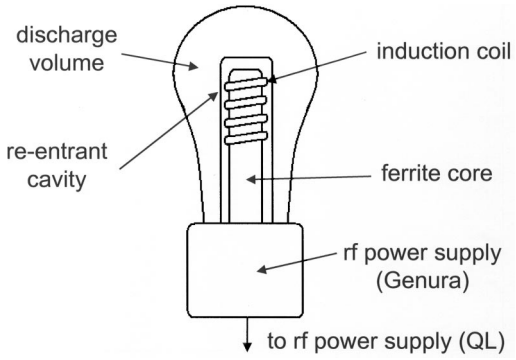

FIG. 12. Schematic of a reentrant cavity lamp (Philips QL® and General Electric *Genura*®).

a. Reentrant cavity lamps

The concept of the reentrant cavity lamp was introduced by Bethenod *et al.* (1936) and is illustrated schematically in Fig. 12. An insulated coil is wound several turns around a ferrite core and placed within the reentrant cavity. The application of an ac current activates the discharge. The high permeability of the ferrite core increases the magnetic flux surrounding the discharge and leads to more efficient coupling, but power losses in the ferrite increase at high temperatures and electric fields, although these are usually less than losses in a coil without a ferrite core. Additional phosphor coating on the reentrant can be used to enhance the production of visible light from UV transported to the inside of the lamp. The Philips QL® (Netten and Verheij, 1994) and General Electric *Genura*® (Wharmby, 1993, 1997) are examples of reentrant cavity lamps. Both operate at 2.65 MHz with a few hundred millitorr rare-gas pressure (the QL® uses argon and the *Genura*® krypton). The QL® is a highly loaded, high-lumen-output lamp for outdoor applications, and heating of the lamp ballast is reduced by separating the lamp and electronics via a shielded coaxial cable. The *Genura*® is the first compact electrodeless fluorescent lamp with integrated electronics and is intended as a high-efficacy direct replacement for incandescent reflector lamps. The lamp is internally coated with a transparent electrically conductive coating to reduce electromagnetic interference, and there is a further titanium reflective coating on the reentrant cavity and neck of the bulb. The phosphor coating is applied to the entire inside of the bulb. Recently Popov and Chandler (2002) described a reentrant cavity lamp without ferrite, operating with lamp power greater than 100 W at 200 kHz with a system efficiency of 85 lm/W.

The discharge in these lamps forms a bright ring around the reentrant cavity. Thomson-scattering measurements in a model QL® lamp (van de Sande and van der Mullen, 2002), operating at 85 W, with a bulb inside diameter of 11 cm and argon fill pressure of 300 mtorr, measured electron densities above 10^{19} m^{-3} (more than an order of magnitude higher than in standard fluorescent lamps) and typical electron temperatures around 11 000 K or $k_B T_e \sim 1$ eV (comparable with standard fluorescent lamps). The higher electron density leads to

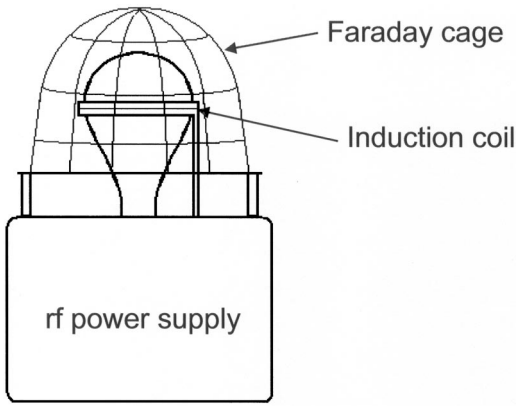

FIG. 13. Schematic of a lamp with outer coils (cf. Matsushita *Everlight*® lamp).

enhanced gas heating–laser absorption measurements of gas temperature (Jonkers *et al.*, 1997) showed a peak value of 550 K for these parameters.

b. Lamps with external coils

Lamps with external coils (Fig. 13) have the disadvantages that the coil blocks some of the light emitted from the lamp, and the lamp requires extra electromagnetic screening, such as the mesh screen used in the Matsushita *Everlight*® lamp (Shinomaya *et al.*, 1991). The *Everlight*® operates at the industrial frequency of 13.56 MHz using neon as a buffer gas to provide direct visible light during starting.

c. Toroidal lamps

Fluorescent lamps can also be operated using the principle of a ring discharge, similar to that of a tokamak in fusion research. In the ICETRON® lamp (ENDURA® in Europe), the discharge tube ring penetrates a ferrite core, with a primary winding to which rf power is applied. The discharge tube ring provides the single-turn secondary loop (Fig. 14). The voltage in the lamp is thus induced by a closed magnetic path. These lamps can operate at low frequency (100–500 kHz), which is attractive because of the low cost of electronics and easier restrictions on electromagnetic interference. Since the high-permeability closed magnetic core completely encloses the discharge current, coupling of rf power to the discharge is 98%, with a system efficiency including the ballast of ~85%.

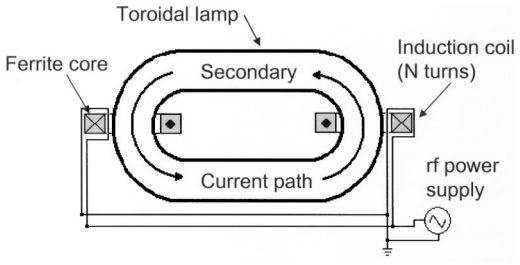

FIG. 14. Schematic of the ICETRON® (ENDURA®) lamp.

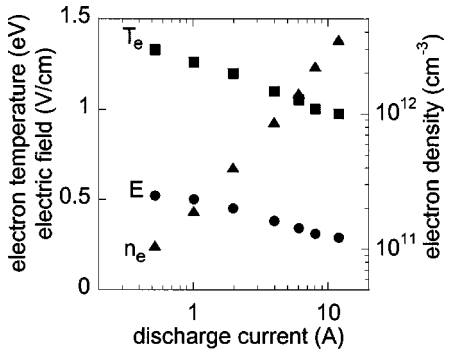

FIG. 15. Electron density, electron temperature, and electric field as a function of discharge current in an ICETRON-like discharge (parameters as in Fig. 11).

The concept of the toroidal lamp was invented by Anderson (1970), but early lamps required a large amount of ferrite, and heat losses in the ferrite ring resulted in unacceptably low efficacy. Godyak and Schaffer (1998) demonstrated that ferrite losses could be minimized provided the power loading was sufficiently high. They showed that the ratio of core losses W_c to the electrical power in the discharge W_{elec} is

$$W_c/W_{elec} \propto I^{-1.5}. \tag{6.1}$$

The 150-W ICETRON® lamp operates at 7.1 A, compared to 500 mA in the Anderson lamp, resulting in a reduction of more than a factor of 50 in ferrite losses. The operating frequency is 250 kHz, the lowest of all commercial electrodeless lamps, the tube minor diameter is 5 cm, the major dimension is about 35 cm, and the fill gas is 300-mtorr krypton. A smaller version of the lamp operates at 100 W and is filled with 300 mtorr argon.

The straight arms of the discharge are similar to the positive column of an electroded fluorescent lamp. Experiments have been performed on a model ICETRON® lamp, in which one of the arms was free of phosphor. The lamp exhibited the familiar "negative dynamic resistance" current voltage characteristic, and Langmuir-probe experiments (Godyak *et al.*, 2001) measured very high axial electron densities (3.5×10^{18} m^{-3} at 12 A) with electron temperatures ranging from 9500 to 19 500 K ($k_B T_e \sim 0.8$–1.7 eV) and electric fields in the range, 25–50 $V\,m^{-1}$ (see Fig. 15). These results and those of a complementary set of measurements of excited-state population densities for Hg $6p\,^3P_{0,1,2}$ and $6p\,^1P_1$ using white light absorption spectroscopy (Curry *et al.*, 2002) will be discussed in Sec. VI.D.

Integrating sphere measurements of a 100-W ICETRON® lamp at 4 A discharge current running under normal operating conditions show that 60–65 % of the electrical power in the discharge is converted to UV (254 and 185 nm) and 6% as visible light. Analysis of the experimental data using a numerical model (Sec. VI.D) indicates that elastic losses (electron and ion) comprise a further 11% and diffusion (wall) losses 13% of the discharge power. In this case, losses due to heating of the gas by elastic ion collisions with neutral atoms exceed

elastic electron collisions, in contrast to the situation in standard fluorescent lamps. Power dissipated in the ballast and ferrites contribute a further loss of 15%, resulting in a system efficacy of 85 lm/W.

2. Capacitively coupled fluorescent lamps

Attempts to drive capacitive rf lamps at a relatively low frequency (a few MHz) have failed due to high mercury absorption and sputtering at rf electrodes (or at the phosphor and glass when the electrodes are placed outside the discharge volume). This sputtering was caused by the dc component of the electrode sheath voltage, due to the rectification of the rf sheath voltage (cf. Lieberman and Lichtenberg, 1994).

It has been shown, however (Alexandrovich *et al.*, 1996), that rf driving of cold-cathode subminiature fluorescent lamps at higher frequencies (27 and 40 MHz) resulted in lower rf and dc sheath voltages than cathode sheath voltages for dc operation, with a significant increase of the lamp lm/W and longevity.

One of the first electrodeless fluorescent lamps was based on a capacitive discharge operating at 915 MHz (Proud and Smith, 1981), developed at GTE Laboratories. However, commercial exploitation of this device was limited by low system efficacy from the relatively inefficient microwave power supply. Improvements in the efficiency and lifetime of solid-state microwave sources, together with cost reductions, should make microwave lamps a commercial possibility in the future.

3. Surface-wave fluorescent discharge lamps

Electromagnetic surface waves can be used to sustain plasma columns (Moisan *et al.*, 1993, 1999). A device called a *wave launcher* is used to excite the plasma at one end of the discharge, and the wave travels along the plasma column that it sustains, as well as the dielectric media surrounding it. Experiments (Beneking and Andrerer, 1992; Rowley and Wharmby, 1992) showed that SWD to have the same efficiency as the positive column of a conventional fluorescent lamp. However, the efficiency gain due to the absence of electrodes was more than offset by the losses in generation of high-frequency rf or microwave power.

It was initially hoped that the atomic excitation in a surface-wave discharge would be concentrated near the discharge tube wall and thus reduce radiation trapping. This did not happen under fluorescent lamp conditions due to the nonlocal behavior of the distribution function (Kortshagen *et al.*, 1996). The axial nonuniformity of the discharge was a further disadvantage, leading to nonuniform light output.

D. Fluorescent lamp modeling

1. Positive-column models

Theoretical and numerical models of the positive column in fluorescent lamps have been developed for more than 40 years, following the pioneering work of Waymouth and Bitter (1956) and Cayless (1963). Since that time, all major lighting companies and a number of independent researchers have developed numerical programs with varying degrees of complexity. These models will be discussed in the text below, where appropriate. Models have provided valuable insight into the performance of fluorescent lamps, but have yet to realize their full potential in the design and optimization of these lamps. To some extent the models work best in the limited regions of parameter space for which they were optimized during their development, and they have reduced predictive capability in other regions of parameter space.

The aim of positive-column models is to predict the electrical characteristics, power balance, and radiation output in a fluorescent lamp as a function of discharge diameter, rare-gas type and pressure, discharge current, and mercury vapor pressure.

All models assume the positive column to be infinite in length, but particle densities may be calculated as radially averaged quantities (Winkler *et al.*, 1983a, 1983b; Kreher and Stern, 1988, 1989; Maya and Lagushenko, 1989) or the radial dependence may be included in a set of differential equations (Dakin, 1986; Zissis *et al.*, 1992; Lister and Coe, 1993; Petrov and Giuliani, 2003). The numerical methods required for these models are straightforward but their validity is limited by the availability of fundamental data (see Sec. V.D.1.a).

Models use either an analytic representation of the EEDF (Vriens *et al.*, 1978; Dakin, 1986; Maya and Lagushenko, 1989; Zissis *et al.*, 1992; Lister and Coe, 1993) or a direct solution of the Boltzmann equation to solve the electron kinetics directly (Winkler *et al.*, 1983a; 1983b; Kreher and Stern, 1988, 1989; Petrov and Giuliani, 2003) prior to computing rate and transport coefficients.

Positive-column models include Ohm's law [Eq. (3.1)], together with a set of particle diffusion equations [Eq. (5.1) for neutral particles and (5.2) for electrons] and the thermal conduction Eq. (5.5). Convection of the gas can be neglected. The equations are combined with the power-balance equation (3.2) to self-consistently calculate the electrical power dissipated as radiation, gas heating, and wall losses for a given set of discharge parameters. The way these equations are implemented in the numerical models is described in the following sections.

Fluorescent lamp diagnostics were discussed in Sec. IV. Of the large number of experimental measurements available for comparison with model predictions, the most comprehensive sets of data are for T12 (ID $=36$ mm) and ICETRON® (ID$=50$ mm). For T12, Langmuir-probe measurements of the electron density and temperature, EEDF and electric field (Verweij, 1961), and spectroscopic measurements of excited-state densities (Koedam *et al.*, 1963) have been made for argon pressures 0–20 torr, discharge currents 100–800 mA, and mercury pressures 0.5–90 mtorr. Similar measurements in ICETRON® lamps (Curry *et al.*, 2002; Godyak *et al.*, 2001) were made with an argon pressure of 300 mtorr at 20 °C for discharge currents 0.5–12 A

and mercury pressures 1–13 mtorr. These data sets will be used to complement the discussion of the modeling results described below.

a. Fundamental atomic data

The data used to characterize fluorescent lamps include the following.

(1) *Electron-impact excitation and ionization cross sections*. Until recently the available electron-impact excitation cross sections for mercury have been limited to the excitation from the ground state, from data assembled by Rockwood (1973), and augmented by estimates by Kenty (1950) for electron excitations between excited levels. Cross sections for ionization from excited levels were estimated from a formula by Vriens and Smeets (1980). These so-called two-step ionization processes become increasingly important as power loading in the lamp is increased.

The development of theoretical methods for calculating accurate electron-impact cross sections near threshold, and of computer programs to implement the methods, has raised hopes that the necessary data might be accurately calculated. Bartschat (2002a) has published electron-impact cross sections from ground-state mercury atoms to the $6p\,^3P_{0,1,2}$ and $6p\,^1P_1$ levels using a five-state semirelativistic Breit-Pauli R-matrix calculation. Cross sections for these excitations have also been calculated using the converged close-coupling method (Fursa *et al.*, 2003). Lister (2003) compared model results using each of the sets of cross sections above for typical ICETRON® parameters, and research is continuing to evaluate, improve, and extend these data.

(2) *Cross sections for elastic collisions*. The electron momentum-transfer cross sections for Hg and rare gases are important for numerical models of the positive column, since they play a major role in determining the electrical conductivity. In standard fluorescent lamps with rare-gas pressures around 3 torr, the cross sections for rare gases play the dominant role, although electron collisions with mercury atoms can be significant. For electrodeless fluorescent lamps operating at rare-gas pressures of a few hundred mtorr, collisions with mercury atoms are as important as those with rare-gas atoms due to the high electron momentum-transfer cross sections for mercury.

The recommended electron momentum cross sections for argon have been tabulated in the JILA database (Phelps, 2001). Until recently, models used cross sections for mercury from Rockwood (1973), but more accurate measurements (England and Elford, 1991) showed a resonance near 0.4 eV, leading to much larger cross sections than those previously used in this energy region.

(3) *Chemi-ionization cross sections*. Chemi-ionization was first included in models of the ionization balance of Hg rare-gas discharges by Vriens *et al.* (1978). There are two distinct processes:

$$\textit{Associative ionization} \quad \mathrm{Hg}^* + \mathrm{Hg}^{**} \rightarrow \mathrm{Hg}_2^{+} + e^-,$$

$$\textit{Penning ionization} \quad \mathrm{Hg}^* + \mathrm{Hg}^{**} \rightarrow \mathrm{Hg}^{+} + \mathrm{Hg} + e^-,$$

$$X^* + \mathrm{Hg} \rightarrow X + \mathrm{Hg}^{+} + e^-,$$

where Hg* and Hg** represent excited mercury atoms and X^* represents an excited rare-gas atom. It was suggested that Hg_2^{+} molecular ions could be a major component of the ion density at sufficiently high excitation temperature and Hg density. However, the cross section for dissociative recombination,

$$\mathrm{Hg}_2^{+} + e^- \_ \mathrm{Hg}^* + \mathrm{Hg}(^1S_0),$$

is also large (Vriens *et al.*, 1978), and the net increase in electron density by associative ionization is computed to be relatively small in standard fluorescent lamps (Zissis *et al.*, 1992; Lister and Coe, 1993).

Penning ionization involving two $\mathrm{Hg}(6\,^3P_2)$ atoms can, in principle, be an effective channel for electron production (Zissis *et al.*, 1992; Lister and Coe, 1993). Vriens *et al.* (1978) estimated this cross section to be 100 Å^2, while a value of 25 Å^2 was obtained by Sakai *et al.* (1989) from a Boltzmann-equation analysis of electron swarm data. Recent numerical calculations of the intermolecular potentials (Cohen *et al.*, 2002) indicated that the *total* cross section for Penning and associative ionization is much smaller than previously estimated. Since associative ionization should be the dominant process, it appears that Penning ionization for the two $\mathrm{Hg}(6\,^3P_2)$ atoms is a less important process in fluorescent lamps than previously thought.

(4) *Radiation transport parameters*. The transition probabilities of all the important mercury lines, with the exception of the 185-nm resonance line, have been measured by Benck *et al.* (1989). There have been numerous measurements of the 185-nm lifetime. The most recent measurement by Bousquet and Bras (1980) may be the most accurate, according to radiation trapping studies by Menningen and Lawler (2000). Resonance lines are also broadened by the rare-gas atoms, for which limited data are available, but measurements of broadening in argon have been reported (Bousquet and Bras, 1977).

b. Electrical characteristics

Ohm's law [Eq. (3.1)] describes the relationship between the electric field and discharge current, through the electrical conductivity σ_e [Eq. (5.14)]. Comparisons of experimentally measured electric fields with values calculated from models of the positive column (Dakin, 1986; Lister and Coe, 1993) for operating conditions in a standard fluorescent lamp (ID=36 mm, 3 torr argon pressure, 7 mtorr mercury vapor pressure) are shown in Fig. 16. Considering the uncertainties in cross-section data and experimental measurements, the agreement is quite good. However, Coulomb collisions between electrons and ions were neglected in calculating conductivity in these early models. These collisions become important at higher discharge currents, as can be seen from the following example.

To calculate σ_e we require the electron momentum cross sections, the EEDF, and the electron, rare-gas, and mercury density profiles. The dominant contribution to σ_e is from low-energy electrons, which are close to Max-

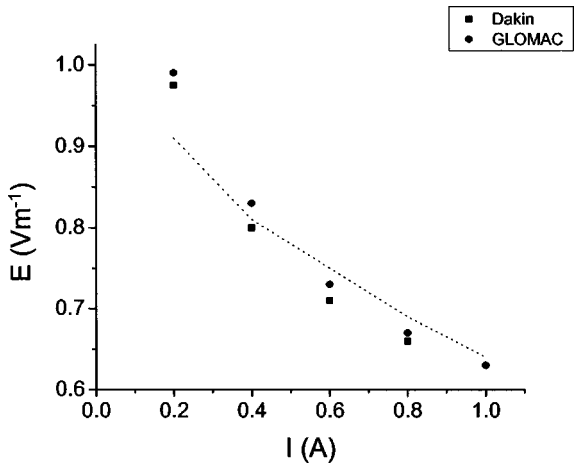

FIG. 16. Comparisons between experimental measurements of electric field (dotted lines) and numerical calculations from Dakin (1986) and GLOMAC (Lister and Coe, 1993) models for T12 lamps (ID=3.6 cm, argon pressure 3 torr, mercury pressure 7 micron) as a function of discharge current.

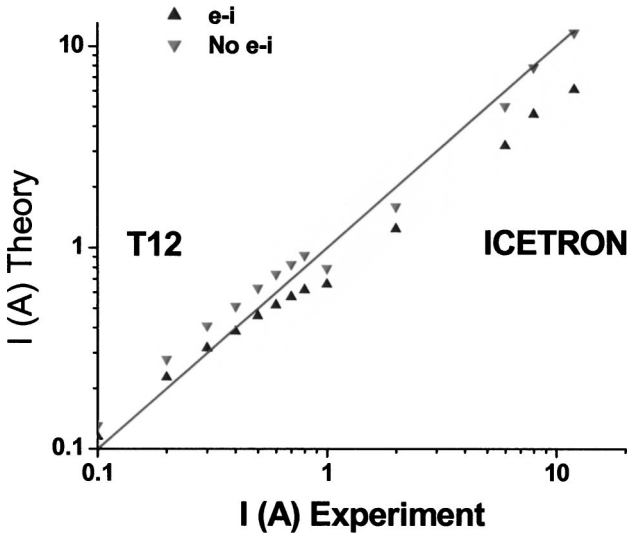

FIG. 17. Comparison of discharge currents in T12 and ICETRON® lamps calculated from Eq. (2.1) with the measured values. Calculations used the experimental measurements of electron density and temperature for T12 from Verweij (1961) and for ICETRON from Godyak *et al.* (2001).

wellian and characterized by the electron temperature T_e. The measurements of electron densities and temperatures in T12 lamps by Verweij (1961) and in ICETRON® lamps by Godyak *et al.* (2001) can be included in a simplified model to calculate gas and mercury densities and thence the electrical conductivity, assuming the electron density follows a zero-order Bessel function (Verweij, 1961).

From Eqs. (5.1) and (5.2), ignoring metastable atom diffusion (which represents about 1% of the ground-state density) and argon ionization,

$$D_{Hg}N\frac{d}{dr}\left(\frac{n_{Hg}}{N}\right)=-D_a\frac{dn_e}{dr}, \tag{6.2}$$

where D_{Hg} is the diffusion coefficient for ground-state mercury atoms. Since $D_a/D_{Hg}\sim T_e/T_g\gg 1$, ions diffuse out of the discharge faster than ground-state atoms diffuse back in, leaving a depletion of mercury in the center for any significant fractional ionization. There is also a correction to the total gas density N due to gas heating [Eq. (5.5) and the ideal gas law].

For standard 100-W ICETRON® operation (4 A discharge current, 6.1 mtorr Hg pressure, and 300 mtorr argon pressure), mercury density on axis is predicted to be about 85% of its value at the wall. If the mercury pressure is reduced to 1.2 mtorr, corresponding to a 20 °C cold spot, negative mercury densities are predicted on axis. This is clearly unphysical and implies that there is strong ionization of the buffer gas, which is incompletely treated in the model described here. The following discussion will therefore be restricted to cases in which argon excitation can be assumed to be negligible.

The discharge currents calculated for both T12 and ICETRON® lamps at 6.1 mtorr Hg pressure compared to the measured discharge current are illustrated in Fig. 17. There is considerable discrepancy between the calculated and experimental values for discharge currents above 600 mA in the T12 lamps and above 1 A in the ICETRON® lamps. For high currents in ICETRON®, the disagreement is close to a factor of 2. The importance of Coulomb collisions is also illustrated in Fig. 17—if they are excluded from the calculation, the agreement with experimental measurements is much better.

Kinetic models (Kreher and Stern, 1988, 1989) have reproduced the experimentally measured electric field for T12 lamps operating at discharge currents up to 3 A and pressures above 1 torr, but these models exhibit a similar discrepancy with Langmuir-probe measurements of electron density.

The above example illustrates the care with which results from experiments and models should be compared. The electric field can be reliably measured, and since it determines the total electrical power dissipated in the discharge, it is a more valuable parameter for comparison with modeling results than axial electron density.

c. Particle balance, diffusion, and radiation transport

The diffusion of neutral and charged particles through the discharge has been discussed in Sec. V.B. The source term for neutral species in Eq. (5.1) is

$$S_j=\sum_{j,k}(Q_{kj}-Q_{jk}+R_{kj}-R_{jk}), \tag{6.3}$$

where Q_{jk} is the rate per unit volume for inelastic collision processes involving an atomic transition from level j to level k, while R_{jk} represents the rate of loss per unit volume from level j to k through radiative decay. The equation for ground-state Hg atoms must be included in order to calculate the axial depletion of that state due to radial cataphoresis.

The most important inelastic collision processes are between electrons and atoms, for which

$$Q_{jk}=n_e n_j (2/m_e)^{1/2}\int_0^\infty q_{jk}(\varepsilon) f_0(\varepsilon)\varepsilon d\varepsilon, \tag{6.4}$$

where $q_{jk}(\varepsilon)$ is the cross section for a collision resulting in an atomic transition from level j to level k and ε is the energy of the impacting electron. The form of the EEDF $f_0(\varepsilon)$ is important in modeling the discharge and is discussed in more detail in Sec. VI.D.1.d. Associative ionization processes Q_{jk} can also be included in Eq. (6.4), replacing n_e by n_k and $f_0(\varepsilon)$ by a Maxwell-Boltzmann distribution at the gas temperature T_g. In principle, Q_{jk} should include "energy pooling," whereby collisions between mercury atoms in excited levels result in atoms in different atomic levels, but available data on these processes are poor.

The spatial distribution of radiating atoms in standard fluorescent lamps is close to the fundamental-mode solution of the radiation transport equation (Sec. V.E). The radiation term in Eq. (6.3) may then be written in the form

$$R_{jk}=\beta_{jk} n_j, \tag{6.5}$$

where β_{jk} is a position-independent constant, referred to as the *trapped decay rate* (actually the fundamental-mode decay rate), which depends on the average density of absorbing atoms, the gas temperature, the dimensions of the discharge, and the densities of atomic species responsible for broadening of the spectral lines. Under typical T12 lamp conditions the 254-nm line exhibits five relatively isolated, Doppler-broadened components due to the hyperfine and isotopic structure of the seven Hg isotopes. Until recently, Holstein's formula for a Doppler-broadened line was multiplied by 5 and used to describe the trapped decay rate of the $6\,^3P_1$ level (Walsh, 1957).

A recently developed partial-frequency-redistribution formula for trapped decay rates with a line shape dominated by Doppler, resonance collisional, radiative, and buffer-gas broadening (Lawler and Curry, 1998; Lawler *et al.*, 2000) has been modified and applied to the 254-nm line in Hg-Ar discharges (Curry *et al.*, 2002). It was found that dividing the Hg density by 5 in the formula, rather than multiplying the resultant trapped decay rate of the $6\,^3P_1$ level by 5, was a better method of representing isotopic structure in the radiation transport of the 254-nm line. Although the $6\,^3P_1$ decay is well described by the simple complete-frequency-redistribution approximation, the contribution of buffer-gas broadening to the Lorentz wings of the 254-nm-line components is not negligible. The foreign-gas broadening of the 254-nm line increases β_{jk} by only about 10% for ICETRON-like discharges, due to the low buffer gas pressure. However, for standard fluorescent lamps, operating at 3 torr argon, β_{jk} is a factor of 2 higher than the Holstein value obtained using the Walsh (1957) approximation. Curry *et al.* (1999) have parametrized the effect of a nonuniform distribution of ground-level atoms, like that produced by radial cataphoresis, on trapped decay rates within the complete-frequency-redistribution approximation.

The treatment of the isotopic structure and partial frequency redistribution for the 185-nm radiation is somewhat more complex than for other mercury lines, and a special formula, applicable only to this line, was developed from simulations (Menningen and Lawler, 2000). The Monte Carlo results and analytic expression for the 185-nm Hg line were compared with data from a trapped laser-induced-fluorescence experiment. This work confirmed and extended that of Post (1986) with the advantage that all results reduce to a simple formula for inclusion in the numerical models.

Koedam and Kruithof (1962) reported large discrepancies between the $6\,^3P_1$ densities deduced from absorption measurements and those deduced from direct measurement of 254-nm radiation intensity for both low and high values of argon pressure, with agreement only near 3 torr argon pressure. If the more recent value for the transition probability of the 435.8-nm line (Benck *et al.*, 1989) is used to deduce $6\,^3P_1$ densities from the experimental measurements, and foreign-gas broadening (Lawler *et al.*, 2000) is included in the interpretation of the 254-nm radiation transport, this discrepancy is reduced to $\sim$10% or less for argon pressures between 0.1 and 15 torr.

Numerical models (Dakin, 1986; Zissis *et al.*, 1992; Lister and Coe, 1993) have reproduced the experimentally measured $6\,^3P_{0,1,2}$ densities (Koedam and Kruithof, 1962) in standard fluorescent lamps to within about 20%. However, calculated densities in ICETRON-like discharges were found to be a factor of 3 higher than the experimentally measured values (Curry *et al.*, 2002). A similar discrepancy was found in independent calculations by Petrov (2002). Using three different sets of data (Rockwood, 1973; Bartschat, 2002b; Fursa *et al.*, 2003), together with EEDF measurements from the Langmuir probes, Lister (2003) showed that the results were relatively independent of the choice of available cross sections. This suggests that a mechanism for depopulating these levels, such as the ladderlike ionization described by Wani (1994), is missing from the models. The importance of excitation to higher levels in these discharges was qualitatively discussed by van Dijk *et al.* (2000).

The source term for ambipolar diffusion [Eq. (5.2)] contains only the ionization terms Q_{ji}, since volume recombination can be neglected. Associative ionization may be included in the same way as in the diffusion equations for excited states

d. EEDF

A number of positive-column models (Maya and Lagushenko, 1989; Zissis *et al.*, 1992; Lister and Coe, 1993) have used an approximation for the EEDF proposed by Lagushenko, in which the main assumptions are

(i) Electron-electron collisions dominate all other collision processes for $\varepsilon \leqslant \varepsilon_1$, where ε_1 is the energy of the first excitation level of mercury, and the EEDF may be approximated by a Maxwellian distribution in this range.

(ii) For $\varepsilon > \varepsilon_1$, only excitation and ionization from the ground state and superelastic collisions to the ground state play a significant role in the EEDF.

For further details of this approximation and its application to fluorescent and neon lamps, see Maya and Lagushenko (1989) and Lister *et al.* (2002).

An alternative approach to the Lagushenko approximation for the EEDF is the two-electron-group model, developed by Morgan and Vriens (1980) and extended by Dakin (1986). This model assumes that the bulk electrons ($\varepsilon \leqslant \varepsilon_1$) may be described by an electron temperature T_b, while the tail electrons ($\varepsilon > \varepsilon_1$) may be described by a second electron temperature T_t.

Yousfi *et al.* (1990) have compared results using the above approaches with the solution of the compete zero-order Boltzmann equation for standard fluorescent lamp conditions, and their results indicate that the Lagushenko approximation in this case tends to underestimate the depletion of the high-energy tail, whilst the two-temperature approach overestimates the depletion.

Most EEDF calculations to date have been based on the local approach, in which the EEDF is assumed constant across the discharge. The influence of the local ambipolar electric field on the EEDF in low-pressure discharges for lighting is not clear. The local theory is only strictly applicable if the electron energy relaxation length is $\lambda_\varepsilon \ll R_D$, where R_D is the discharge radius (Kortshagen *et al.*, 1996). In fluorescent lamp discharges, for low-energy electrons, *elastic* collisions have a relaxation length $\lambda_\varepsilon \gg R_D$, and nonlocal theory is applicable, while for high-energy electrons, *inelastic* collisions have a relaxation length $\lambda_\varepsilon \approx R_D$. Nonlocal and local models are equivalent for Maxwellian distribution functions, which is approximately the case in highly loaded fluorescent lamps (Godyak *et al.*, 2001). Petrov and Giuliani (2003) recently applied a kinetic model as a function of radius to T12 lamps and concluded that the dependence of the EEDF on radius is neither local nor nonlocal.

Comparisons of experimentally measured electron temperatures with calculated values at standard operating temperatures (42 °C or 7 mtorr mercury vapor pressure) are shown in Fig. 18. The computed electron temperature using the analytic EEDF models (Dakin, 1986; Lister and Coe, 1993) is consistently higher than the experimentally measured values. Petrov and Giuliani (2003) found much better agreement using a kinetic model.

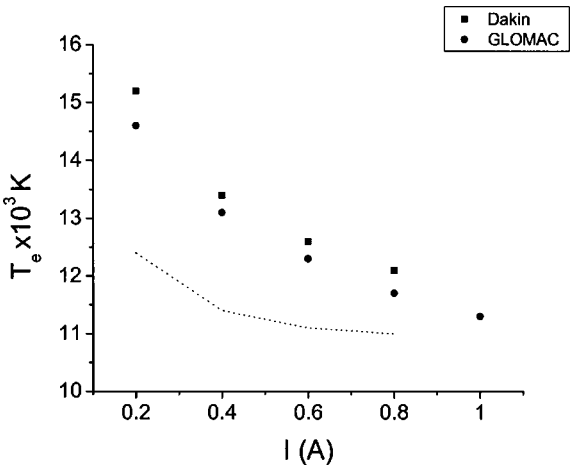

FIG. 18. Comparison of calculated and experimentally measured electron temperatures for the same parameters as Fig. 16.

e. Power balance

The source term S_H in the heat Eq. (5.5) for the positive column contains terms due to elastic collisions of electrons with atoms and ions (Kenty *et al.*, 1951; Lawler *et al.*, 1991), as well as heating due to ion-atom collisions as they drift through the ambipolar field E_r, i.e.,

$$S_H(r) = \left(\frac{2}{m_e}\right)^{1/2} n_e \int_0^\infty \sum_s n_s q_t^s(\varepsilon) \times \frac{2m_e}{m_s}\left(\varepsilon - \frac{3k_B T_g}{2}\right)\varepsilon f(\varepsilon)\, d\varepsilon + e n_e \mu_i E_r^2, \tag{6.6}$$

where $q_t^s(\varepsilon)$, m_s, and n_s are the total electron momentum-transfer cross section [Eq. (5.15)], atomic mass, and gas density for species s, respectively, and

$$E_r = -\frac{k_B T_e}{e n_e}\frac{dn_e}{dr}. \tag{6.7}$$

The total power per unit length dissipated by gas heating is then

$$w_{heat} = 2\pi \int_0^{R_D} S_H(r) r\, dr. \tag{6.8}$$

The total power per unit length from the radiative transition $j \to k$ escaping from the discharge is

$$w_{rad}(\lambda_{jk}) = \frac{2\pi h c \beta_{jk}}{\lambda_{jk}} \int_0^{R_D} n_j(r) r\, dr, \tag{6.9}$$

where λ_{jk} is the radiated wavelength for the transition $j \to k$.

Losses to the wall are the sum of diffusion of metastable atoms and ions to the wall, i.e.,

$$w_{wall} = w_{meta} + w_{ion}. \tag{6.10}$$

The power dissipation per unit length in the positive column due to metastable atom diffusion to the wall w_{meta} is

$$w_{meta} = 2\pi R_D \sum_j \varepsilon_j \Gamma_j(R_D), \tag{6.11}$$

where ε_j is the excitation energy of the metastable level and the flux density of metastable atoms to the wall is

$$\Gamma_j(R_D) = -D_j N \frac{d}{dr}\left(\frac{n_j}{N}\right). \tag{6.12}$$

The power dissipation per unit length in the positive column due to charged-particle diffusion to the wall w_{ion} is (Lister *et al.*, 2000)

$$w_{ion} = 2\pi R_D (\varepsilon_i + \varepsilon_w + e V_w)\Gamma_i(R_D), \tag{6.13}$$

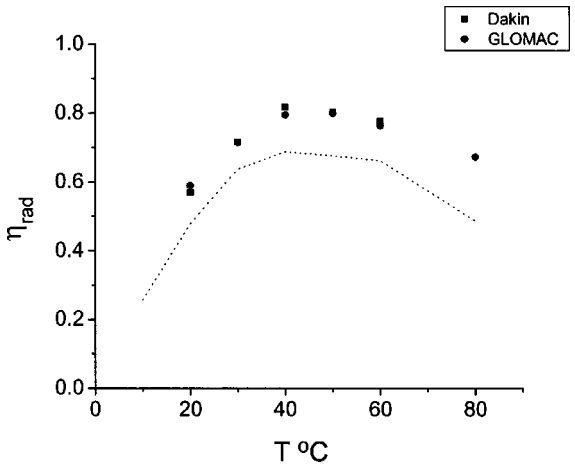

FIG. 19. Efficiency of radiation production in a standard T12 positive column (400 mA, 3 torr argon) as a function of cold-spot temperature.

where ε_i is the ionization energy of the atom from the ground state, $\varepsilon_w = 2k_B T_e$ is the average energy of electrons striking the wall,

$$\Gamma_i(R_D) = -D_a \frac{dn_i}{dr} \tag{6.14}$$

is the ion flux, and V_w is the potential drop across the positive space-charge sheath at the wall. For a Maxwell-Boltzmann electron distribution,

$$V_w \approx \frac{k_B T_e}{2e} \ln\left(\frac{m_i}{2\pi m_e}\right). \tag{6.15}$$

One of the important successes of modeling standard fluorescent lamps is the ability to qualitatively reproduce the observed variation in efficiency of converting electrical power to radiation with mercury vapor pressure (cold-spot temperature T_c), illustrated in Fig. 19. The experimental results are from Koedam *et al.* (1963). Two different calculations are represented, from Dakin (1986) and Lister and Cox (1992). The optimum vapor pressure is found to be at 42 °C in standard lamps. Both models represent reasonably well the increase in radiation efficiency as vapor pressure (and therefore density of resonance Hg atoms) increases above 10 °C to just below the optimum. At high mercury vapor pressures, increased radiation trapping due to an increase in the number of absorbing ground-state Hg atoms leads to a sharp decrease in radiation efficiency, which is somewhat underestimated by the models, possibly due to deviations of the resonance-state density profile from the fundamental mode.

Cayless (1960) and Ingold (1991a) developed simple 2D models to describe noncircular fluorescent lamps, for possible application to flat-panel lamps. They calculated the efficiency of producing radiation as a function of aspect ratio and reproduced the experimentally observed maximum at 3:1, which Ingold attributed to two-step ionization.

2. Models of the electrode region

Modeling of the electrode region in HID lamps has received considerable attention recently (see Sec. VII.D.2), but there has been significantly less activity in modeling of this region in fluorescent lamps. Soules *et al.* (1989) used a simplified thermal model and representation of the cathode sheath for both dc and ac to predict the formation of cathode spots. The oxide-coated cathode and the two lead wires were each represented as cylinders. Despite the simplifications of the model, which included empirical values for the effective work function and second ionization coefficient, the results qualitatively reproduced pyrometric measurements of the cathode temperature. Haverlag *et al.* (2002) developed a model to study ignition in lamps operated on high-frequency electronic ballasts, in which the coil was represented by a series of concentric discs.

Modeling of the negative glow was motivated originally by the prospect of using this region as a standalone light source, but such lamps proved to be inefficient. An early model by Cayless (1958) treated a discharge with no positive column and ignored the contribution of the fast electrons emerging from the cathode fall. Later models (Ingold, 1991b; Coe and Lister, 1992; Coe *et al.*, 1993) were directed at understanding the physics of the negative glow, with the hope of tailoring the region to provide a positive I-V characteristic, eliminating the need for a ballast.

Ingold (1991b) developed a two-electron (beam and plasma) model to investigate the properties of the near-cathode region as a function of discharge radius and electron and ion temperature. He included the axial ambipolar diffusion of the plasma electrons and plasma ionization by the beam electrons. The model predicted two field reversals, one at the cathode end of the negative glow, where the discharge current is supported by ambipolar diffusion, and the second at the end of the Faraday dark space, where axial ambipolar diffusion is insufficient to maintain the discharge current in the positive column. The model also predicted many of the experimentally observed quantities, including the length of the near-cathode region, axial distribution of electron density, and ion current to the cathode.

Coe and Lister (1992) developed a similar model, but included two-step ionization and ionization of the buffer gas. This model was later extended (Coe *et al.*, 1993) to calculate the electron temperature in the cathode region self-consistently, using the known properties of the positive column as a boundary condition. Results of the model were in reasonable agreement with Langmuir-probe measurements.

3. Models of electrodeless lamps

a. Inductively coupled discharge

The fundamental properties of an inductively coupled discharge in a reentrant cavity lamp are illustrated in Fig. 20(a), from a 1D model (Lister and Cox, 1992). The inductive coil is assumed to be infinitely long and the plasma forms the secondary loop of a transformer. Fig-

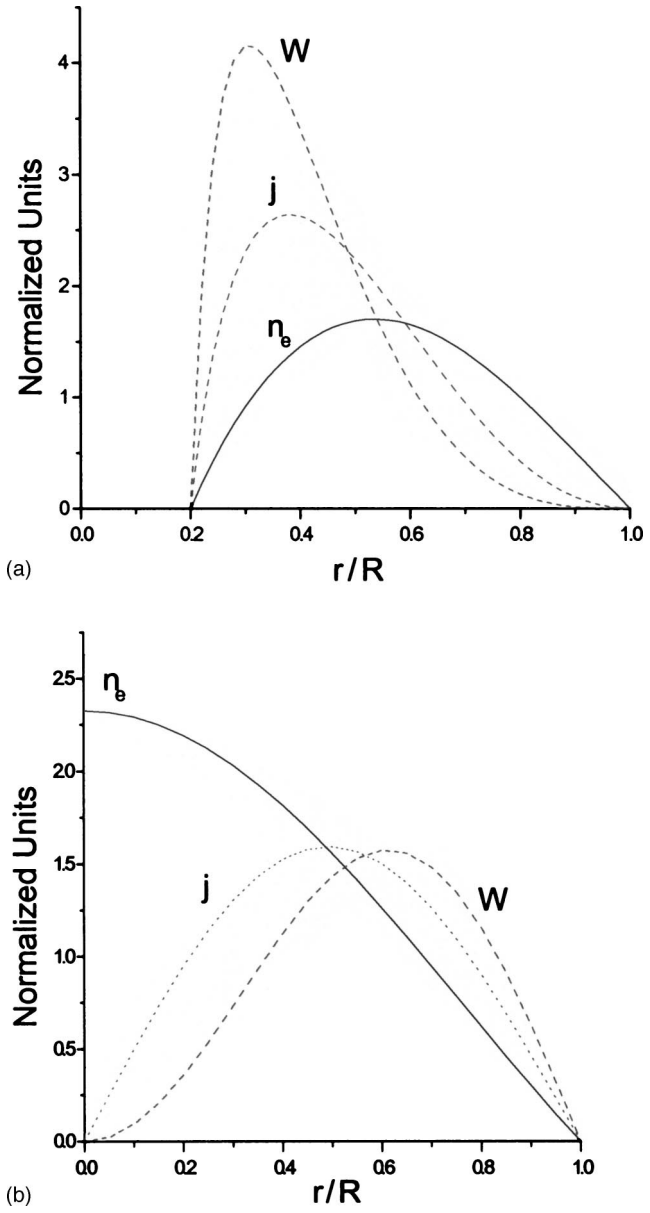

FIG. 20. Radial profiles of normalized electron density n_e, current density j, and power density jE_ϑ in an inductively coupled discharge calculated using a 1D (infinite-length coil) model (Lister and Cox, 1992) with (a) internal coils, (b) external coils. All quantities are normalized to their volume-averaged value across the radius.

ure 20(a) was obtained by integrating Maxwell's equations, assuming a simple Schottky model for the ambipolar diffusion, with zero electron density at both the reentrant cavity wall and the outer wall. In contrast to conventional fluorescent lamps, the electron density has a maximum near the center of the annular ring forming the discharge, and the electrical power dissipated in the discharge is concentrated near the reentrant cavity wall. Experimental measurements in Philips QL® lamps (Jonkers *et al.*, 1997) show relatively high gas temperatures near the reentrant cavity wall leading to mercury depletion in this region.

The fundamental properties of an inductively coupled discharge in a lamp with an external coil are illustrated in Fig. 20(b), also obtained from a 1D transformer model (Denneman, 1990; Lister and Cox, 1992). In this case, the electron density is peaked at the discharge axis, but power dissipation is now peaked towards the outer wall, due to the geometry and skin effects.

It was noted in the previous section that modeling of ICETRON® lamps has dealt only with the straight arms of the discharge, assuming that the physics of this region may be approximated by that of the positive column in a standard fluorescent lamp. No attempt has been made to model the coupling between the ferrite core and the discharge.

b. Capacitive discharge

Beneking (1990a) analyzed the impedance and emission properties of a capacitive discharge in Hg-Ar mixtures, for a range of frequencies, rf power, and gas pressure. His conclusions, supported by results from a numerical model (Beneking, 1990b), are that much of the nonradiative power loss can be explained by the space-charge-limited ion current across the sheaths. Excitation of Ar at the sheath boundary and dielectric losses in the walls of the lamp provide additional loss mechanisms. Results confirm that a capacitive discharge can compete with conventional fluorescent lamps only at relatively low power loading and high frequency (100 MHz and above).

E. Lamp electrical circuit system

Fluorescent lamps operate on ac, and the necessary current limiting impedance provided by the ballast can be reactive rather than resistive. [Note: Fluorescent lamps cannot be operated on continuous direct current due to axial cataphoresis (Sec. II.A.4), which causes the mercury to accumulate at the cathode.]

1. Lamp starting

In fluorescent lamps, there are three principal methods used to achieve the high voltage required to reach ignition: the glow starter switch, rapid-start ballast, and instant-start ballast.

The glow starter switch is used in most of the world except in the United States. A small glass bulb containing two bimetal contacts is filled with a low-pressure gas and mounted, together with a capacitor, in a container with two contact pins. Before switching on, the bimetal contacts are separated by a small gap. On ignition, a glow discharge forms and the contacts heat and bend towards each other until they touch, extinguishing the glow discharge and providing relatively large current through the ballast and electrodes, which warms the cathode coils. Since the circuit is inductive, a high-voltage pulse (600–1500 V) is produced across the ends of the lamp when the cooling contacts open, which rapidly ionizes the gas, and current flows between the lamp electrodes. This "glow-to-arc" transition is associated with enhanced secondary emission of electrons at the cathode (Waymouth, 1971). If the pulse fails to ignite

the lamp, the process is repeated, leading to a repeated flicker. During normal operation the lamp voltage is too low to cause a discharge in the starter switch.

In the United States, either rapid-start or instant-start systems are used. In rapid-start ballast systems, individual filament transformers wound on the ballast core continually supply 3.75 V to the cathodes, and the resulting current flow heats them to the temperature required to provide sufficient electrons to initiate the breakdown process. This represents an additional system loss of 2.5 W in a T12 fluorescent lamp.

Instant-start ballasts apply a high voltage across the lamp terminals when the lamp is switched on and the electrodes are cold. The high voltage results in increased "sputtering" of material from the electrodes, which reduces lamp life, but increases efficacy due to the absence of a heater current.

van den Hoek *et al.* (2002) reported that lamps operated at 50 Hz experienced two modes of starting—the normal glow-to-arc mode and a second vapor-arc mode, a contracted arc associated with fast (μs) dielectric breakdown and cathode spot temperatures of 2500 K, which are particularly damaging for electrode life.

2. Continuous operation

The power loss in a magnetic ballast is typically 6 W per lamp. System efficiency can be improved by the use of electronic ballasts with semiconductor components and by operating the lamps at $\sim$25 kHz frequency. Impedance losses can be reduced at these frequencies, and the lamp itself is more efficient because the discharge is maintained throughout the main cycle, reducing electrode losses. The considerably higher cost of electronic ballasts is compensated by improved lamp efficacy. An important commercial benefit is the lack of light fluctuations at the supply frequency and its first harmonic.

3. End of life

Lamp life is primarily determined by the erosion of electron emission material from the cathodes. The process of ignition results in momentarily enhanced erosion, and lamp life is adversely affected by increasing numbers of ignitions per thousand burning hours. A lamp that is ignited and never switched off would last about four years, while one that is started once per minute of operation would last 2000–5000 starts—roughly a hundred hours. Lamps requiring many ignitions per hour are operated on ballasts supplying continuous filament heat, even when the lamp is not operating, to minimize damage to the electrodes at starting.

As fluorescent lamps approach the end of their service life, the electron-emitting coating on the electrode coils becomes depleted. This generally occurs at one electrode first, and the power increases dramatically in an attempt to maintain the discharge current. The excessive heat generated at the worn coil may cause it to break and result in melted sockets or cracked lamp glass, particularly in small-diameter lamps (such as compact fluorescent lamps), which are powered by high-frequency electronic ballasts. In such cases, the ballast must include the capability to sense end of life. Company proprietary technologies have also been developed for lamps themselves to sense end of life and self-extinguish.

F. Fluorescent lamp materials

1. Electrodes

Loss of emitter material occurs mainly as a result of evaporation during continuous operation and sputtering by fast ions striking the cathode with an energy corresponding to the cathode fall during the glow-to-arc transition, when the fluorescent lamp operates as a cold-cathode discharge.

During continuous operation, the excess barium required at the cathode surface for thermionic emission is produced by chemical reactions between BaO and tungsten, liberating barium and leaving a layer of barium tungstate, Ba_3WO_4, between the wire and the coating (Waymouth, 1971). Barium diffuses through the emitter material to the cathode surface and the Ba_3WO_4 limits the Ba diffusion to that required to operate the lamp, thus avoiding rapid evaporation of Ba and the consequent shortening of the life of the lamp. Laser-induced fluorescence measurements by Bhattacharya (1989a, 1989b) showed that significantly more Ba neutral atoms were present in the vicinity of the electrode in the anode phase than in the cathode phase, since much of the barium leaving the cathode was ionized in the cathode fall and returned to the electrode. The consumption of barium was found to increase linearly with magnitude of the discharge current and also varied with the shape of the current supplied by the ballast.

Experiments and modeling of cathodes during the ignition phase of compact fluorescent lamps on electronic ballasts (Haverlag *et al.*, 2002) showed that sputtering could occur at the exposed tungsten areas of the electrode. The tungsten can be transported to emitter-coated areas of the cathode, reducing the work function, as well as eroding the electrode itself to the point of breaking and lamp failure.

2. Phosphors

UV radiation reaching the walls of the discharge tube is absorbed and converted to visible light by coatings of luminescent phosphor powders applied to them. These phosphors are composed of inorganic crystalline materials (typically oxides), which are optically transparent in the pure state but synthesized to incorporate specific luminescent centers to absorb the desired wavelengths of UV light and emit visible light. Such luminescent centers are typically strongly coupled to ligand fields of the solid; therefore, excitation by a UV photon creates electronically excited-state complexes in high-vibrational-energy states. Interaction with lattice phonons relaxes states of the excited manifold to lower vibrational energy levels before radiating. Due to the loss of energy by phonon relaxation, the energy of the emitted photon is much less than that of the absorbed one (a 254-nm UV

photon carries 4.89 eV, whereas a visible green photon carries only 2.2 eV). The difference between the energy of the absorbed photon and that of the emitted photon (called the Stokes shift) ends up as heat in the phosphor medium.

Phosphors that glowed in UV-generating rare-gas discharges were first described by Becquerel (1867) and phosphor development has been an active area of research since the first experimental fluorescent lamps were made in 1934. The discovery in 1942 of calcium halophosphate phosphors (McKeag and Ranby, 1942), which combined two complementary emission bands in a single phosphor, was a major breakthrough, and these phosphors are still used in fluorescent lamps, since they are relatively inexpensive and provide CRI in the range 51–76.

The discovery of rare-earth phosphors in the mid-70s, with narrow emission bands at 610 nm in the red, 545 nm in the green, and 450 nm in the blue (Verstegen, 1974; Verstegen *et al.*, 1974) led to the development of three-band phosphors with CRI of 80–85. More recently, multiband phosphors have been developed with CRI of 90 and above, but with lower efficacies than the three-band phosphors. Fluorescent lamps are available in a range of white colors with CCT from 3000 to 6500 K. For a detailed discussion of lamps phosphors, see Soules (1997).

Fluorescent phosphors deteriorate in operation as a result of photolytic decomposition and color-center formation, ion bombardment, and chemical reactions with mercury, glass, and impurity gases. The rate of deterioration increases with the wall loading (i.e., the flux density of UV photons and ions) and with wall temperature, depending on the particular type of phosphor. Sputtering of electrode material from the cathodes during starting also coats the phosphor near the electrodes. If the baking temperature during manufacture is too high, reactions with alkali from the glass can also damage the phosphor.

The effective life of a fluorescent lamp is the time over which it produces sufficient light for the application required. Standard cool-white halophosphate fluorescent lamps lose ~20% of their output over 8000 h of operation compared to ~10% for three-band phosphors. Loss of phosphor performance is referred to as *lumen depreciation*.

3. Amalgams

Mercury vapor pressure is an important parameter in the design of fluorescent lamps. Optimum luminous efficacy in linear fluorescent lamps is obtained for Hg vapor pressures around 7 mtorr, corresponding to a cold-spot temperature of 42 °C, while in compact fluorescent lamps the optimum value is somewhat higher (around 12 mtorr, with a cold spot of 50 °C). This is a serious restriction on the design of fluorescent lamps, which must produce satisfactory light output in ambient temperatures from below zero to 40 °C and with lamp operating temperatures that can reach 150 °C. Since the early 1970s, lighting companies have investigated the possibility of using amalgams of Hg with other metals to provide a more consistent vapor pressure over a wide temperature range (Franck, 1971; Bloem *et al.*, 1978). Most new compact fluorescent lamps contain an amalgam of either Bi-In-Hg or Bi-Pb-Sn-Hg, which have optimal Hg vapor pressures in the range 60–130 °C (Lankhorst and Niemann, 2000). Lankhorst and Niemann investigated the thermodynamic limitations of amalgams for use in fluorescent lamps, the most important property being the eutectic temperature of the alloy without mercury. Practical considerations are also important, since many of the efficient amalgams contain toxic substances such as Cd and Se. Lankhorst *et al.* (2000) showed that vapor pressure variations in the range 60–130 °C could be markedly reduced by using an amalgam of Bi-Pb-Au-Hg, and a number of other systems are currently under investigation.

G. Fluorescent lamp research and development

Research and development in fluorescent lamp technology is focused on four areas: more efficient fluorescent lamps; improved phosphors; reduction of mercury to comply with evolving environmental legislation; and compact fluorescent lamps to replace incandescent lamps.

The first of these areas involves a range of activities from studies of changes of diameter, fill-gas mixture, pressure, and phosphor type, to fundamental studies aimed at increasing the primary efficiency of generation of resonance radiation.

The primary focus in fluorescent lamp phosphor development is the search for less expensive substitutes for rare-earth phosphors without loss of efficiency, color, or durability. A longer-range goal is the development of phosphors that emit more than one visible photon for each incident UV photon.

Mercury is absorbed in phosphor and is consumed by chemical reactions with the emitted electrode materials of fluorescent lamps. Important research activities are continuing to minimize these processes and thus reduce the mercury content. Considerable progress has been made in this area; in 1980, standard fluorescent lamps contained up to 50 mg of mercury, while today, "ecological" lamps contain only 8 mg or less. During operation, ~50 μg is in the vapor phase; thus even smaller doses are possible if Hg loss mechanisms can be further reduced.

The development of more robust electrodes or more durable electron-emitting materials could yield significant improvements in fluorescent lamps, since it would allow them to operate at lower gas pressures, where efficacy is higher. Electrodeless lamps operate at lower pressures, with lamp life limited only by the electronics and the phosphor.

VII. HIGH-INTENSITY DISCHARGE LAMPS

A. Introduction

High-intensity discharge (HID) lamps are compact gas discharges (1–100 mm or more in length) that operate at pressures of order 1 atm or greater. The radiating temperatures in these lamps are much higher than in any incandescent solid, resulting in a much higher ratio of visible to IR radiation. Consequently, HID lamps are much brighter (higher radiance) and three to ten times more efficient than incandescent lamps. These "thermal plasma" discharges are close to local thermal equilibrium (LTE) since all species in the discharge (atoms, molecules, ions, and electrons) have approximately the same temperature (1000–7000 K). Collisional excitation/deexcitation rates are large compared to radiative decay rates, and collisional ionization is balanced locally by recombination in these LTE discharges. However, the radiation field is not in equilibrium with the particles.

There are three principal types of HID lamp, distinguished by their radiating species: high-pressure mercury (Kirby, 1997b); high-pressure sodium (HPS; de Groot and van Vliet, 1986; Hollo, 1997) and metal halide (MH; Preston and Odell, 1997). Figures 21(a) and (b) illustrate the principal components of typical MH and HPS lamps, respectively. Each consists of an inner discharge tube (arc tube) containing the high-pressure gas or vapor enclosed in a hermetically sealed outer envelope (jacket). The outer jacket protects the arc tube seals from oxidation and absorbs UV radiation emitted from the arc.

HID lamps are filled at room temperature with 35–300 torr of inert gas to aid in starting (this is typically argon, but mixtures of argon with krypton or pure xenon are also used in commercially available lamps). Most conventional HID lamps contain mercury, which is introduced in MH lamps as a droplet and vaporized to above atmospheric pressure by the heated wall during operation. An amalgam of mercury metal with sodium is used in HPS lamps. Other metals in MH lamps are introduced in the form of metal iodide salts, which melt at the wall, providing the required vapor above the molten salt, subsequently dissociating into their elemental constituents in the high-temperature region near the axis of the discharge. The entire dose of liquid Hg is evaporated at operating temperature and thus the Hg vapor is described as unsaturated. Vapor pressures of other additives (as well as the amalgam in HPS lamps) are typically saturated.

Arc tubes for mercury and MH lamps have traditionally been made of fused silica (commonly referred to as quartz), while HPS arc tubes are made from translucent polycrystalline aluminum, a ceramic material able to withstand corrosion by hot molten and gaseous sodium. Polycrystalline aluminum is gradually replacing quartz in MH lamps, due to its high chemical resistance and ability to operate at higher temperatures ($\sim$1400 K, compared to $\sim$1200 K for quartz).

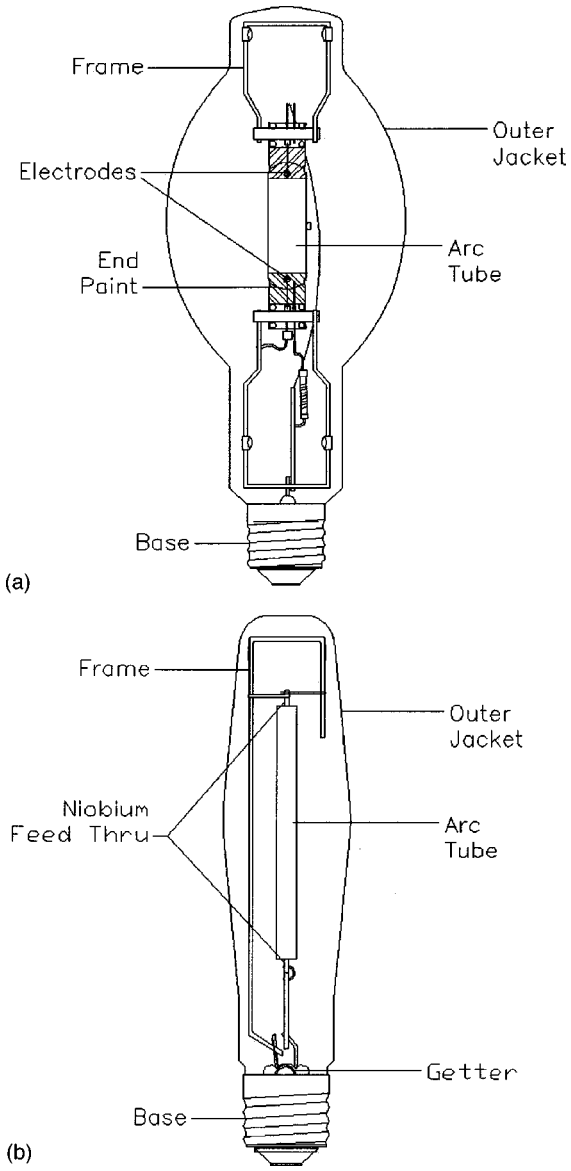

FIG. 21. Schematic diagram showing principal features of (a) 400-W MH lamp, (b) 400-W HPS lamp.

Although a number of electrodeless fluorescent lamps have appeared on the market (see Sec. VI.C), technological problems associated with the development of electrodeless HID lamps have proved more challenging. The ability to use this technology with chemical doses that would react with electrodes would be a great benefit to MH lamp development. To date only one product has been produced commercially for general lighting, the *Solar 1000*® lamp developed by Fusion Lighting (see Sec. VII.C).

B. Physics of the discharge

1. Energy balance

Electric power is dissipated in the arc tube by radiation from the atomic and molecular species in the discharge, heat conduction to the tube walls, and heating of the electrodes to the temperature required for therm-

TABLE I. Approximate percentages of power dissipation in 400-W HID lamps.

Lamp	Electrode loss	Heat conduction plus wall absorption	Radiation		
			IR	UV	Visible
Mercury	12	38	10	24	16
Metal halide	12	25	17	19	21
High-pressure sodium	6	38	25	0	31

ionic emission. Table I (Lister and Waymouth, 2001) shows the approximate percentages of power dissipation in these modes for 400-W mercury, HPS, and MH lamps. It is important to distinguish between near-IR gas-phase emission and mid-IR arc tube emission. Studies to distinguish these two channels in MH lamps are currently underway.

Electrode loss can be reduced by operating the lamp at low current, implying a higher operating voltage for a given input power. Thermal losses as a fraction of input power can be minimized by reducing the arc length, since power per unit length dissipated in the arc by heat conduction is approximately constant. The high arc resistance required in HID lamps to maintain a high voltage across a short arc gap is achieved by selecting a buffer gas of low electrical conductivity. Mercury vapor at high pressure (1–10 atm) is used in most commercially available HPS and MH lamps because, for the same gas temperature, it has a lower electrical conductivity than most credible alternatives, as well as a very low thermal conductivity, minimizing thermal losses. Investigations by Born (2001) suggest that replacement of mercury by zinc might require a lamp with a 25% longer electrode gap and a slight ($\sim 7\%$) reduction in efficacy.

In HID lamps, the gas temperature on axis is between 4000 and 7000 K, while the walls must be maintained at 1000–1400 K (depending on lamp type) to prevent deterioration of the arc tube material. The gas is heated principally by collisions between electrons and atoms, confining the main heating channel to the axis region. The temperature profile is itself modified by the radiation transport, since radiation emitted at one point may be absorbed at another point, resulting in a net transfer of energy.

Thermal gradients may cause free or gravitationally driven convective cells in HID lamps. Flow velocities are generally small (a few cm s^{-1}), and the flow is laminar. For sufficiently high pressure, however, flow may become turbulent (Elenbaas, 1951), leading to instability and flickering light output. The balance between convection and thermal conduction near the wall of the arc tube determines the variation of surface temperature. The vapor pressure of the molten salts used to enrich the spectrum is governed by the temperature of the cold spot, while the maximum temperature on the wall must be sufficiently low to prevent degradation of the wall material, so a reasonably uniform wall temperature is desirable. Convective flows can be reduced by reducing the tube radius. The aspect ratio (the ratio between tube length and diameter) is an important lamp design parameter (Elenbaas, 1951).

Metal halide lamp performance is significantly influenced by orientation during operation. The combination of diffusion and free convection in vertically burning MH lamps leads to chemical separation (referred to as demixing) with a concentration of more easily ionized metallic species near the lower electrode.

The arc in horizontally operated lamps bows upwards, due to buoyancy forces resulting from the balance of convective flows and gravitational forces. This bowing, which gives the arc its name, results in higher temperatures at the top of the arc tube (Waymouth, 1971) and is remedied in some lamps by curving the arc tube to follow the bowing (Koury *et al.*, 1975). Bowing also causes difficulties in design of optical systems for some lamps. The arc can be straightened by applying a correcting magnetic field, by rotating the lamp about its axis (Elenbaas, 1951), or by operation at high frequencies.

HID lamps operating above 1 kHz on electronic ballasts can have unstable arc/operating modes due to the excitation of acoustic resonances within the arc tube. Problematic acoustic resonances occur when high-frequency components of the lamp power (e.g., from internal switching-mode frequencies) couple with the natural sound-wave resonances of the arc tube cavity to produce standing pressure waves, which can rapidly destabilize the arc. At sufficiently high frequency (>350 kHz) these instabilities are damped and stable operation of the lamp is possible.

One approach for avoiding acoustic resonances is to switch the frequency before sufficient energy is imparted to the acoustic resonance (frequency hopping). However, frequencies at which acoustic resonances occur are sensitive to the operating conditions of the lamps, and in practice it is difficult to find a sufficiently broad band that will operate all lamps intended for the ballast.

A common solution is to apply a low-frequency (<400 Hz) square-wave voltage and current to the arc, such that the total power dissipated in the lamp is approximately constant with time, minimizing the potential to excite destabilizing acoustic resonances. Low-frequency excitation is usually below the cutoff frequency (or the lamp's lowest eigenfrequency).

The interaction of driving wave forms and the plasma to produce acoustical excitations is not always detrimental. Controlled excitation of acoustic resonances in a perturbative manner can be used to straighten bowed arcs and counteract the demixing and color separation effects caused by radial and axial segregation. The advent of electronic ballasts, which often incorporate microprocessor-controlled programmable wave forms, makes control of power delivered to the beneficial sys-

tem eigenmodes much simpler. Excitation at moderate levels with either fixed frequency or swept frequency can be achieved and sustained indefinitely with no arc extinguishment or lamp failure.

2. Radiation

The principal visible emitters in HID lamps are mercury atoms in mercury lamps, sodium atoms in HPS lamps, and metal atoms in MH lamps. Although mercury is the principal component of the vapor in most HPS and MH lamps, the arc temperatures are such that radiation from additive metal atoms (sodium or dissociated metal iodide molecules) dominates emission from visible mercury lines.

In MH lamps, the metal iodides participate in a halogen cycle: iodide molecules vaporize at the tube wall and diffuse to the high-temperature core of the arc, where they dissociate, freeing metal atoms. Free metal and iodine atoms diffuse, or are convected, back into the low-temperature mantle and chemically recombine, preventing metal atoms from interacting with the arc tube walls. The emitted radiation is dominated by the line spectrum of the added metal atoms and ions, with some contribution from metal iodide molecules (Wharmby, 1986). Arc temperatures at the core are too low to excite iodine significantly, and its emission lines are barely detectable.

In all three types of HID lamps, optical depths range from very thin to very thick, and the absorption spectra are greatly influenced by resonance, van der Waals, and Stark broadening. Because of the large temperature gradients, self-reversed lines are common. Spectral radiances at emission-line maxima approach 50% or more of the blackbody level at the arc axis temperature for strong nonresonance lines, and 25% or more of that level for resonance lines.

Figure 22 shows spectral power distributions of the radiation emitted from the three types of HID lamps. These spectra were taken on instruments with 0.6 nm spectral bandwidth and do not reveal the self-reversed nature of the spectral lines except in the case of the sodium resonance lines at 589 nm in the HPS lamp.

Infrared radiation is a significant loss mechanism in all HID lamps (see Table I), while there is substantial emission of UV radiation in mercury and MH lamps. A phosphor is used in some lamps to convert UV to visible light.

Mercury lamps for general lighting applications are almost obsolete, due to their poor CRI and efficacy. However, short-arc, ultrahigh-pressure mercury lamps operating at 150–300 atm generate an intense white-blue light, due to strong broadening of mercury spectral lines. The high luminance and small dimensions of these arcs provide sources (Derra *et al.*, 2001) suitable for various projection applications (e.g., video and data projection).

The sodium pressure in most HPS lamps (100 torr) is chosen to maximize radiation from the sodium-*D* (yellow) line, giving a high efficacy ($\sim$140 lm/W) but with a CRI $\sim$22. Increasing sodium pressure broadens the yellow lines to yellow-orange, where the eye is less sensitive, and some lamps produce "white" light with a CRI of 80 but an efficacy $\sim$50 lm/W. Pulsed excitation has also been used to achieve white light in HPS lamps.

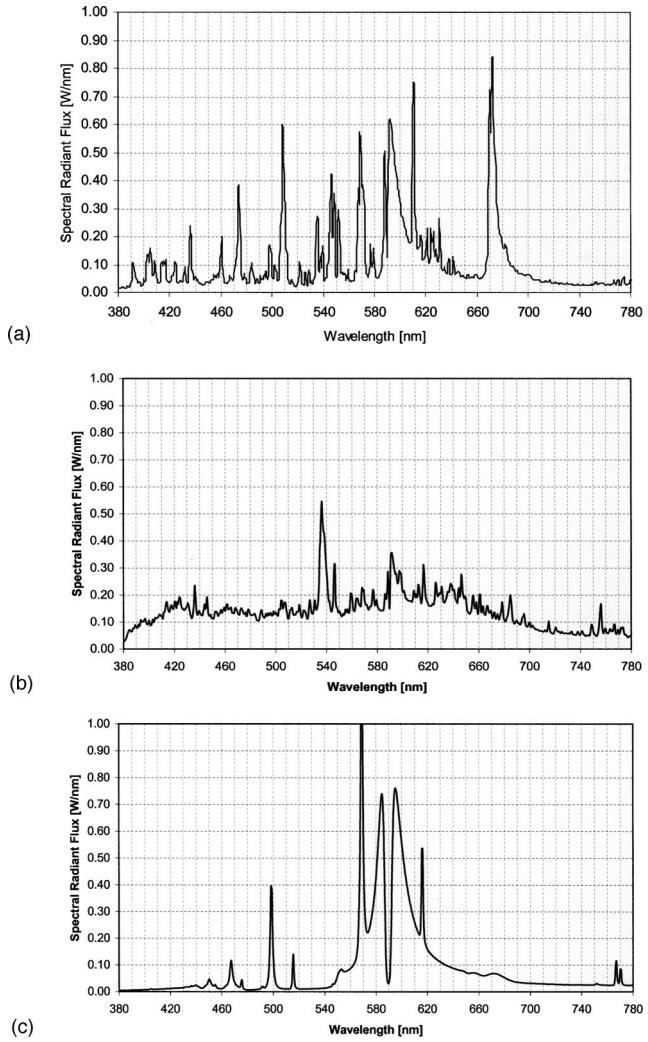

FIG. 22. Spectral distribution of radiated power ($W\,nm^{-1}$) of HID lamp types in use in the United States, all at 150 W input power: (a) quartz lamp with Na-Sc chemistry: the mercury lines are visible in the spectrum. The strong line at 590 nm is due to sodium, and the balance is due to groups of lines emitted by scandium atoms (unresolved at the spectrometer bandpass used here); (b) ceramic lamp with rare-earth chemistry; (c) high-pressure sodium lamp: all radiation is from sodium, the major yellow peak with a minimum at 590 being the self-reversed resonance line of sodium.

Metal atoms radiate in all colors, and MH lamps are produced with a high CRI and a variety of CCT by using a suitable mix of available metal halide salts. A blend of sodium and scandium iodides is widely used in the USA and Japan, while mixtures of indium (blue), thallium (green), and sodium iodides are popular in Europe. Mixtures including rare-earth iodides (e.g., dysprosium, holmium, thulium) are also used to improve CRI.

3. Electrodes

There has been considerable research into the physics of HID lamp electrodes in recent years, motivated by

the desire to increase lamp life and lumen maintenance. Much of this work has been published in a special issue of *Journal of Physics D: Applied Physics* (Vol. 35, No. 14), and many of these papers are referred to in this section and in the section on modeling of the electrode region (Sec. VII.D.2)

High-intensity discharge lamp cathodes operate in both diffuse and spot modes. These attachment modes have been studied in arcs since the early 1950s (Thouret *et al.*, 1951; Weizel and Thouret, 1952; Ecker, 1961). The transition of a thermionic cathode from diffuse to spot mode tends to occur in discharges at increased pressure or reduced current (Lichtenberg *et al.*, 2002). Larger electrodes also tend to favor the spot mode. The transition is characterized by a constriction of the arc attachment area to a radius of a few hundred μm. Hartmann *et al.* (2002) also found a highly contracted "superspot" mode, with a radius of 20–200 μm, apparently attached to small structures growing on the electrode at close to melting temperatures.

Experimental observations of arc attachment show a hysteresis in the mode transition as current is varied (Lichtenberg *et al.*, 2002; Pursch *et al.*, 2002). Attachment in a spot mode switches to a diffuse mode when the current is increased above a value I_{SD}. If the current is reduced from a value above I_{SD}, the transition from diffuse to spot mode occurs at a value $I_{DS}<I_{SD}$. There have been a number of theoretical attempts to explain this transition. These are discussed in Sec. VII.D.2. Lichtenberg *et al.* (2002) reported that bulk electrode temperature, power losses, and cathode-fall voltage in argon and xenon HID discharges at lower pressure remained approximately constant during the transition, but these quantities decreased as pressure was increased. At higher pressures in mercury lamps, Pursch *et al.* (2002) found that the transition from a diffuse to a spot mode was accompanied by a fall of about 10 V in discharge voltage, attributed to the higher temperature at the spot and therefore stronger thermionic emission in the spot mode.

The physics of the transition region between the cathode sheath and the arc, where the current channel expands from the area of the cathode tip or smaller to a quarter to one-half of the lamp cross section, is not well understood. There is considerable deviation from local thermal equilibrium in this region and the gas temperature in the vicinity of the cathode is much higher than in the center of the arc. Fromm *et al.* (2002) measured near-cathode temperatures of 6400 K in MH lamps (compared to 5600 K in the arc). Comparative temperatures in mercury were measured (Kettlitz and Großjohann, 2002) to be 11 000 and 7000 K, respectively. Convection and cataphoresis play a role in the plasma-electrode interface, although cataphoresis effects can be suppressed by operating the lamp above 100 Hz (Fromm *et al.*, 2002). Models of this region are discussed in Sec. VII.D.2.c.

The physics of the anode region in HID lamps is also poorly understood. Sanders and Pfender (1984) investigated atmospheric discharges in argon and concluded that there was a transition region between the arc and the anode fall, as is the case at the cathode. While the space-charge sheath created a positive anode fall, the total voltage across the region was negative. The ion production in the transition region was found to depend on macroscopic flow effects as well as axial diffusion and energy-loss processes from the arc plasma to the anode.

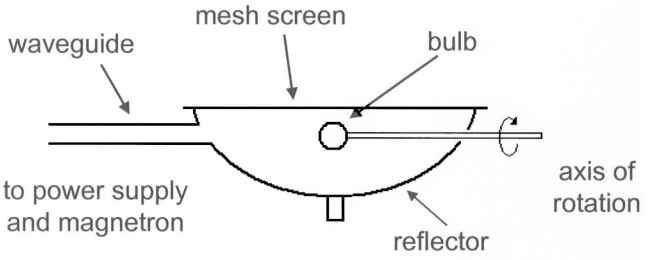

FIG. 23. Schematic of the *Solar 1000*® lamp.

4. Role of impurities

In all three classes of HID lamps, gaseous impurities can interfere with ignition or reignition. Both hydrogen and oxygen, liberated from absorbed water vapor, react with metal additives and with arc tube material. Hydrogen is especially harmful in MH lamps because it reacts with liberated iodine, forming HI. During lamp life, complex sequences of chemical reactions occur, which separate iodine from the active metals. Much of the liberated iodine forms mercuric iodides, and some will combine with residual H. The metal reacts with the arc tube walls and is lost to the halogen cycle, often causing a decrease in light output of the lamp over time. HI is an electronegative gas at room temperature and retards the electron avalanche growth during ignition by capturing free electrons. Avalanche can also be impeded by the presence of nitrogen gas, since low-energy electrons collide inelastically with N_2 molecules and transfer energy to molecular vibrational and rotational modes.

C. Electrodeless HID lamps

1. Resonant-cavity lamps

A number of resonant-cavity configurations for lighting applications were reviewed by Waymouth (1993), and there is a large patent literature on the subject, much of which is cited in that paper. The only commercial product to date for general lighting was the *Solar 1000*® (Wharmby, 1993, 1997; Turner *et al.*, 1995), which produced light largely from sulfur. The lamp was operated by transmitting microwave power at 2.45 GHz from a magnetron through a waveguide to the lamp, which was contained in a resonant cavity (see Fig. 23).

The original lamp contained argon and a small amount of sulfur, providing a very "white" light, mainly from the sulfur molecules in a 5900-W lamp, with a wall power loading of 250 W cm^{-2} (DiChristina, 1995), which is a factor of 10 higher than conventional HID lamps. The excess heat was removed by rotating the lamp and

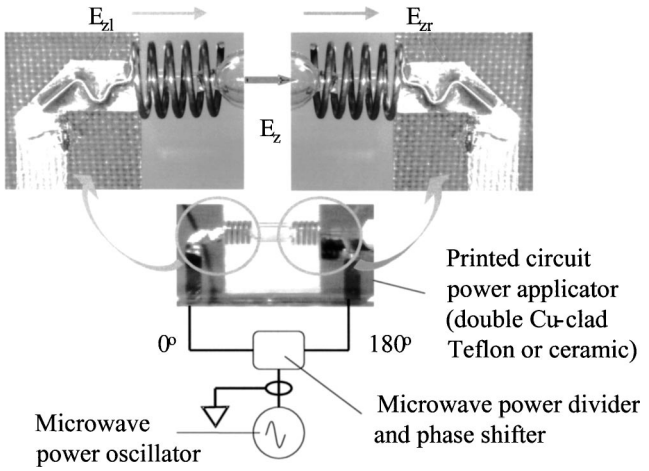

FIG. 24. An electrodeless HID lamp placed coaxially between the ends of facing quarter-wave helical resonators. The resonators have the same sense of rotation and are fed by a microwave source whose power is split so each resonator receives equal power. The wave is adjusted in phase so the feed points of each resonator are 180° out of phase. The axial electric-field components, E_{zl} and E_{zr}, add vectorially to produce an enhanced field E_z aligned with the axis of the arc lamp (see resonator detail in circled regions above). Microstripline is used to build the tuning network and power divider directly on the printed circuit applicator. The microstripline and resonator dimensions are determined by the driving frequency, 915 MHz, in the photo above.

by supplementary air cooling. The *Solar 1000*® was developed for general lighting applications and operated at 1425 W, with a bulb diameter of less than 3 cm. Due to the greatly reduced wall loading ($30\ \mathrm{W\,cm^{-2}}$), air cooling was not required, but the lamp still had to be rotated.

Sulfur molecules have a broad continuum of radiation in the visible spectrum with very little in either the IR or UV, and it is these molecules which were presumed to provide the major source of radiation (Johnston *et al.*, 2002). Since sulfur is chemically reactive with most metals, it cannot be used in conventional electroded lamps (Wharmby, 1993).

2. Capacitively coupled HID lamps

Lapatovich (1995) reported the development of microwave lamps in slow-wave structures of the type schematically illustrated in Fig. 24. A helical applicator is placed at each end of the lamp, such that the applied voltages are 180° out of phase, effectively doubling the axial electric field across the lamp. The coupling between applicator and lamp is essentially capacitive and can be efficient due to the high frequency (915 MHz and 2.45 GHz) employed. Lamps can operate at low power (35 W) and exhibit a flatter temperature profile than conventional electroded lamps, the power applied being significantly below that required for the skin effect to play a dominant role in these small (internal diameter $\sim$2 mm) discharges. The small size and correspondingly small heat capacity of this design is an advantage for faster starting (it reaches full operating temperature quickly) and restarting (it cools quickly to lower the Hg vapor pressure). Small electrodeless HID lamps are likely to find a number of applications when efficient, long-lived and low-cost solid-state microwave sources become available.

3. Inductively coupled HID lamps

Stewart *et al.* (1992) described an inductively coupled mercury-metal halide HID lamp, operating at 13.56 MHz with an induction coil surrounding a section of the outer jacket and a reflective coating to direct light away from the coil. Spectral emission measurements (Duffy *et al.*, 1992) show the characteristic hot annular core in the discharge [see Fig. 20(b)]. The lamp was never released commercially but had no electrode losses and produced 140 lm/W with very long life.

D. HID lamp modeling

1. Arc and thermal models

As we have seen, metal halide lamps are extremely complex systems, involving many tens of chemical species and many thousands of spectral lines. Uncertainties in the data for all relevant processes limit our ability to model these systems in detail. However, the great advances in both computer technology and diagnostic techniques in the last decade provide the opportunity to understand the influence of many important parameters (e.g., cold-spot temperature, arc tube design, and chemical constituents) on lamp performance.

Models are also necessary to interpret the results of experiments, which use such techniques as laser and x-ray spectroscopy. The aim is to develop a method for predicting how a lamp will perform after many thousands of hours, thus reducing the need for costly and time-consuming life tests. Models are also helpful in reducing the number of design experiments in optimizing lamp performance and establishing manufacturing tolerances.

The first theoretical models of high-pressure electric discharges in the 1960s emphasized arcs for which thermal conduction is the principal form of energy transport. The pioneering theoretical treatment of arcs in which radiation is the principal form of energy loss (radiation dominated arcs) by Lowke (1970) led to the first 1D time-dependent numerical model of a mercury arc (Lowke *et al.*, 1975).

Two-dimensional numerical models were developed by a number of lighting companies to address specific aspects of vertically burning HID lamps—arc constriction (Zollweg *et al.*, 1975), demixing and species separation (Fischer, 1976; Stormberg, 1981; Zollweg *et al.*, 1981; Dakin *et al.*, 1989), and radiation output (Stormberg, 1980; Zollweg *et al.*, 1981). Flesch and Neiger (2002) also included electrodes. Time-dependent 1D models of mercury discharges have been useful in understanding lamp electrical characteristics (Lowke *et al.*, 1975; Stormberg and Schäfer, 1983; Hartel *et al.*, 1999).

Numerical models of HID lamps are distinguished by the way the radiation term U_{rad} is calculated in the Elenbaas-Heller equation (5.6). Models that are primarily concerned with the thermal balance of the lamp often use an analytic form for U_{rad}, derived from experimental observations (Zollweg *et al.*, 1975; Chang *et al.*, 1990). Models have also been developed to predict radiation output in mercury (Stormberg and Schäfer, 1983; Hartel *et al.*, 1999) and MH lamps (Zollweg *et al.*, 1981; Dakin *et al.*, 1989) in which U_{rad} is calculated self-consistently from the radiation transport data for the most important lines.

There is an extensive literature describing theory and modeling of the electrode region in high-pressure arcs, much of which has been applied to HID lamps. Electrodes in HID lamps generally require a 3D representation, but if the area of current attachment to the cathode is large compared to the width of the electrode plasma-interaction region (as is the case in diffuse mode operation) a 1D model in the coordinate perpendicular to the cathode surface can provide valuable insight. Since these lamps operate on an ac ballast, time-dependent effects are also important.

Thermal models have been used to determine electrode temperatures and cathode fall voltages [Tielemans and Oostvogels, 1983 (dc); Springer and Lake, 1984 (ac)]. The transition region between the cathode sheath and the main discharge has also been included in a number of HID electrode thermal models [Waymouth, 1982; Schmitz and Riemann, 2001, 2002 (1D); Bötticher and Bötticher, 2000; Benilov and Cunha, 2002, 2003a (2D); Benilov and Cunha, 2003b (3D)].

A series of experiments on a model HID lamp (Dabringhausen *et al.*, 2002; Lichtenberg *et al.*, 2002; Luhmann *et al.*, 2002) has provided a consistent set of data for better understanding of HID electrode behavior and for validation of numerical models (Nandelstädt *et al.*, 2002). Experiments were performed in argon and xenon discharges, since the strength of visible radiation near the electrodes of regular HID lamps obscures some of the diagnostics. The lamp was made of fused silica with a 9 mm inside diameter and movable electrodes, enabling the arc length to be varied. Electrodes of pure tungsten and tungsten impregnated with thorium oxide were investigated. The models were able to reproduce many of the experimentally observed trends quite well, and the results are discussed in more detail in Sec. VII.D.2.c.

a. Fundamental data

Since the discharge is assumed to be in local thermal equilibrium, cross sections for inelastic processes involving electronic excitation of atoms and molecules are not required in HID lamp models. However, the electron momentum-transfer cross sections are required to calculate the electrical conductivity [Eq. (5.15)]. In most HID lamps, the dominant species for elastic collisions during steady-state operation is mercury, for which the cross sections from England and Elford (1991) are accepted as the most accurate (Hartel *et al.*, 1999; see Sec. VI.D.1.a).

The composition of the vapor in HID lamps as a function of gas temperature is calculated from the chemical potential of each species [see Eq. (7.1)]. Many data can be found in the JANAF tables (Stull and Prophet, 1971) or calculated using available molecular and atomic data based on procedures described therein. Thermodynamics data for rare-earth halides have been reviewed in a number of papers (Hilpert, 1989; Boghosian and Papatheodorou, 1996; Hilpert and Niemann, 1997). There are also commercially available databases, and most lighting companies have their own proprietary databases.

Parameters for the Lennard-Jones potential are necessary to calculate the transport properties (Sec. V.F), and a number are tabulated in Hirschfelder *et al.* (1954). In mercury-containing lamps, values for Hg are usually sufficient to calculate viscosity and thermal conductivity.

Although there are more than 10 000 known spectral lines emitted from MH lamps containing Dy (or other rare-earth metals with similarly complex spectra), most of those lines are optically thin. Under typical MH lamp operating conditions, the strong Hg lines and perhaps fewer than 100 additive lines are optically thick. Some knowledge of the broadening coefficients for the optically thick lines is needed.

Transition probabilities for the major spectral lines in many important atoms have been tabulated by Fuhr and Wiese (1998). Improved atomic transition probabilities for Hg (Benck *et al.*, 1989) and for metal atoms and ions from common metal halide additives including Sc (Lawler and Dakin, 1989), Tm (Wickliffe and Lawler, 1997), and Dy (Wickliffe *et al.*, 2000) make it easier to extract absolute information from emission spectroscopy measurements. Radiative lifetimes from laser-induced fluorescence measurements on atoms and ions in a beam environment have become available for elements of interest in lighting and many other neutral and singly ionized species. These lifetimes, when combined with modern branching-fraction measurements from Fourier-transform spectra of low-pressure lamps, have yielded vast improvements in the fundamental data needed to analyze and model discharges in low- and high-pressure lamps (Lawler, 1987).

b. Electrical characteristics

Less attention has been given to modeling of the electrical characteristics of HID lamps than to fluorescent lamps, in which the positive column may be regarded as infinitely long. Such models as have been reported are mostly limited to 1D time-dependent treatments of mercury lamps. Lowke *et al.* (1975) included a simple circuit equation and were able to reproduce the experimentally measured current-voltage characteristics by adjusting the net radiation transport term U_{rad} in the thermal balance equation (5.6). Stormberg and Schäfer (1983) also used a circuit equation, but calculated U_{rad} self-consistently from the available radiation transport data for mercury.

Hartel *et al.* (1999) also calculated U_{rad} self-consistently, but included the measured electrical current and found better agreement in the electrical and

spectral characteristics by including the time-dependent variation in the cathode and anode falls measured by Kloss *et al.* (2000). Hashiguchi *et al.* (2002) recently reported results of a 1D time dependent model in an MH lamp with Na-Sc chemistry.

c. Local thermal equilibrium

In the central region of the arc, the electron and gas temperatures are approximately equal. This does not strictly apply in the mantle, but since temperatures are too low there to provide substantial excitation, the discharge is generally considered to be in local thermal equilibrium with the atoms, ions, and electrons conforming to a Maxwell-Boltzmann energy distribution. The distribution of the chemical components can be calculated from the thermodynamic properties of the constituents by minimizing the Gibbs free energy per unit volume (Dakin *et al.*, 1989) at each desired temperature T,

$$G=\sum_j n_j\chi_j=\text{minimum}, \tag{7.1}$$

where $n_j(T)$ and $\chi_j(T)$ are the density and chemical potential of the jth species, respectively. Algorithms for finding the Gibbs free-energy minimum in MH lamps are relatively complex (Cruise, 1964) because of the large number of species present, and there are a number of commercial software packages available to do this.

For a system in local thermal equilibrium, the number densities of upper- and lower-level atoms with excitation energies ε_u and ε_l, respectively, are related through a Boltzmann factor:

$$n_u=n_l\frac{g_u}{g_l}\exp[-(\varepsilon_u-\varepsilon_l)/k_BT]. \tag{7.2}$$

Ion and electron densities are related through the Saha equation,

$$\frac{n_j^+ n_e}{n_j}=\frac{2\sigma_j^+}{\sigma_j}\frac{(2\pi m_e k_B T)^{3/2}}{h^3}\exp\left(-\frac{\varepsilon_j^+-\Delta\varepsilon_j}{k_BT}\right), \tag{7.3}$$

where n_j and n_j^+ are the total (ground-state and excited) atom and ion densities, σ_j and σ_j^+ are the respective partition functions [$\sigma_j=\Sigma_k g_k^{(j)}\exp(-\varepsilon_k/k_BT)$] and ε_j^+ is the ionization potential for atoms in species j. Here $\Delta\varepsilon_j$ is a correction term to ε_j^+ due to the presence of plasma and is given by

$$\Delta\varepsilon_j=\frac{e^2}{4\pi\varepsilon_0\lambda_D}. \tag{7.4}$$

This correction is relatively small ($<10\%$) in most HID lamps.

The validity of the LTE assumption, even in the center of the arc, has recently been brought into question. Karabourniotis (2002) used emission spectroscopy to measure time-resolved excited-state densities in mercury HID lamps during a 50-Hz cycle and found significant deviations from Saha equilibrium, particularly for lower energy levels and at higher mercury pressures.

d. Particle diffusion

Particle diffusion, cataphoresis, and convection are responsible for mixing and demixing of the species. Solving the diffusion equations (5.1) and (5.2) directly is inconsistent with the LTE calculation of species densities, but Fischer (1976) developed a formalism for treating neutral-particle diffusion, which was extended by Stormberg (1981) to include ambipolar diffusion. The method outlined below is from Dakin *et al.* (1989). The density $n_j^{(el)}$ of element j in the gas is

$$n_j^{(el)}=\sum_k n_k\zeta_{kj}, \tag{7.5}$$

where ζ_{kj} are stochiometry coefficients for molecular species k. If the gases were well mixed then the elemental fractions $n_j^{(el)}/\Sigma_k n_k^{(el)}$ would be independent of gas temperature and position. However, in MH and HPS lamps, this is seldom the case, due to the combined effects of cataphoresis, diffusion, and convection. The elemental densities satisfy the continuity equation

$$\nabla\cdot n_j^{(el)}\vec{v}_j=\nabla\cdot\vec{v}_j\sum_k n_k\zeta_{kj}=0. \tag{7.6}$$

If there are N_s different species in the discharge, the diffusion velocities $\vec{v}_j$ of each species j satisfy a set of N_s-1 coupled equations (Hirschfelder *et al.*, 1954),

$$\sum_k\frac{n_j n_k}{N^2 D_{jk}}(\vec{v}_k-\vec{v}_j)=\nabla\frac{n_j}{N}+Z_j\frac{n_j}{n_e}\nabla\frac{n_e}{N}, \tag{7.7}$$

where D_{jk} is the diffusion coefficient of species j diffusing through species k [Eq. (5.20)] and the term containing Z_j, the ionic charge, represents charge particle (ambipolar) diffusion. Equations (7.7) are solved for all but the majority species in the gas (usually Hg) and it is assumed that

$$\sum_j\frac{n_j}{N}\vec{v}_j=\vec{v}, \tag{7.8}$$

where $\vec{v}$ is the fluid velocity found from Eq. (5.4).

Measurements and calculations of Tl segregation (demixing) in vertically burning MH lamps (Stormberg, 1981) clearly show the influence of ambipolar diffusion on the axial segregation. The concentration of Tl near the base of the lamp was found to be about a factor of 2 higher than in the center. If ambipolar diffusion is not included (Fischer, 1976), the calculated segregation is reduced by a factor of 2 and the results are in strong disagreement with experiment. The model results indicate a strong dependence of segregation on pressure and arc tube diameter. Segregation was found to have a maximum value for a particular value of lamp radius (6 mm in the case discussed by Stormberg). Dakin *et al.* (1989) also obtained good agreement with experiment in modeling segregation of Na and Sc in MH lamps, and Hashiguchi *et al.* (2002) have shown the axial segregation of Na and Sc in a time-dependent calculation.

e. Radiation transport

A self-consistent calculation of the spectral output of a HID lamp requires integration of Eq. (5.12) for rays

representing the complete spectrum of the lamp passing through each point in the discharge and over the complete solid angle.

The spectra from a mercury lamp now appears to be well understood, and models can predict the spectral output under a variety of conditions, due largely to the pioneering efforts of Stormberg (1980) to deduce broadening coefficients from experimental data and apply them in a 2D model. Stormberg also reproduced the spectra of important Na and Tl lines. Hartel *et al.* (1999) have shown the importance of time dependence in a 1D representation.

This method of analyzing the spectra of a HID lamp can also be used to calculate the radiation energy transport term U_{rad} (see Sec. VII.D.1.f below). Calculations of U_{rad} in HID lamps by solving the full radiation transport equations were shown to be possible in the early 1970s by using a relaxation method developed by Lowke (1969). The Hg, Na, Sc system has been extensively modeled for both steady-state (Zollweg *et al.*, 1981; Dakin *et al.*, 1989) and 50-Hz operation (Hashiguchi *et al.*, 2002).

The analysis of a MH lamp is computationally intensive, especially if the spectra of the rare-earth atoms are to be included. However, the problem is not hopeless, because all of the molecular emission and most of the atomic emission is optically thin under typical MH lamp conditions. The radiation transport problem in a high-pressure plasma is quite compatible with a multiprocessor approach, and the increased availability of both computer power and spectral data should make more complex treatments feasible.

Aubrecht and Lowke (1994) demonstrated the use of partial characteristics (Soloukhin, 1987) to solve the radiation transport problem in SF_6 discharges, and this method has also been successfully applied to mercury HID lamps (Sevast'yanenko, 1998). Using this method, the time-consuming integrations over radiation frequency are carried out in advance to calculate temperature-dependent integral functions, which are called *partial characteristics*. These partial characteristics are stored in the form of tables for use in the thermal equations to calculate radiation transfer.

f. Thermal balance

Models of the thermal balance in HID lamps differ in two important ways in their approach to solving the Elenbaas-Heller equation [Eqs. (5.5) and (5.6)]. The first is the choice of boundary condition on the gas temperature and the second is the way the radiation energy transport term U_{rad} is calculated. Early models assumed a constant temperature on the wall to calculate the thermal balance inside the lamp. A more realistic boundary condition is to equate the power dissipated as heat on the arc tube surface to that thermally radiated from the surface through the Stefan-Boltzmann law,

$$\vec{u} \cdot \kappa_g \nabla T_g = \varepsilon_m \sigma_B T_w^4, \tag{7.9}$$

where $\vec{u}$ is the unit vector normal to the surface, ε_m is the emissivity of the arc tube material, and σ_B is the Stefan-Boltzmann constant. Application of Eq. (7.9) enables the wall temperature to be calculated self-consistently as a function of position on the arc tube surface. In principle, this method could be used to calculate the temperature of the cold spot and determine the vapor composition of the molten salts from Eq. (7.1). Although models can predict trends in the wall temperature and define hot spots, they are not yet sufficiently accurate to calculate the cold-spot temperature, since a few degrees' error can make a large difference to the vapor pressure determination. Vapor composition at the cold spot is therefore calculated using the experimentally measured cold-spot temperature.

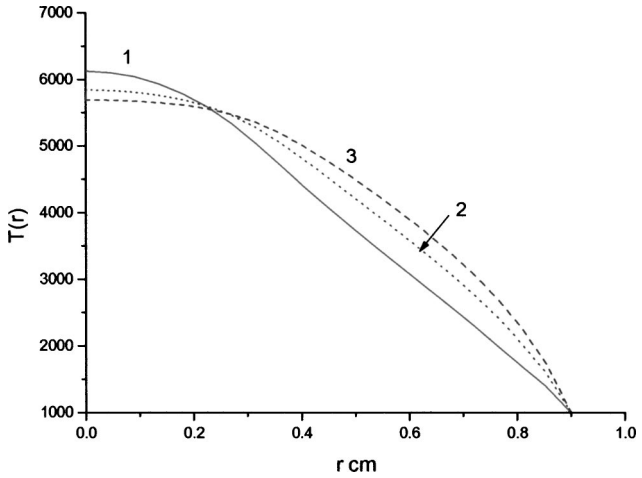

FIG. 25. Computed temperature profiles for a 2.7-atm Hg lamp with absorption terms $U_{abs}(T)=C_{abs}/T$ for (1) $C_{abs}=0$; (2) 9.6×10^7; and (3) 1.8×10^8 W m^{-3}, respectively. Adapted from Zollweg *et al.*, 1975.

Dakin *et al.* (1989) have used this approach in vertically burning lamps. Shyy and co-workers have developed 3D models to calculate the thermal properties of horizontally burning HID lamps (Chang *et al.*, 1990; Shyy and Chang, 1990), including the straightening of the arc using a magnetic field (Chang and Shyy, 1992) and the influence of the outer jacket on the thermal balance of the lamp system (Chang and Shyy, 1991). Shyy and Chang (1990) modeled a lamp bent in the shape of a bowed arc and showed uniform wall temperatures.

An alternative to solving the full radiation transport equations to calculate U_{rad} in Eq. (5.6) is to replace it by a simple function, $U_{rad}(T)=U_{emit}(T)-U_{abs}(T)$, representing the difference between emitted and absorbed radiation at temperature T in the lamp (Zollweg *et al.*, 1975; Chang *et al.*, 1990). In a pure mercury arc at 2.7 bars, Zollweg *et al.* found that the absorption of radiation could be represented by $U_{abs}(T)=C_{abs}/T$, where C_{abs} is an adjustable constant that can be fitted to the spectroscopic output of the lamp. Note that $U_{rad}(T)$ can become negative (i.e., is a net source of energy) in the colder mantle.

Figure 25 shows the result of a similar calculation, in which the computed temperature profile has been extended to the wall. Temperatures profiles are compared for $C_{abs}=0.0$, 9.6×10^7, and 1.8×10^8 W m^{-3} K, i.e., for

no absorption, absorption corresponding to the experimental measurements, and an artificially enhanced absorption, for constant total discharge power. As absorption increases, the axial temperature is substantially reduced, the profiles become broader, and radiation heating of the mantle is clearly demonstrated. The temperature profile computed using the value $C_{rad}=9.6\times10^7$ W m^{-3} K was shown to agree well with experimental measurements down to 4500 K, the lower limit of emission spectroscopy measurements.

Lowke (1970) showed that radiation transport of the optically thick lines can be included in the Elenbaas-Heller equation as an additional contribution to the thermal conductivity κ_{rad}, which is added to that of the gas κ_g in Eq. (5.5). This approach was used in a number of models (Fischer, 1987; Born, 1999, 2001) but is limited in its application to real lamps, since the optical depths of many of the important spectral lines are a substantial fraction of the discharge dimensions.

2. Modeling of the electrodes and near-electrode regions

a. Thermal models

The simplest models treat electrodes as metal cylinders, in which the current-emitting region is uniform and covers the entire electrode tip (diffuse mode). The cathode is heated by the bombardment of fast ions from the positive space-charge sheath and cooled by electrons losing energy in overcoming the work function ϕ, such that the total power delivered by the discharge to the cathode tip is

$$W_k=I\left(V_c-\frac{\phi}{e}+\frac{5k_BT_k}{2e}\right). \tag{7.10}$$

Since IV_c represents the total discharge power dissipated in the cathode sheath, Eq. (7.10) implies that all of this power (in the absence of radiative losses in the sheath) must be transferred to the cathode (Waymouth, 1982). Recent investigations have shown that this assumption does not hold for cathodes in the spot mode (Benilov and Cunha, 2002, 2003a) due to intensive enthalpy transport by the electron current from the sheath into the column, which is neglected in Eq. (7.10). However, it is unlikely to cause a large error in the diffuse mode.

The temperature profile along the electrode can be determined from the energy-balance equation

$$\pi R_k^2\frac{d}{dx}\kappa_k\frac{dT}{dx}-2\pi R_c\sigma_B\varepsilon_kT^4=0, \tag{7.11}$$

where κ_k and ε_k are the thermal conductivity and emissivity of the electrode material, respectively, and R_k is the electrode radius. Equation (7.11) expresses the condition that the net thermal energy flux through a section of the electrode is exactly balanced by the radiative energy flux at the electrode surface and ignores the heat exchange between the electrode and the filling gas by convection and conduction.

At the electrode tip, $T=T_k$ and the total net power input at the electrode tip from equations (7.10) and (7.11) is

$$W_k=\pi R_k^2\kappa_k\left(\frac{dT}{dx}\right)_k=I\left(V_c-\frac{\phi}{e}+\frac{5k_BT_k}{2e}\right). \tag{7.12}$$

The temperature profile in the electrode may be calculated from Eq. (7.11) by supplying any two boundary conditions, either the temperatures or the thermal flux, to the cathode tip and press seal. The cathode fall V_c is then calculated self-consistently from Eq. (7.12). Tielemans and Oostvogels (1983) used a similar model to describe electrode heating in steady-state HID lamps, while Springer and Lake (1984) included the frequency dependence of the discharge current.

Dabringhausen *et al.* (2002) measured the temperature profile along the length of both anode and cathode in a model lamp as a function of discharge current and rare-gas pressure, using a one-wavelength pyrometer that detects surface radiation in a spectral range from 0.7 to 1.1 μm. A second experiment (Luhmann *et al.*, 2002) used two specially designed Langmuir probes to measure the plasma potential along the discharge and deduce both the cathode and anode falls. Nandelstädt *et al.* (2002) showed that the cathode fall calculated from a thermal model, using the measured electrode temperatures, agreed well with the direct measurement of V_c, supporting the assumption that all the power from the cathode sheath is deposited at the electrode tip.

The electrons heat (or cool) the anode according to the sign of the anode fall V_a, and there is additional heating due to the energy released by the electrons to the anode, corresponding to the work function. Tielemans and Oostvogels (1983) suggested that the total power to the anode is

$$W_a=I\left(V_a+\frac{\phi}{e}\right) \tag{7.13}$$

although pyrometric measurements indicate that this is inaccurate in HID lamps (Lichtenberg, 2003). If $W_a>W_k$, the anode heating is greater than that to the cathode, and the anode temperature is higher than at the cathode.[1]

b. Cathode sheath models

Waymouth (1982) proposed a model to explain the existence of spot and diffuse modes. For a given value of the electrode tip temperature T_k, V_c can be obtained from the thermal model and from Eqs. (5.27) and (5.32),

$$j_e=\frac{\varepsilon_0}{4}\left(\frac{2e}{m_i}\right)^{1/2}\frac{E_k^2}{\beta V_c^{1/2}}. \tag{7.14}$$

[1]Modeling of the anode and near-anode region of HID lamps is currently an active area of research, but results have yet to appear in the open literature. There are many similarities to the modeling of high-pressure arcs (e.g., Amakawa *et al.*, 1998; Sansonnens *et al.*, 2000).

Equations (5.21) and (7.14) represent two equations in two variables, j_e and E_k. Waymouth analyzed a number of HID electrodes and found there were typically two solutions for j_e and E_k for each value of T_k up to a maximum value, beyond which no solutions could be found. He postulated that the low-current-density solution corresponded to the diffuse mode and the higher value to the spot mode. Typical upper values for j_e, calculated assuming $\beta = eV_c/\varepsilon_i$ [Eq. (5.33)] were $\sim 10^9$ A m^{-2}, i.e., the spot on an electrode carrying 10 A would have a diameter $\sim 200\ \mu$m, with a considerable component of the electron current supplied by field emission.

Benilov (1998) described the existence of diffuse and spot modes in terms of the nonmonotonic nature of the heat flux to the cathode as a function of electrode temperature. This occurs because the ion heating to the cathode reaches a maximum when the plasma at the edge of the sheath becomes fully ionized. Any further increase in the temperature of the attachment area increases the emission current, thereby cooling the electrode through electrons overcoming the work function, while the ion heating remains constant. Thus there exist two values of T_k for which the same power is delivered to the cathode. In order to correctly model this process, therefore, it is necessary to include a better physical representation of the plasma region adjacent to the space-charge sheath, sometimes referred to as the ionization layer.

Benilov (1998) used bifurcation theory to demonstrate the existence of multiple solutions in the framework of a 2D thermal model of the cathode coupled to the sheath equations. These solutions have also been calculated using an axially symmetric numerical model by Bötticher and Bötticher (2000). This model has been extended to include further axially symmetric (Benilov and Cunha, 2003a) and 3D (Benilov and Cunha, 2003b) modes. Solutions that were identified with the spot mode generally conformed with experimental observations (Lichtenberg *et al.*, 2002) concerning cathode shape and thermal properties (conduction and emissivity).

Benilov and Cunha (2003b) developed a method of calculating bifurcation points at which 3D spot-mode solutions branch off from solutions describing the diffuse mode and axially symmetric spot modes. In particular, the first bifurcation point positioned on the diffuse-mode solution has been calculated, as well as its stability limit, i.e., a current below which the diffuse mode becomes unstable. Parameter studies on cylindrical tungsten electrodes using the model predict that the stability limit is much more sensitive to variations of control parameters than characteristics of the diffuse mode, the strongest influences being the cathode dimensions and the work function of the cathode material. This conclusion is supported by the observation that the diffuse-spot transition is difficult to reproduce experimentally.

Modeling of collision-dominated sheaths in high-pressure arc discharges was addressed by Benilov and Coulombe (2001). They found that although ions can experience a number of collisions when passing through the space charge region, the calculated sheath width and cathode electric field are quite close to the values obtained using the collisionless model. For example, in a typical 150-W MH lamp (0.58 mm cathode diameter, 1.4 A, $\phi = 4$ eV) operating at 2900 K cathode temperature, the electric field at the cathode E_k is of order 10^4 V m^{-1}, corresponding to $E/p_0 \approx 50$ V m^{-1} torr^{-1}, where $p_0 = 273p/T$ torr is the reduced pressure. Kovar (1964) has noted that for mercury discharges, the high-field case [Eq. (5.30)] is applicable when $E/p_0 > 2$ V m^{-1} torr^{-1}. For these conditions, the ion charge exchange collision length is $\lambda_{cx} \approx 0.2\ \mu$m (Kovar, 1964), while the sheath width is $\delta_c \approx 1\ \mu$m. In this case, a typical ion experiences on average five collisions within the sheath. Clearly, these parameters will vary for different electrodes and different gas fills. For the case considered, the ratios of the sheath widths and cathode electric fields to those calculated using a collisionless (Langmuir-Childs) sheath are $\delta_c/\delta_c^{LC} \approx 1.05$ and $E_k/E_k^{LC} \approx 1.2$, so the results from the model are only weakly dependent on the sheath representation adopted.

Models of HID lamps including electrodes have been developed which ignore the cathode sheath entirely (Fischer, 1987; Flesch and Neiger, 2002). They introduced an enhanced non-LTE electrical conductivity in the near-cathode region, which reproduces the required cathode heating and current density at the cathode.

c. Transition region models

Waymouth (1982) suggested that the transition between the cathode sheath and the main discharge could be described by two separate regions:

(i) a *thermal gradient sheath* in which the current channel remains small, but the fraction of ions carried by the electric current at the sheath edge falls to a very small value, corresponding to the ratio of the ion and electron mobilities, while the gas temperature increases to a higher value than in the arc,
(ii) an *expansion zone* in which the current channel expands to the area of the main discharge.

Benilov (1998) proposed a three region model, characterized by three scale lengths: the Debye length λ_D (*space-charge sheath*); the ionization length λ_{IL} (*ionization layer*); and the length of energy relaxation λ_{TR} (*thermal relaxation zone*). Under typical high-pressure arc conditions, these lengths are quite distinct, $\lambda_D < 1\ \mu\text{m} \ll \lambda_{IL} \sim 10\ \mu\text{m} \ll \lambda_{TR} \sim 10^2\ \mu$m. The ionization layer is a quasineutral region of constant (but different) electron and gas temperatures, of thickness of order of the recombination length, and performs a similar function to the thermal gradient sheath in the Waymouth model.

Schmitz and Riemann (2002) also used a three-region model. The boundary conditions on the discharge side of the ionization layer were the temperatures of electrons and heavy particles in the arc plasma. They included a

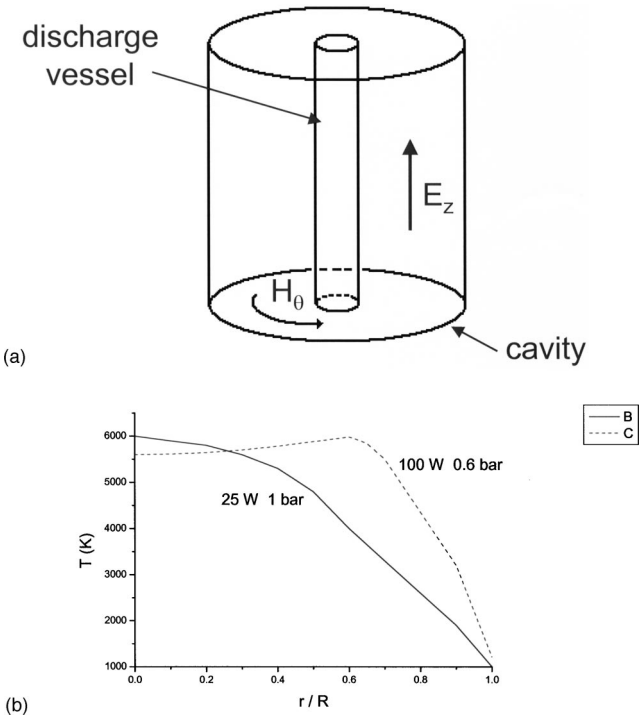

FIG. 26. Model resonant-cavity lamp: (a) schematic of lamp and electromagnetic fields; (b) temperature profile for two different microwave power and pressure conditions, ID $=10$ mm, $\nu=2.3$ GHz. Adapted from Offermans, 1990.

kinetic treatment of the presheath to obtain the ion current density j_i at the sheath edge and coupled the sheath model to a 1D thermal model at the cathode.

Nandelstädt *et al.* (2002) compared the results of a number of electrode models (Schmitz and Riemann, 2001, 2002; Benilov and Cunha, 2002; Bötticher and Bötticher, 2002; Flesch and Neiger, 2002) with experimental measurements. All the models reproduced the experimentally observed trends in cathode fall, but the Benilov model gave the best quantitative agreement, indicating the importance of the ionization layer in the calculations. Some differences were found in comparing the total power loss at the cathode with pyrometric measurements for large electrode diameters (1.5 mm), but in general the Benilov model reproduced the trends quite well.

3. Models of electrodeless HID lamps

The coupling of microwave power into a mercury lamp in a resonant cavity was studied theoretically and experimentally by Offermanns (1990). The system he considered is illustrated schematically in Fig. 26(a). In order to describe the system with a 1D model, he placed a lamp with large aspect ratio (length/diameter$\gg$1) inside a cylindrical resonant cavity and excited a symmetrical T_{010} mode, which has electromagnetic field components E_z, H_θ. For an axial electric field $E_z = E_0 \exp(i\omega t)$, Maxwell's equations reduce to

$$\frac{1}{r}\frac{d}{dr}\left[r\frac{d}{dr}(E_0)\right] - i\omega\mu_0\sigma_e(r)E_0 = 0. \tag{7.15}$$

Equations (3.1) and (7.15) may now be solved iteratively, together with the ideal-gas law, to calculate electric-field, density, and gas temperature profiles as a function of operating frequency, gas pressure, and discharge power. Detailed results from the model and comparison with experiment are given by Offermanns (1990). Temperature profiles obtained from a similar calculation are illustrated in Fig. 26(b). At low (25 W) power input to the discharge, temperature profiles are peaked at the center, while at high power (100 W), temperature profiles are peaked away from the axis and towards the wall.

These results were qualitatively observed in the experiment, although the measured temperatures on axis were somewhat lower (100–400 K) than the calculated values. The shift of the temperature maximum away from the discharge axis with increasing power is a common observation in microwave plasma devices and is a direct result of the skin effect discussed in Sec. V.H. At high powers, the electron density near the axis increases and the skin depth [Eq. (5.35)] becomes comparable to the dimensions of the discharge, effectively screening the central region from the external electromagnetic fields. Power input is thus limited to a value that does not result in damage to the containing vessel.

Waymouth (1993) presented results of numerical calculations relevant to the application of microwave power to the discharges studied by Zollweg *et al.* (1975) (see Sec. VIII.D.1). He found for this case that the calculated gas temperatures on axis were always lower than those found for dc operation, again due to the skin effect. This leads to a lower radiation efficiency for low discharge power. However, at higher powers, the heating of the gas away from the axis led to improved efficiency compared to dc discharges at the same power. Further, the presence of a temperature peak closer to the wall reduces radiation trapping for that portion of light emitted in the direction of the wall, further enhancing efficiency. Waymouth also concluded that in this case the microwave discharge has a positive electric field vs current characteristic, unlike the dc and 50-Hz operation of standard HID lamps.

Two-dimensional modeling of HID inductively coupled discharges (Duffy *et al.*, 1992) has shown the importance of $\vec{j}\times\vec{B}$ forces, which induce much higher convection velocities ($\sim 40\ \mathrm{cm\,s^{-1}}$) than in conventional lamps.

E. Lamp electrical circuit system

1. Lamp starting

Ballasts for HID lamps employ either a voltage step-up transformer, or a supplemental igniter circuit, to increase the ballast open-circuit voltage in order to properly start the lamp.

During the starting phase of HID lamps, mercury vapor pressure is only a few millitorr and any salts present remain solidified, so the initial discharge is formed in argon or xenon gas at a pressure of 35–300 torr. Argon

is used in mercury and MH lamps because discharges are easier to start than in xenon. Xenon is preferred in HPS lamps, since it provides higher efficacy during normal operation, due to its lower thermal conductivity and excimer (NaXe*) contribution to the spectral output. After striking, the discharge is essentially a low-pressure mercury cold-cathode glow. As the lamp warms up, the mercury dose and salts vaporize, the vapor pressure increases, and the arc constricts and localizes near the electrode tips (glow-to-arc transition). This transition time should be kept to a minimum, since sputtering of electrode material onto the arc tube during the glow phase can cause poor lumen maintenance.

High-intensity discharge lamps use a number of different starting aids. In mercury and older MH lamps, an auxiliary electrode (or probe) is placed a few millimeters from one of the main electrodes. When the supply is switched on, a glow discharge forms between the main electrode and the probe, and the low-current glow discharge provides sufficient ionization to initiate breakdown between the two main electrodes of the arc tube. After breakdown, the probe plays no role during run-up or steady-state lamp operation and must be effectively insulated to avoid electrolysis.

High-pressure sodium and newer metal halide lamps use 2–4.5-kV pulsed start circuits in place of the probe, which results in reduced sputtering from electrodes and also better lumen maintenance (see Sec. VII.F.2). Another aid to starting is UV irradiation of the discharge from a small capacitively coupled glow discharge lamp, located in the outer jacket. Some MH lamps use radioactive traces of ^{85}Kr mixed with the Ar buffer gas as a starting aid.

Full light output in HID lamps is only reached a few minutes after starting. If the lamp is switched off, the lamp must be allowed to cool until the vapor is sufficiently condensed to allow reignition at the applied starting voltage. For special applications, such as automobile headlights, where instant start and restart are required, special high ignition voltage ballasts are used.

2. Continuous operation

HID lamps must also be reignited each half-cycle; the peak instantaneous voltage required to accomplish this is typically 40% more than the instantaneous arc voltage during the majority of the half-cycle. A properly designed ballast will reignite the lamp at the start of each half-cycle without contribution to the voltage from the ballast's igniter circuitry.

High-frequency electronic ballasts are being introduced to reduce weight, volume, and audio noise and to improve maintenance, although these ballasts are substantially more expensive than magnetic ballasts. They also exacerbate the problems from excitation of acoustic resonances discussed in Sec. VII.A.1 above.

F. Lamp materials

1. Metal halide lamp dosing

Modern MH lamps contain multiple metal halide salts. The salts are added instead of pure metals because of their relatively high vapor pressure at lamp operating temperatures (about 1100–1300 K). Metal iodides are usually chosen as lamp salts since the dissociated halogen component is less reactive with the tungsten electrodes used to carry current into the plasma. Quartz MH lamps often contain mixtures of ScI_3, NaI, other minor additives, and metallic liquid mercury. Sometimes the lamps are dosed with a flake of Sc metal that acts as an internal getter of trace impurities. Ceramic metal halide lamps are often dosed with combinations of rare-earth iodides, such as DyI_3, TmI_3, HoI_3, CeI_3, or NdI_3, along with NaI, TlI, and sometimes an alkaline-earth iodide such as CaI_2. Occasionally, bromide salts are used in special lamps.

All of these compounds are extremely hydroscopic, with the rare-earth and scandium iodides being the most problematic. All handling of salts and lamp dosing must be done in a dry-box atmosphere of scrubbed argon gas and the moisture content of this gas must be monitored and maintained at less than a few ppm. The salts are generally provided as spherical pills, which are available commercially and formed from a melt mixture of definite stoichiometry. The spherical pills expedite automated manufacturing processes. Experimental lamps are often dosed with individual salt components provided as pills, granules, or flakes.

2. Arc tube materials and wall reactions

If it is necessary to raise the vapor pressure of the condensate, one or both ends of the arc tube may be coated with a refractory, oxide-based IR-absorbing end paint to increase wall temperatures. Thermal management of the arc tube can also be modified by surrounding it with a glass or quartz shroud, which also protects the outer jacket in the event of destructive failure.

Sodium loss can occur as a result of an electrolytic process at the arc tube wall in high-pressure sodium (Weinmüller, 1986) and MH lamps (Waymouth, 1971; Keeffe and Meyer, 1989). In operation, there are always a few parts per million of sodium ions dissolved in quartz in contact with sodium iodide, as a result of reaching thermochemical equilibrium in the reversible reaction between the quartz and the iodide. The quantity is not harmful to the quartz, nor does it represent a significant depletion of sodium from the initial lamp dose. However, sodium ions are mobile in quartz, and negative charging of the outer surface of the quartz arc tube by photoelectrons emitted from various parts of the outer jacket (under UV bombardment) will attract the sodium ions to the outer surface, to be neutralized and evaporated. The depletion of the ionic concentration in the inner surface then permits the forward reaction to proceed, providing more sodium ions, which are electrolyzed in turn, until eventually a substantial fraction of

the original sodium dose has been lost. Outer jacket designs providing minimum photoelectric-emitting surfaces, or positively biased surfaces (such as a shroud) are used to solve this problem.

Chemical reactions between quartz and metals and metal iodides in MH lamps may form stable metal oxides at the wall and liberate silicon (van Erk and Rietveld, 1986; Zubler, 1988). The loss of metal reduces the partial pressure of metal vapor and ultimately changes the radiation output of the lamp. The silicon metal reacts with iodine to form volatile silicon SiI_4, which decomposes at the electrode temperature and deposits silicon on the electrode (Waymouth, 1971). Silicon will dissolve in the tungsten, forming silicides which melt at the operating temperature, drastically distorting the electrode shape and degrading its performance. The iodine transported to the hot electrode reacts further with the ThO_2 dopant to form ThI_4. The liberation of ThI_4 from the tip is one of the life-limiting processes in MH lamps, adversely affecting the reignition process every half-cycle, to the point that the ballast can no longer reignite the lamp.

Fused-silica lamps are particularly sensitive to water, since dissolved hydroxyl is dissociated photolytically by UV radiation from the discharge, liberating hydrogen. The hydroxyl content in quartz must be at most a few parts per million. Moisture in the outer jacket must also be minimized, since it is also dissociated by UV light, and the liberated hydrogen diffuses rapidly through hot fused silica. Hydrocarbon vapors in the outer jacket are also decomposed thermally and photolytically, liberating hydrogen and depositing amorphous carbon on the arc tube wall surface, reducing optical transmission. A getter material is frequently used in the outer jacket to scrub the atmosphere of hydrogen and oxygen.

Efficacy of HID lamps increases as input electrical power per unit length is increased, first because of a reduction in the fraction of power lost to heat conduction, and second due to increased arc tube temperature, which results in higher vapor pressures of the radiating species. However, increased arc tube temperatures reduce lamp life due to increased chemical reactions with the arc tube material, and in the case of quartz, due to recrystallization of SiO_2 (devitrification). Acceptable lives in mercury lamps are obtained at wall loadings of 10–12 W/cm^2, and quartz MH lamps for general lighting are commonly found at 13–22 W/cm^2. The robustness of polycrystalline aluminum at higher temperatures allows ceramic MH lamps to run at $\sim$40 W/cm^2, and HPS lamps can use designs at 15–20 W/cm^2. For some applications, such as automobile headlamps and projection lamps, shorter lifetimes are acceptable and higher wall loading may be used.

3. Electrodes

Mercury and HPS lamp electrodes are coated with an electron-emitting activator material, which evaporates with time, resulting in failure to ignite or reignite each half-cycle. All HID lamp types are subject to excessive arc tube blackening by material evaporated from the electrode or sputtered by bombardment by ions accelerated in the space-charge sheath at the cathode.

In HPS lamps, wall blackening near the electrodes leads to an increase in the amalgam temperature and the subsequent increase in gas pressure causes a voltage rise. This can result in cycling near the end of lamp life, in which the lamp voltage rises to a value that can no longer be sustained by the ballast, and the lamp extinguishes. The lamp then cools to a temperature at which the igniter pulse is sufficient to restart the lamp and the process is repeated, resulting in a continuous switching cycle that repeats every few minutes. This problem can be solved by reducing the amalgam dose to the extent that all the mercury and sodium is in the vapor phase during normal lamp operation. This principle has led to the development of so-called "unsaturated vapor" HPS lamps. For these lamps, minimization of sodium loss due to chemical reactions with arc tube components is critical, since there is no pool of sodium available to replace it. Experiments and modeling by Almanstötter *et al.* (2002) suggest that the presence of a sodium monolayer on the cathode may reduce the work function of the electrode to a sufficient degree to allow operation at much lower electrode temperatures.

4. Lamp seals

Molybdenum foil seals in MH lamps have adequate life when protected from oxidation by a vacuum or an inert atmosphere in the outer jacket. The electrical lead-in in HPS lamps includes a niobium metal (also known as columbium) tubular member, chosen to match the coefficient of thermal expansion of polycrystalline aluminum and sealed with a polycrystalline oxide mixture, fusible without melting either niobium or polycrystalline aluminum. The niobium is protected from oxidation by a vacuum in the outer jacket. In HPS lamps, the maximum seal temperature is determined by the resistance of sealing compounds to attack by sodium, thereby limiting the cold-spot temperature and hence the maximum pressure of sodium vapor in the arc tube.

G. HID lamp research and development

1. New materials

The development of new materials will be central to advances in HID lamp technology in the future. New ceramics for arc tubes with properties better than polycrystalline aluminum (e.g., higher transparency, greater strength, improved corrosion resistance, or better thermal shock resistance) have been in the research phase for several years and in some cases are already under development.

New materials for electrodes that can better withstand the high-temperature chemical attack in the HID environment have been proposed, but are still in the research phase. At present, tungsten remains the preferred material. Advances have been made to make "green" or

environmentally friendly lamps by removing thorium oxide from the electrodes, and many of these lamps are on the market already.

2. Operation on electronic ballasts

The performance of MH lamps is enhanced under the operation of electronic ballasts—that is, smart, active electronic power supplies versus passive inductive ballasting. Among the benefits of electronic control are improved lumen maintenance and faster warmups and dimming. The chief impediment to their widespread introduction now is cost. Active research programs are exploring new topologies incorporating power MOSFET's and on-board microprocessors for wave-form control. As these ballasts become compact, lighter weight, and less costly, they will find applications in many more areas as new buildings are constructed and older structures refitted.

3. Molecular discharges

Over the past 25 years many chemical fills have been tested in HID lamps. Most of them depend on atomic emission from dissociated metal salts. A few, notably the sulfur lamp, are purely molecular. Other molecular systems studied suffer from the same technological barrier as sulfur, namely, electrode degradation. While electrodeless excitation is viable, high-frequency electronic drivers (at 750–2.45 GHz) do not have the efficiency, life, or interference-free operation required for general lighting applications. However, there are specific technological applications that could employ electrodeless HID lamps (e.g., video projection). Until materials for electrodes can be found that withstand the attack of sulfur or other molecules, this category of lamp will remain a curiosity. Coated electrodes, often discussed in the literature, may provide some resistance to attack, but no coating has been produced that is perfect with respect to pinholes and adhesion over life.

4. Mercury-free lamps

The use of mercury in HID lamps is almost universal, but there is some momentum for removing mercury from these devices entirely, which currently means compromising lamp life. A mercury-free HPS lamp is already on the market, and an automobile headlamp without mercury is imminent (Callahan *et al.*, 2002). Mercury-free MH lamps for general lighting are under development by all the major lighting manufacturers, and it is only a matter of time before this technology is introduced. The drivers for commercial introduction will be a demonstration of lamp performance equivalent to that of a mercury-containing lamp, or legislation mandating mercury removal.

5. Numerical modeling

Great advances have been made in analytical and numerical models that can be applied to the behavior of HID lamps. Models of convective gas flows, heat transfer, and environmental interaction provide valuable research and development insight as well as design tools for the engineers. Individual programs are currently used to predict behavior and shorten the design cycle time. Streamlining, refining, and linking of these codes to provide self-consistent predictive capability between thermal and electrical behavior, and radiative output from HID lamps will accelerate the introduction of improved products.

VIII. NON-LTE, MERCURY-FREE LAMPS

A. Low-pressure sodium lamps

The low-pressure sodium (LPS) lamp was introduced in the 1930s and is still the most efficient light source available. The physics and operation of LPS lamps are discussed in detail by Waymouth (1971) and Denneman (1981), and the current status of LPS lamp technology is reviewed by Kirby (1997a).

Low-pressure-sodium lamps emit radiation principally in two resonance lines, 589.0 and 589.6 nm (D lines), which are near the peak of the photopic eye sensitivity curve, corresponding to about 520 lm/W. In fluorescent lamps, the conversion efficiency of 254-nm radiation to visible light using current phosphors is about 160 lm/W, so an LPS lamp with the same energy efficiency in converting electrical power to resonance radiation as a fluorescent lamp would have more than three times the efficacy, i.e., about 300 lm/W (Waymouth, 1971). In the 1930s, LPS lamps achieved 50 lm/W, but significant improvements since that time have led to efficacies as high as 200 lm/W (Kirby, 1997a). However, the radiation produced is principally yellow, which gives very poor color rendition, and the use of these lamps is mainly restricted to outdoor applications, such as highways and parking areas, where brightness is more important than color definition.

LPS lamps contain a minority of sodium vapor in a buffer gas, which is typically neon. The optimum vapor pressure of sodium in these lamps is 3 mtorr, which is attained at a temperature of 260 °C (corresponding to a Na atom density of 1.5×10^{20} m^{-3} at the wall). Below the optimum temperature there is insufficient vapor to provide radiation, and above this temperature, increased radiation trapping causes loss of efficacy.

In order to maintain the lamp at the required temperature, additional means of heating are necessary. In early LPS lamps, this was achieved using a neon buffer gas at a pressure of 20 torr, to provide gas heating by elastic scattering from electrons, and by enclosing the arc tube in a vacuum-sealed outer jacket to reduce losses due to convection (Waymouth, 1971). In the current generation of LPS lamps, a coating on the inside of the outer jacket, which reflects IR radiation back to the arc tube, reduces the heat losses still further, enabling the lamps to operate with neon pressures below 10 torr.

The current densities required to provide the necessary gas heating are much higher than in a standard fluorescent lamp, resulting in higher electron densities and

consequently increased sodium depletion on axis. Druyvesteyn (1934) was the first to observe sodium depletion at the center of the discharge, finding that for his conditions 83% of sodium atoms were ionized in this region. This finding was part of the first detailed experimental investigation of LPS lamps, in which Druyvesteyn used Langmuir probes to measure the electron temperature and absorption spectroscopy to measure the relative densities of excited sodium atoms and sodium ions. Extensive numerical and experimental investigations of low-pressure Cs and Na rare-gas discharges were conducted by van Tongeren (1975), who found good qualitative agreement despite the relatively simple three-level atomic model adopted. Later calculations by Vriens (1978), which included multistep ionization processes, led to better agreement with experiment, particularly for the electric field.

The main difficulty in attaining the theoretical efficacy limit of the LPS is to achieve both the optimum current density and the optimum wall temperature simultaneously (Waymouth, 1971). The discharge power may be increased at constant current by raising the discharge electric field or lengthening the lamp. The latter solution has the further advantage, in common with the fluorescent lamp, of reducing the fraction of input power which is lost due to the electrodes. There are two types of LPS lamp—the standard SOX lamp and the SOX-E, which is run at lower current (Kirby, 1997a). The discharge in SOX lamps is lengthened by bending the tube into a U shape (Waymouth, 1971; Kirby, 1997a). In a 90-W SOX lamp, 30% of input power is output as visible radiation, 5% as IR radiation, 22% of losses are due to electrodes, and the remaining 43% is accounted for by other losses, such as gas heating.

Increasing the lamp power by increasing the discharge current leads to increased sodium depletion on axis due to radial cataphoresis. Conventional LPS lamps operate on a 50/60-Hz ac ballast. The effect of sodium depletion can be reduced by use of a square-wave ballast, to reduce the peak value of the current, but this has limitations due to the control gear requirements.

A monotonic increase in efficacy of 10–20 % has been reported as the operating frequency is increased from 100 to 400 MHz (de Groot *et al.*, 1984). This is well above the frequency associated with sodium ion diffusion (1 kHz) and of order of the trapped decay rate of excited sodium atoms (100 kHz) in a typical LPS discharge. In contrast to fluorescent lamps, operation from 1 to 100 kHz can lead to a reduction in efficacy compared to 50/60-Hz operation.

A further problem affecting the efficacy of LPS lamps is radiation transport. Radiation trapping of the sodium *D* lines is more effective than trapping of the 254-nm line in mercury discharges, while the ground-level sodium atoms are depleted near the axis, so most of the radiation from the lamp is emitted near the surface. In a U-shaped lamp, some of the radiation emitted in one leg may be trapped in the other (Kirby, 1997a). Changes in the shape of the lamp, to replace the circular cross section with one that has an increased ratio of surface area to volume (such as a cross or crescent shape; Waymouth, 1971) have proved successful in increasing the efficacy of these lamps.

During the starting phase before the lamp has heated sufficiently to vaporize the sodium, the discharge is essentially a rare-gas plasma. This phase lasts typically 10–15 min. A small amount (0.5–1 %) of argon is added to the neon, forming a so-called Penning mixture (Penning, 1928) to reduce the starting voltage. Penning ionization occurs when ground-state argon atoms collide with neon metastable atoms to produce argon ions. During the long starting phase, however, argon ions diffuse to the wall and may become embedded in the glass arc tube, leading to the removal of argon from the gas mixture and a rise in starting voltage. The glass used in LPS lamps must therefore be both nonabsorbing for argon and resistive to chemical interaction with sodium.

B. Rare-gas discharges for lighting

Low-pressure discharges in rare gases have not been used for general lighting. The most readily excited radiation spectrum is in the vacuum ultraviolet, where the phosphor conversion to visible light is inefficient. Furthermore, the vuv radiation tends to degrade phosphors more rapidly than UV radiation. Rare-gas discharges have been used in special light sources such as street signs, copy machine lamps, and plasma displays (Murakami, 1995). These discharges have the advantage that their performance is independent of the ambient temperature, unlike fluorescent and LPS lamps, and they are therefore suited to outdoor applications in cold climates. The efficacy of these discharges would be greatly improved if phosphors could be developed with quantum conversion efficiencies to visible light which are substantially greater than 1 for vuv photons. As is the case for fluorescent lamps, such "quantum splitting" phosphors are an important research goal.

Rare gases such as neon, argon, krypton, and xenon have a similar energy level structure. Therefore the elementary processes in the discharge plasma of these gases are identical and may be described in a similar way. The important low excited levels in neon are in the $2p^5 3s$ configuration, called $1s$ by Paschen (four levels), and the $2p^5 3p$ configuration, called $2p$ by Paschen (ten levels). Resonance radiation from two of the $1s$ levels is in the vuv, while visible radiation and near-IR is emitted from the decay of the $2p$ to the $1s$ levels. The principal visible lines due to the $2p$ to $1s$ in neon are red, and in argon are near-IR. The yellow emission from krypton and the blue emission from xenon are from transitions between higher excited levels.

Neon discharges are the most efficient of all rare gases in producing visible light, and the bright red neon line is used as the center high-mounted stop light (brake light) on some automobiles (Ligthart and Geboers, 1995). The narrow bore (4 mm outer diameter) and uniform color make it ideal for this purpose. The lamp runs on dc electricity supply and starts virtually instantly, in common with LED's, so that the human response is 150 msec

faster than for a comparable incandescent lamp with a red filter. Efficacy is 13 lm/W, comparable to incandescent lamps. These narrow-bore lamps run with a discharge current of 8 mA, the current density being comparable to (or higher than) that of standard fluorescent lamps. In the 2–20 torr pressure range, neon is also the best of the rare gases in providing visible-light discharges from vuv when converted by currently available phosphors (Roozekrans *et al.*, 1998). Use of a green-emitting phosphor together with the visible radiation can provide an amber light suitable for turning signals on automobiles. The discharge in narrow-bore Ne lamps is rather similar to that in He-Ne lasers, except that no gain is available without the $He^* + Ne$ excitation transfer reaction.

Sommerer and Doughty (1998) performed a comprehensive set of experiments, supported by numerical modeling, to investigate the potential of xenon discharges as a replacement for fluorescent lamps. While they were able to demonstrate 147-nm radiation output of order $15\,W\,m^{-1}$ at efficiencies of 80%, there was a strong tradeoff between efficiency and output, the efficiency showing a marked decrease as electrical power increased. These lamps cannot therefore compete with fluorescent lamps under the constraints of unit quantum efficiency imposed by the current generation of phosphors.

C. Alternative radiators

The search for alternative atomic emitters to replace mercury as a source of UV radiation for excitation of phosphors has been thorough, since the scope is limited to the Periodic Table. When molecular emitters are considered, many more possibilities become apparent, and the search for alternatives to mercury has only been superficial.

Sulfur vapor in electrodeless discharges was originally investigated as a source of UV for photolithography and for phosphor excitation because of the strong diatomic bands S_2: $B^3\Pi$-$X^3\Sigma$ (Peterson and Schlie, 1980). It was discovered that sulfur at high pressures could also be used as a source of continuum emission for white-light generation, and the use as a phosphor excitation medium was abandoned. Measurements of the conversion efficiency (rf to UV) also proved to be on the order of only 10% (Gibson *et al.*, 1996).

Other molecular radiators that have been investigated are the aluminum trihalides. Electrodeless excitation was required because electrodes are prematurely degraded by the chlorine or bromine, although cold and hot cathode discharges of this type were successfully tested. The strong 261.4-nm emission from AlCl: $A^1\Pi$-$X^1\Sigma$, for example, was particularly effective at exciting typical oxide host phosphors (Lapatovich and Gibbs, 1985).

There have also been investigations into potential atoms and molecules that radiate in the visible region of the spectrum, thus avoiding the need for a phosphor. Initial theoretical and experimental investigations (Anderson *et al.*, 1997) suggested that barium might be a suitable replacement for mercury as a low-pressure discharge light source. The barium atom has a green resonance line at 553.5 nm, at the center of the eye's photopic response curve, and the resonance level is energetically located less than halfway to the ionization limit, thereby favoring radiation over ionization processes. Calculations using a numerical model of barium rare-gas discharges (Curry *et al.*, 2000; Lister *et al.*, 2000) predicted white-light emission for a number of discharge operating parameters. Further experimental work (Laski *et al.*, 2002; Peng *et al.*, 2002) measured lower than expected radiative efficiency, largely due to the amount of electrical power dissipated in near-IR spectral lines, which did not contribute to the visible spectrum of the lamp.

The highest efficacies were achieved for barium vapor pressures corresponding to arc wall temperatures of 700 °C. Barium reacts with a wide variety of standard lamp materials including glass, silica, and polycrystalline aluminum, and the only suitable material was yttria (Y_2O_3). Lamp operation at such high temperatures implies the need for short, high-voltage lamps. However, the maintenance field of the positive column in these discharges was found to be of order 100 V/m, similar to fluorescent lamps, requiring long lamps in order to provide the necessary luminance.

D. Dielectric-barrier discharge lamps

Lamps using a dielectric-barrier discharge are finding increasing applications as UV sources (Kogelschatz and Salge, 2001). Recently, Osram introduced a new lamp, PLANON® based on this principle, which, through pulsed excitation, has achieved an efficiency of 60% conversion from electrical power to vuv xenon excimer radiation. The lamp is filled with 100-torr xenon, is extremely thin (~ 10 mm), and has a large surface area ($\sim 0.08\,m^2$) suitable for back-panel lighting.

The dielectric barrier discharge is a nonthermal plasma, in which the EEDF is very far from local thermal equilibrium. A dielectric coating covers at least one electrode to limit the electron current. The discharge volume contains an array of high-current-density ($10–10^3\,A\,m^{-2}$) microdischarges of radii ~ 0.1 mm. In the PLANON® lamp, the duty cycle of the voltage pulse must be adjusted to minimize electron density (and hence the high-energy tail of the EEDF) while maximizing the production of metastable Xe* atoms (Vollkommer and Hitzschke, 1998). The metastable atoms then combine with ground-state Xe in a three-body reaction to produce the Xe_2^* excimer which emits a broad band centered at 172 nm.

IX. CONCLUSIONS

In the foregoing text we have traced the research and development of gas discharge lighting over the past two centuries. From the early experiments, in which light from gas discharges was merely a curiosity, to current

activities using state-of-the-art diagnostics and numerical models to develop an increasingly varied range of lighting products, gas discharge physics has remained a lively, stimulating, and multidisciplinary field of research. In this paper, we have attempted to convey some of the flavor of the research activities that have led to the development of gas discharge light sources used today, together with a glimpse into likely future developments.

It would be impossible within the space available for this paper to cite all the excellent research that has been published in the open literature from universities, lighting companies, and research organizations. However, we have tried to include a representative sample of papers from each of the important areas in the physics of discharge lamps. There are a number of books and review papers which deal with individual topics in more detail, and these have been cited in the text where appropriate.

ACKNOWLEDGMENTS

The authors gratefully acknowledge valuable discussions and comments on the manuscript from M. Benilov, R. Garner, S. Lichtenberg, and R. Piejak.

LIST OF SYMBOLS

Subscripts: e, electrons; i, ions; l, lower level; u, upper level

A_R	Richardson's coefficient	Eq. (5.22)
c	speed of light in vacuum	Eq. (5.5)
C_p	specific heat at constant pressure	
D	distance traveled by ray	Eq. (5.13)
D_a	ambipolar diffusion coefficient	Eq. (5.2)
D_{ij}	diffusion coefficient of species j through species i	Eq. (5.20)
D_j	diffusion coefficient of species j through gaseous mixture	Eq. (5.1)
e	unit charge	
$\vec{E}$	electric field	Eq. (3.1)
E_k	electric field at cathode	Eq. (5.21)
E_r	ambipolar radial electric field	Eq. (6.6)
E_s	electric field at the plasma-sheath boundary	
$f_0(\varepsilon)$	electron energy distribution function (EEDF)	Eq. (4.4)
$g(\nu-\nu_0)$	normalized spectral line shape	Eq. (5.8)
$\vec{g}$	gravitational constant	Eq. (5.4)
g_j	degeneracy, atomic level j	Eq. (5.10)
G	Gibbs free energy	Eq. (7.1)
h	Planck's constant	
I	discharge current	
I_e	electron probe current	Eq. (4.4)
I_{e0}	saturation electron probe current	
I_p	probe current	
I_T	diffusion current at anode	
$\vec{j}$	current density	Eq. (3.1)
j_{FE}	electron current density from field emission at the cathode	Eq. (5.21)
j_j	current density, charge species j	
j_{Th}	electron current density from thermal emission at the cathode	Eq. (5.21)
k_B	Boltzmann's constant	
k^+	$v_i/E^{1/2}$	Eq. (5.29)
L_p	length of probe	
m_j	particle mass, species j	
$\overline{m}_{ij}$	half reduced mass $\overline{m}_{ij}=(m_i+m_j)/2m_im_j$	Eq. (5.20)
M	atomic mass (amu)	
n	index of refraction	
n_j	particle density, species j	Eq. (5.1)
$n_j^{(el)}$	particle density, *elemental* species j	Eq. (7.5)
N	gas particle density	Eq. (5.1)
N_A	Avogadro's constant	
p	gas pressure	Eq. (5.4)
$q_e(\varepsilon)$	Coulomb cross section	Eq. (5.16)
$q_{jk}(\varepsilon)$	cross section, excitation from level j to k	Eq. (6.4)
$q_t(\varepsilon)$	total electron transport cross section	Eq. (5.15)
$\vec{r}$	position in plasma	
R_B	ballast resistance	
R_k	radius of cathode	
R_D	radius of discharge	
R_P	radius of probe	
s	distance along a ray through the discharge	Eq. (5.10)
S_j	source term, diffusion equation	Eq. (5.1)
S_H	heat source term, thermal conduction equation	Eq. (5.5)
s_P	area of probe	
t	time	
$T(R)$	Holstein transmission function with $R=\lvert\vec{r}-\vec{r}'\rvert$	Eq. (5.8)
T_j	temperature, species j	
T_k	temperature of cathode	Eq. (5.21)
U_{rad}	radiation transport energy transfer term	Eq. (5.6)
$\vec{\mathrm{v}}$	fluid velocity	Eq. (5.4)
$\mathrm{v_i}$	ion velocity	
V_0	plasma potential from knee in probe characteristics	
V_c	cathode fall voltage	Eq. (5.27)
V_f	floating probe voltage	
V_p	probe voltage	Eq. (4.4)
V_w	sheath voltage at the wall	Eq. (6.15)

w_{mech}	power per unit length dissipated by mechanism	Eq. (6.8)
W_{mech}	power dissipated by mechanism	Eq. (3.2)
α_0	absorption coefficient at line center	Eq. (5.8)
$\alpha'(\nu,s)$	effective spectral absorption coefficient	Eq. (5.10)
β	ratio of ion to electron current at cathode	Eq. (5.33)
β_{jk}	trapped decay rate, levels $j \rightarrow k$	Eq. (6.5)
γ_E	ratio of conductivities	Eq. (5.16)
$\Gamma(\nu,s)$	spectral radiance	Eq. (5.10)
Γ_j	particle flux density, species j	Eq. (6.12)
δ_c	cathode sheath width	Eq. (5.28)
δ_s	collisional skin depth	Eq. (5.35)
$\Delta\phi$	Schottky correction to the work function	Eq. (5.24)
ε	electron energy	
ε_0	permittivity of free space	
ε_k	emissivity of cathode material	Eq. (7.11)
ε_{ij}	Lennard-Jones potential parameter	Eq. (5.17)
ε_{is}	ion kinetic energy at the Bohm velocity	Eq. (5.27)
ε_j	excitation energy, level j	
ε_m	emissivity of arc tube wall material	Eq. (7.9)
ε_w	energy of electrons to the wall	Eq. (6.13)
ζ_{kj}	stochiometry coefficients for molecular species k element j	Eq. (7.5)
$\Psi(r)$	Lennard-Jones potential	Eq. (5.17)
η_g	gas viscosity	Eq. (5.19)
κ_g	thermal conductivity of gas	Eq. (5.18)
κ_c	thermal conductivity of cathode material	Eq. (7.11)
λ_{cx}	ion mean free path for charge exchange	Eq. (5.29)
λ_e	electron mean free path	
λ_D	Debye length	
λ_i	ion mean free path	
λ_{IL}	ionization length	
λ_{jk}	wavelength, transition j to k	
λ_{TR}	ion thermal relaxation length	
λ_ε	electron energy relaxation length	
$\ln\Lambda$	Coulomb logarithm	Eq. (5.16)
μ_j	Charged-particle mobility	Eq. (5.3)
ν	rf or microwave frequency (cycles/s)	
$\nu(y)$	Fowler-Nordheim function, $y=\Delta\phi/(\phi-\varepsilon)$	Eq. (5.25)
$\nu_m(\varepsilon)$	collision frequency for electron momentum transfer	Eq. (5.14)
ν_{pe}	electron plasma frequency	
ρ	mass density of gas	Eq. (5.4)
σ_B	Stefan-Boltzmann constant	
σ_e	electrical conductivity	Eq. (3.1)
σ_{ij}	Lennard-Jones effective collision diameter	Eq. (5.17)
τ	optical depth	Eq. (5.13)
τ_v	radiative lifetime in vacuum	Eq. (5.7)
ϕ_{eff}	effective work function of cathode	Eq. (5.23)
ϕ	work function of cathode material	Eq. (5.23)
χ_j	chemical potential of the jth species	Eq. (7.1)
ω	rf excitation frequency (radians/s)	Eq. (5.35)
ω_{pe}	electron plasma frequency (radians/s)	Eq. (5.35)
$d\Omega$	differential of solid angle	
$\Omega^{(k,l)*}(T^*)$	omega integral from Lennard-Jones potential	Eq. (5.18)

REFERENCES

Abeywickrama, M. G., 1997, in *Lamps and Lighting*, edited by J. R. Coaton and A. M. Marsden (Arnold, London), p. 194.

Adler, H., L. Riley, and J. E. Lawler, 2001, in *Proceedings of the 9th International Symposium on the Science and Technology of Light Sources LS-9*, Ithaca, edited by R. S. Bergman (Cornell University, Ithaca, NY), p. 129.

Adriaansz, M., and L. Vriens, 1976, Philips Res. Rep. **31**, 193.

Aicher, J. O., and E. Lemmers, 1957, Illum. Eng. (N.Y.) **52**, 579.

Aicher, J. O., and E. Lemmers, 1960, Illum. Eng. (N.Y.) **55**, 39.

Alexandrovich, B. M., R. B. Piejak, and V. A. Godyak, 1996, J. Illum. Eng. Soc. **25**, 93.

Allen, G. R., R. Lagushenko, J. Maya, and W. M. Keeffe, 1987, J. Illum. Eng. Soc. **16**, 13.

Almanstötter, J., B. Eberhard, K. Günther, and T. Hartmann, 2002, J. Phys. D **35**, 1751.

Amakawa, T., J. Jenista, J. Heberlein, and E. Pfender, 1998, J. Phys. D **31**, 2826.

Anderson, H. M., J. MacDonagh-Dumler, and J. E. Lawler, 1997, *IEEE Conference Record-Abstracts, 1997 International Conference on Plasma Science* (IEEE, New York), p. 247.

Anderson, J. M., 1970, U.S. Patent No. 3,500,118.

Anderson, L. W., A. N. Goyette, and J. E. Lawler, 2000, Adv. At., Mol., Opt. Phys. **43**, 295.

Antón, J. C., C. Blanco, F. Ferrero, P. Rolán, and G. Zissis, 2002, in *37th IEEE Industry Applications Society Annual Meeting* (IEEE, Piscataway, NJ), p. 1494.

Asselman, A., M. Aubes, J. J. Damelincourt, and J. Salon, 1992, J. Appl. Phys. **71**, 4739.

Aubrecht, V., and J. J. Lowke, 1994, J. Phys. D **27**, 2066.

Bakker, L. P., and G. M. W. Kroesen, 2000, Appl. Phys. Lett. **76**, 1528.

Bartschat, K., 2002a, in *Atomic and Molecular Data and Their Applications*, AIP Conference Proceedings No. 636, edited by D. R. Schultz, P. S. Krstic, and F. Ownby (AIP, Melville, NY), p. 192.

Bartschat, K., 2002b, private communication.

Bartels, H., 1949a, Z. Phys. **125**, 597.

Bartels, H., 1949b, Z. Phys. **126**, 108.

Becquerel, E., 1867, *La Lumière—Ses Causes et Ses Effets* (Librairie de Firmin Didot Frêres, Fils et Cie, Paris).

Benck, E. C., J. E. Lawler, and J. T. Dakin, 1989, J. Opt. Soc. Am. B **6**, 11.
Beneking, C., 1990a, J. Appl. Phys. **68**, 5435.
Beneking, C., 1990b, J. Appl. Phys. **68**, 4461.
Beneking, C., and P. Anderer, 1992, J. Phys. D **25**, 1470.
Benilov, M. S., 1998, Phys. Rev. E **58**, 6480.
Benilov, M. S., and S. Coulombe, 2001, Phys. Plasmas **8**, 4227.
Benilov, M. S., and M. D. Cunha, 2002, J. Phys. D **35**, 1736.
Benilov, M. S., and M. D. Cunha, 2003a, J. Phys. D **36**, 603.
Benilov, M. S., and M. D. Cunha, 2003b, Phys. Rev. E **68**, 056407.
Bethenod, J., and A. Claude, 1936, U.S. Patent No. 2,030,957.
Bhattacharya, A. K., 1989a, J. Appl. Phys. **65**, 4595.
Bhattacharya, A. K., 1989b, J. Appl. Phys. **65**, 4603.
Biberman, L. M., 1947, Zh. Eksp. Teor. Fiz. **17**, 416.
Bigio, L., 1988, J. Appl. Phys. **63**, 5259.
Bigio, L., and J. T. Dakin, 1989, J. Appl. Phys. **65**, 375.
Bigio, L., and D. Johnson, 1991, J. Opt. Soc. Am. B **8**, 525.
Bloem, J., A. Bouwknegt, and G. A. Wesselink, 1978/79, Philips Tech. Rev. **38**, 83.
Boghosian, S., and G. N. Papatheodorou, 1996, in *Handbook of the Physics and Chemistry of the Rare Earths 23*, edited by K. A. Gschneider and L. Eyriung (Elsevier Science, Amsterdam), p. 435.
Bohm, D., 1949, *The Characteristics of Electric Discharges in Magnetic Fields*, edited by A. Guthry and R. K. Wakerling (McGraw-Hill, New York).
Bonvallet, G. A., and J. E. Lawler, 2003, J. Phys. D **36**, 1510.
Born, M., 1999, J. Phys. D **32**, 876.
Born, M., 2001, J. Phys. D **34**, 909.
Bötticher, R., and W. Bötticher, 2000, J. Phys. D **33**, 367.
Bousquet, C., and N. Bras, 1977, J. Phys. (Paris) **38**, 139.
Bousquet, C., and N. Bras, 1980, J. Phys. (Paris) **41**, 19.
Bowden, M. D., Y. Goto, H. Yanaga, P. J. A. Howarth, K. Uchino, and K. Muraoka, 1999, Plasma Sources Sci. Technol. **8**, 203.
Buie, M. J., J. T. P. Pender, J. P. Holloway, T. Vincent, P. L. G. Ventzek, and M. L. Brake, 1996, J. Quant. Spectrosc. Radiat. Transf. **55**, 231.
Burgess, R. E., H. Kroemer, and J. M. Houston, 1953, Phys. Rev. **90**, 515.
Burnett, K., 1985, Phys. Rep. **118**, 339.
Callahan, S. L., and W. P. Lapatovich, 2002, SAE Technical Paper 2002-01-0976, in *Advanced Lighting Technology for Vehicles, Proceedings of the Society of Automotive Engineers World Congress*, Detroit (Soc. Auto. Eng., Warrendale, PA).
Cayless, M. A., 1958, J. Electron. Control **4**, 2.
Cayless, M. A., 1960, Br. J. Appl. Phys. **11**, 492.
Cayless, M. A., 1963, Br. J. Appl. Phys. **14**, 863.
Cayless, M. A., 1986, in *Radiative Processes in Discharge Plasmas*, Vol. 149 of *NATO Advanced Study Institute, Series B: Physics*, edited by J. M. Proud and L. H. Luessen (Plenum, New York), p. 249.
Chang, P. Y., and W. Shyy, 1991, Int. J. Heat Mass Transfer **34**, 1811.
Chang, P. Y., and W. Shyy, 1992, Int. J. Heat Mass Transfer **35**, 1857.
Chang, P. Y., W. Shyy, and J. T. Dakin, 1990, Int. J. Heat Mass Transfer **33**, 483.
Chanin, L. M., 1978, in *Gaseous Electronics* edited by Merle N. Hirsh and H. J. Oskam (Academic, New York), Vol. 1, p. 133.
Chen, F. F., 1965, in *Plasma Diagnostic Techniques*, edited by R. H. Huddlestone and S. L. Leonard (Academic, New York), p. 113.
Chen, F. F., 1974, *Introduction to Plasma Physics* (Plenum, New York), p. 104.
Cherrington, B. E., 1982, Plasma Chem. Plasma Process. **2**, 113.
Coaton, J. R., and A. M. Marsden, 1997, Eds., *Lamps and Lighting* (Arnold, London).
Coe, S. E., and G. G. Lister, 1992, J. Appl. Phys. **71**, 4781.
Coe, S. E., J. A. Stocks, and A. J. Tambini, 1993, J. Phys. D **26**, 1203.
Cohen, J. S., R. L. Martin, and L. A. Collins, 2002, Phys. Rev. A **66**, 012717.
Cornelissen, H. J., and A. L. J. Burgmans, 1982, Opt. Commun. **41**, 187.
Cornelissen, H. J., and H. J. H. Merks-Eppingbroek, 1986, J. Appl. Phys. **59**, 2324.
Corney, A., 1977, *Atomic and Laser Spectroscopy* (Clarendon, Oxford), p. 263.
Cruise, D. R., 1964, J. Phys. Chem. **68**, 3797.
Curry, J. J., H. G. Adler, S. D. Shastri, and J. E. Lawler, 2001, Appl. Phys. Lett. **79**, 1974.
Curry, J. J., H. M. Anderson, J. MacDonagh-Dumler, J. E. Lawler, and G. G. Lister, 2000, J. Appl. Phys. **87**, 2058.
Curry, J. J., J. E. Lawler, and G. G. Lister, 1999, J. Appl. Phys. **86**, 731.
Curry, J. J., G. G. Lister, and J. E. Lawler, 2002, J. Phys. D **35**, 2945.
Curry, J. J., M. Sakai, and J. E. Lawler, 1998, J. Appl. Phys. **84**, 3066.
Dabringhausen, L., D. Nandelstädt, J. Luhmann, and J. Mentel, 2002, J. Phys. D **35**, 1621.
Dakin, J. T., 1986, J. Appl. Phys. **60**, 563.
Dakin, J. T., and R. P. Gilliard, 1987, J. Appl. Phys. **62**, 79.
Dakin, J. T., T. H. Rautenberg, and E. M. Goldfield, 1989, J. Appl. Phys. **66**, 4074.
Davies, P. G., J. Dutton, F. Llewellyn-Jones, and E. M. Williams, 1966, Philos. Trans. R. Soc. London, Ser. A **259**, 299.
de Groot, J. J., A. G. Jack, and H. Coenen, 1984, J. Illum. Eng. Soc. **14**, 188.
de Groot J. J., and J. A. J. M. van Vliet, 1986, *The High Pressure Sodium Lamp* (Kluwer Technische Boeken, Deventer).
Den Hartog, E. A., D. A. Doughty, and J. E. Lawler, 1988, Phys. Rev. A **38**, 2471.
Denneman, J. W., 1981, IEE Proc., Part A: Phys. Sci., Meas. Instrum., Manage. Educ. **128A**, 397.
Denneman, J. W., 1990, J. Phys. D **23**, 293.
Derra, G., H. Moench, E. Fischer, and X. Riederer, 2001, in *Proceedings of the 9th International Symposium on the Science and Technology of Light Sources LS-9*, Ithaca, edited by R. S. Bergman (Cornell University, Ithaca, NY), p. 31.
DiChristina, M., 1995, Pop. Sci. (U.S.) **255** (2), 1.
Dorleijn, J. W. F., and A. G. Jack, 1985, J. Illum. Eng. Soc. **15** (1), 75.
Doughty, D. A., and D. F. Fobare, 1995, Rev. Sci. Instrum. **66**, 4834.
Doughty, D. K., and J. E. Lawler, 1983, Phys. Rev. A **28**, 773.
Doughty, D. K., and J. E. Lawler, 1984, Appl. Phys. Lett. **45**, 611.
Druyvesteyn, M. J., 1930, Z. Phys. **64**, 781.
Druyvesteyn, M. J., 1934, Physica (Amsterdam) **1**, 14.

Druyvesteyn, M. J., and F. M. Penning, 1940, Rev. Mod. Phys. **12**, 87.
Duffy, M. E., J. T. Dakin, G. E. Duffy, and M. M. Secen, 1992, in *Proceedings of the 6th International Symposium on the Science and Technology of Light Sources, LS-6*, Budapest, edited by L. Bartha and F. J. Kedves (Technical University of Budapest, Budapest), p. 325.
Dyke, W. P., and W. W. Dolan, 1956, in *Advances in Electronics and Electron Physics, Vol. VIII*, edited by L. Marton (Academic, New York), p. 90.
Easley, M. A., 1951, J. Appl. Phys. **22**, 590.
Ecker, G., 1961, Ergeb. Exakten Naturwiss. **33**, 1.
Elenbaas, W., 1951, *The High Pressure Mercury Vapour Discharge* (North-Holland–Interscience, Amsterdam).
England, J. P., and M. T. Elford, 1991, Aust. J. Phys. **44**, 647.
Fischer, E., 1976, J. Appl. Phys. **47**, 2954.
Fischer, E., 1987, Philips J. Res. **42**, 58.
Flesch, P., and M. Neiger, 2002, J. Phys. D **35**, 1681.
Fohl, T., J. M. Kramer, and J. E. Lester, 1993, J. Appl. Phys. **73**, 46.
Franck, G., 1971, Z. Naturforsch. A **26a**, 150.
Fromm, D. C., G. H. Lieder, and K. H. Gleixner, 2002, J. Phys. D **35**, 1668.
Fuhr, J. R., and W. L. Wiese, 1998, in *CRC Handbook of Chemistry and Physics, 79th Ed.*, edited by D. R. Lide (CRC, Boca Raton, FL), Vol. 10, p. 88.
Fursa, D. V., I. Bray, and G. Lister, 2003, J. Phys. B **36**, 4255.
Gentle, K. W., 1995, Rev. Mod. Phys. **67**, 809.
Gibson, N. D., U. Kortshagen, and J. E. Lawler, 1996, J. Appl. Phys. **79**, 7523.
Gibson, N. D., and J. E. Lawler, 1996, J. Appl. Phys. **79**, 86.
Godyak, V. A., 1990, in *Surface Interaction and Processing of Materials*, Vol. 179 of *NATO Advance Study Institute, Series E: Applied Sciences*, edited by O. Auciello *et al.* (Kluwer, Dordrecht), p. 95.
Godyak, V. A., 2002, IEEE Ind. Appl. Mag. **8** (May/June), 42.
Godyak, V. A., R. B. Piejak, and B. M. Alexandrovich, 1993, J. Appl. Phys. **73**, 3657.
Godyak, V., R. Piejak, and B. Alexandrovich, 2001, in *Proceedings of the 9th International Symposium on the Science and Technology of Light Sources LS-9*, Ithaca, edited by R. S. Bergman (Cornell University, Ithaca, NY), p. 157.
Godyak, V., and J. Shaffer, 1998, in *Proceedings of the 8th International Symposium on the Science and Technology of Light Sources LS-8*, Greifswald, edited by G. Babucke (Institute for Low Temperature Plasma Physics, Greifswald, Germany), p. 14.
Grossman, M. W., R. Lagushenko, and J. Maya, 1986, Phys. Rev. A **34**, 4094.
Guest, R. A., and E. J. P. Mascarenhas, 1997, in *Lamps and Lighting*, edited by J. R. Coaton and A. M. Marsden (Arnold, London), p. 292.
Hartel, G., H. Schöpp, H. Hess, and L. Hitzschke, 1999, J. Appl. Phys. **85**, 7076.
Hartmann, T., K. Günther, S. Lichtenberg, D. Nandelstädt, L. Dabringhausen, M. Redwitz, and J. Mentel, 2002, J. Phys. D **35**, 1657.
Hashiguchi, S., K. Hatase, S. Mori, and K. Tachibana, 2002, J. Appl. Phys. **92**, 45.
Haverlag, M., A. Kŕaus, J. Sormani, J. Heuvelmans, A. Geven, L. Kaldenhoven, and G. Heijne, 2002, J. Phys. D **35**, 1695.
Hebner, G. A., J. T. Verdeyen, and M. J. Kushner, 1988, J. Appl. Phys. **63**, 2226.
Herrmann, G., and H. Wagener, 1951, *The Oxide Coated Cathode* (Chapman and Hall, London), Vol. 2, p. 171.
Hershkowitz, N., 1989, in *Plasma Diagnostics, Volume 1: Discharge Parameters and Chemistry*, edited by O. Auciello and D. L. Flamm (Academic, New York), p. 113.
Hilpert, K., 1989, J. Electrochem. Soc. **136**, 2099.
Hilpert, K., and U. Niemann, 1997, Thermochim. Acta **299** (1-2), 49.
Hirschfelder, J. O., C. F. Curtiss, and R. B. Bird, 1954, *Molecular Theory of Gases and Liquids* (Wiley, New York).
Hollo, S., 1997, in *Lamps and Lighting*, edited by J. R. Coaton and A. M. Marsden (Arnold, London), p. 235.
Holstein, T., 1947, Phys. Rev. **72**, 1212.
Holstein, T., 1951, Phys. Rev. **83**, 1159.
Ingold, J. H., 1991a, J. Appl. Phys. **69**, 6910.
Ingold, J. H., 1991b, Phys. Rev. A **43**, 3093.
Irons, F. E., 1979a, J. Quant. Spectrosc. Radiat. Transf. **22**, 1.
Irons, F. E., 1979b, J. Quant. Spectrosc. Radiat. Transf. **22**, 21.
Irons, F. E., 1979c, J. Quant. Spectrosc. Radiat. Transf. **22**, 37.
Jack, A. G., and M. Koedam, 1974, J. Illum. Eng. Soc. **3**, 323.
Jeffries, J. T., and O. R. White, 1960, Astrophys. J. **132**, 767.
Johnston, C. W., H. W. P. van der Heijden, G. M. Janssen, J. van Dijk, and J. J. A. M. van der Mullen, 2002, J. Phys. D **35**, 342.
Jonkers, J., M. Bakker, and J. A. M. van der Mullen, 1997, J. Phys. D **30**, 1928.
Karabourniotis, D., 1986, in *Radiative Processes in Discharge Plasmas*, Vol. 149 of *NATO Advanced Study Institute, Series B: Physics*, edited by J. M. Proud and L. H. Luessen (Plenum, New York), p. 171.
Karabourniotis, D., 2002, J. Appl. Phys. **92**, 25.
Keeffe, W. M., 1975, J. Illum. Eng. Soc. **4**, 260.
Keeffe, W. M., and V. D. Meyer, 1989, in *Proceedings of the 5th International Symposium on the Science and Technology of Light Sources LS-5*, York, England, edited by R. Devonshire, J. Meads, and D. O. Wharmby (University of Sheffield, Sheffield, UK), p. 117.
Kenty, C., 1950, J. Appl. Phys. **21**, 1309.
Kenty, C., M. A. Easley, and B. T. Barnes, 1951, J. Appl. Phys. **22**, 1006.
Kettlitz, M., and R. Großjohann, 2002, J. Phys. D **35**, 1702.
Kirby, M. W., 1997a, in *Lamps and Lighting*, edited by J. R. Coaton and A. M. Marsden (Arnold, London), p. 227.
Kirby, M. W., 1997b, in *Lamps and Lighting*, edited by J. R. Coaton and A. M. Marsden (Arnold, London), p. 252.
Kloss, A., H. Schneidenbach, H. Schöpp, H. Hess, L. Hitzschke, and B. Schalk, 2000, J. Appl. Phys. **88**, 1271.
Koedam, M., and A. A. Kruithof, 1962, Physica (Amsterdam) **28**, 80.
Koedam, M., A. A. Kruithof, and J. Riemens, 1963, Physica (Amsterdam) **29**, 565.
Kogelschatz, U., and J. Salge, 2001, in *Low Temperature Plasma Physics: Fundamental Aspects and Applications*, edited by R. Hippler, S. Pfau, M. Schmidt, and K. H. Schoenbach (Wiley, Berlin), p. 331.
Kortshagen, U., C. Busch, and L. D. Tsendin, 1996, Plasma Sources Sci. Technol. **5**, 1.
Koury, F., W. C. Gungle, and J. F. Waymouth, 1975, J. Illum. Eng. Soc. **4**, 106.
Kovar, F. R., 1964, Phys. Rev. **133**, A681.
Kramer, J., 1988, J. Appl. Phys. **64**, 1758.
Kramer, J., 1990a, J. Appl. Phys. **67**, 2289.
Kramer, J., 1990b, J. Appl. Phys. **68**, 1513.

Kramer, J., 1991a, J. Appl. Phys. **70**, 628.
Kramer, J., 1991b, J. Appl. Phys. **70**, 636.
Kreher, J., and W. Stern, 1988, Contrib. Plasma Phys. **28**, 185.
Kreher, J., and W. Stern, 1989, Contrib. Plasma Phys. **29**, 181.
Langmuir, I., 1929, Phys. Rev. **33**, 954.
Lankhorst, M. H. R., and U. Niemann, 2000, J. Alloys Compd. **308**, 280.
Lankhorst, M. H. R., W. Keur, and H. A. M. van Hal, 2000, J. Alloys Compd. **309**, 188.
Lapatovich, W. P., 1995, in *Proceedings of the 7th International Symposium on the Science and Technology of Light Sources LS-7*, Kyoto, edited by R. Itatani and S. Kamiya (Illuminating Engineering Institute of Japan, Tokyo), p. 139.
Lapatovich, W. P., and G. R. Gibbs, 1985, U.S. Patent No. 4,492,898.
Laski, J., G. G. Lister, F. Palmer, P. E. Moskowitz, and J. J. Curry, 2002, J. Appl. Phys. **91**, 1772.
Lawler, J. E., 1980, Phys. Rev. A **22**, 1025.
Lawler, J. E., 1987, in *Lasers, Spectroscopy and New Ideas—A Tribute to Arthur L. Schawlow*, Springer Series in Optical Sciences No. 54, edited by W. M. Yen and M. D. Levenson (Springer-Verlag, Berlin), p. 125.
Lawler, J. E., and J. J. Curry, 1998, J. Phys. D **31**, 3235.
Lawler, J. E., J. J. Curry, and G. G. Lister, 2000, J. Phys. D **33**, 252.
Lawler, J. E., and J. T. Dakin, 1989, J. Opt. Soc. Am. B **6**, 1457.
Lawler, J. E., E. A. Den Hartog, and W. N. G. Hitchon, 1991, Phys. Rev. A **43**, 4427.
Lawler, J. E., and D. A. Doughty, 1994, Adv. At., Mol., Opt. Phys. **34**, 171.
Lawler, J. E., D. A. Doughty, and G. G. Lister, 2002, J. Phys. D **35**, 1613.
Lawler, J. E., G. J. Parker, and W. N. G. Hitchon, 1993, J. Quant. Spectrosc. Radiat. Transf. **49**, 627.
Lee, J.-S., 1974, Astrophys. J. **192**, 465.
Lee, J.-S., 1977, Astrophys. J. **218**, 857.
Lee, J.-S., 1982, Astrophys. J. **255**, 303.
Lichtenberg, S., 2003, private communication.
Lichtenberg, S., D. Nandelstädt, L. Dabringhausen, M. Redwitz, J. Luhmann, and J. Mentel, 2002, J. Phys. D **35**, 1648.
Lieberman, M. A., and A. J. Lichtenberg, 1994, in *Principles of Plasma Discharges and Materials Processing* (Wiley, New York), p. 320.
Ligthart, F. A. V., and J. Geboers, 1995, in *Proceedings of the 7th International Symposium on the Science and Technology of Light Sources LS-7, Kyoto*, edited by R. Itatani and S. Kamiya (Illuminating Engineering Institute of Japan, Tokyo), p. 267.
Lister, G. G., 1999, in *Advanced Technologies Based on Wave and Beam Generated Plasmas*, edited by H. Schlüter and A. Shivarova (Kluwer Academic, Dordrecht), p. 65.
Lister, G. G., 2003, Phys. Plasmas **10**, 2136.
Lister, G. G., and S. E. Coe, 1993, Comput. Phys. Commun. **75**, 160.
Lister, G. G., and M. Cox, 1992, Plasma Sources Sci. Technol. **1**, 67.
Lister, G. G., J. J. Curry, and J. E. Lawler, 2000, Phys. Rev. E **62**, 5576.
Lister, G. G., V. A. Sheverev, and D. Uhrlandt, 2002, J. Phys. D **35**, 2586.
Lister, G. G., and J. F. Waymouth, 2001, in *Encyclopedia of Physical Science and Technology*, 3rd ed., Editor-in-Chief R. A. Meyers (Academic, San Diego), Vol. 8, p. 557.
Lowke, J. J., 1969, J. Quant. Spectrosc. Radiat. Transf. **9**, 839.
Lowke, J. J., 1970, J. Appl. Phys. **41**, 2588.
Lowke, J. J., R. J. Zollweg, and R. W. Liebermann, 1975, J. Appl. Phys. **46**, 650.
Luhmann, J., S. Lichtenberg, O. Langenscheidt, M. S. Benilov, and J. Mentel, 2002, J. Phys. D **35**, 1631.
Maya, J., M. W. Grossman, R. Lagushenko, and J. F. Waymouth, 1984, Science **226**, 435.
Maya, J., and R. Lagushenko, 1989, Adv. At., Mol., Opt. Phys. **26**, 321.
McKeag, A. H., and P. W. Ranby, 1942, GB Patent No. 578 192.
Menningen, K. L., and J. E. Lawler, 2000, J. Appl. Phys. **88**, 3190.
Miller, P. A., J. T. Verdeyen, and B. E. Cherrington, 1971, Phys. Rev. A **4**, 692.
Moisan, M., J. Hubert, J. Margot, G. Sauvé, and Z. Zakrzewski, 1993, in *Microwave Discharges, Fundamentals and Applications*, Vol. 302 of *NATO ASI Series B: Physics*, edited by C. M. Ferreira and M. Moisan (Plenum, New York), p. 1.
Moisan, M., J. Hubert, J. Margot, and Z. Zakrzewski, 1999, in *Advanced Technologies Based on Wave and Beam Generated Plasmas*, Vol. 67 of *NATO Science Series 3: High Technology*, edited by H. Schlüter and A. Shivarova (Kluwer Academic, Dordrecht), p. 23.
Molisch, A. F., and B. P. Oehry, 1998, *Radiation Trapping in Atomic Vapours* (Clarendon, Oxford).
Molisch, A. F., B. P. Oehry, W. Schupita, and G. Magerl, 1993, J. Quant. Spectrosc. Radiat. Transf. **49**, 361.
Moore, J. R., 1980, Light. Res. Technol. **12**, 213.
Morgan, W. L., and L. Vriens, 1980, J. Appl. Phys. **51**, 5300.
Moshkalyov, S. A., C. Thompson, T. Morrow, and W. G. Graham, 2000, J. Vac. Sci. Technol. A **18**, 1395.
Muckenfuss, C., and C. F. Curtiss, 1958, J. Chem. Phys. **29**, 1273.
Murakami, H., 1995, in *Proceedings of the 7th International Symposium on the Science and Technology of Light Sources LS-7*, Kyoto, edited by R. Itatani and S. Kamiya (Illuminating Engineering Institute of Japan, Tokyo), p. 285.
Muroka, K., 2001, in *Proceedings of the 10th International Symposium on Laser-Aided Plasma Diagnositics*, edited by K. Muroka (Kyushu University, Fukuoka, Japan), p. 1.
Muroka, K., K. Uchino, and M. D. Bowden, 1998, Plasma Phys. Controlled Fusion **40**, 1221.
Nandelstädt, D., M. Redwitz, L. Dabringhausen, J. Luhmann, S. Lichtenberg, and J. Mentel, 2002, J. Phys. D **35**, 1639.
Netten, A., and C. M. Verheij, 1994, *QL Lighting Product Presentation Storybook*, Product Literature (Philips Lighting, Eindhoven).
Nordheim, L. W., 1928, Proc. R. Soc. London, Ser. A **121**, 626.
Nottingham, W. B., 1956, in *Handbuch der Physik*, edited by S. Flügge (Springer-Verlag, Berlin), Vol. XXI, p. 1.
Offermanns, S., 1990, J. Appl. Phys. **67**, 115.
Parker, G. J., W. N. G. Hitchon, and J. E. Lawler, 1993, J. Phys. B **26**, 4643.
Payne, M. G., J. E. Talmage, G. S. Hurst, and E. B. Wagner, 1974, Phys. Rev. A **9**, 1050.
Peng, X. L., J. J. Curry, G. G. Lister, and J. E. Lawler, 2002, J. Appl. Phys. **91**, 1761.
Penning, F. M., 1928, Z. Phys. **46**, 335.
Peterson, D. A., and L. A. Schlie, 1980, J. Chem. Phys. **73**, 1551.
Petrov, G., 2002, private communication.
Petrov, G., and J. L. Giuliani, 2003, J. Appl. Phys. **94**, 62.

Phelps, A. V., 2001, private communication (unpublished data, available at jilawww.colorado.edu/www/research/colldata.html).
Polman, J., H. van Tongeren, and T. G. Verbeek, 1975, Philips Tech. Rev. **35**, 321.
Popov, O. A., and R. Chandler, 2002, Plasma Sources Sci. Technol. **11**, 218.
Post, H. A., 1986, Phys. Rev. A **33**, 2003.
Post, H. A., P. van de Weijer, and R. M. M. Cremers, 1986, Phys. Rev. A **33**, 2017.
Preston, B., and E. C. Odell, 1997, in *Lamps and Lighting*, edited by J. R. Coaton and A. M. Marsden (Arnold, London), p. 263.
Proud, J. M., and R. K. Smith, 1981, U.S. Patent No. 4,266,166.
Pursch, H., H. Schoepp, M. Kettlitz, and H. Hess, 2002, J. Phys. D **35**, 1757.
Rockwood, S. D., 1973, Phys. Rev. A **8**, 2348.
Rogoff, G. L., 1985, J. Phys. D **18**, 1533.
Rogoff, G. L., A. E. Feuersanger, J. P. Drummey, and H. L. Rothwell, Jr., 1987, J. Appl. Phys. **62**, 4084.
Roozekrans, C., F. Ligthart, and J. Geboers, 1998, in *Proceedings of the 8th International Symposium on the Science and Technology of Light Sources LS-8*, Greifswald, edited by G. Babucke (Institute for Low Temperature Plasma Physics, Greifswald, Germany), p. 138.
Rowley, A. T., and D. O. Wharmby, 1992, in *Proceedings of the 6th International Symposium on the Science and Technology of Light Sources*, Budapest, edited by L. Bartha and F. J. Kedves (Technical University of Budapest, Budapest), p. 329.
Sakai, Y., S. Sawada, and H. Tagashira, 1989, J. Phys. D **22**, 276.
Sanders, N. A., and E. Pfender, 1984, J. Appl. Phys. **55**, 714.
Sansonnens, L., J. Haider, and J. J. Lowke, 2000, J. Phys. D **33**, 148.
Schäfer, R., and H. P. Stormberg, 1986, J. Appl. Phys. **60**, 1263.
Schmitz, H., and K.-U. Riemann, 2001, J. Phys. D **34**, 1193.
Schmitz, H., and K.-U. Riemann, 2002, J. Phys. D **35**, 1727.
Schottky, W., 1923, Z. Phys. **14**, 63.
Sevast'yanenko, V. G., 1998, unpublished.
Shinomaya, M., K. Kobayashi, M. Higashikawa, S. Ukegawa, J. Matsuura, and K. Tanigawa, 1991, J. Illum. Eng. Soc. **20** (1), 44.
Shkarovsky, I. P., T. W. Johnston, and M. P. Bachynski, 1966, *The Particle Kinetics of Plasmas* (Addison-Wesley, Reading, MA).
Shyy, W., and P. Y. Chang, 1990, Int. J. Heat Mass Transfer **33**, 495.
Smith, D. J., G. A. Bonvallet, and J. E. Lawler, 2003, J. Phys. D **36**, 1519.
Soloukhin, R. I., 1987, in *Handbook of Radiation Transfer in High Temperature Gases* (Hemisphere, London), p. 1.
Sommerer, T. J., and D. A. Doughty, 1998, J. Phys. D **31**, 2803.
Soules, T. F., 1997, in *Lamps and Lighting*, edited by J. R. Coaton and A. M. Marsden (Arnold, London), p. 137.
Soules, T. F., J. H. Ingold, A. K. Bhattacharya, and R. H. Springer, 1989, J. Illum. Eng. Soc. **18** (2), 81.
Spitzer, L., 1962, *Physics of Fully Ionized Gases*, 2nd ed. (Interscience, New York).
Spitzer, L., and R. Härm, 1953, Phys. Rev. **89**, 977.
Springer, R. H., and W. H. Lake, 1984, J. Illum. Eng. Soc. **13** (3), 304.
Stewart, C. S., M. E. Duffy, J. T. Dakin, V. D. Roberts, S. A. El-Hamamsy, H. L. Witting, A. Inouye, K. Shimizu, and K. Araki, 1992 in *Proceedings of the 6th International Symposium on the Science and Technology of Light Sources, LS-6*, Budapest, edited by L. Bartha and F. J. Kedves (Technical University of Budapest, Budapest), p. 319.
Stewart, R. S., I. S. Borthwick, D. J. Smith, A. M. Paterson, and C. J. Whitehead, 2000, J. Phys. D **33**, 864.
Stewart, R. S., D. J. Smith, I. S. Borthwick, and A. M. Paterson, 2000, Phys. Rev. E **62**, 2678.
Stormberg, H.-P., 1980, J. Appl. Phys. **51**, 1963.
Stormberg, H.-P., 1981, J. Appl. Phys. **52**, 3233.
Stormberg, H. P., and R. Schäfer, 1983, J. Appl. Phys. **54**, 4338.
Stull, D. R., and H. Prophet, 1971, *JANAF Thermochemical Tables*, 2nd ed., National Standards Reference Data Series, Natl. Bur. Stand. 37 (U.S. GPO, Washington, D.C.).
Thorne, A. P., U. Litzen, and S. Johansson, 1999, *Spectrophysics* (Springer, Berlin), p. 211.
Thouret, W., W. Weizel, and P. Günther, 1951, Z. Phys. **130**, 621.
Tielemans, P., and F. Oostvogels, 1983, Philips J. Res. **38**, 214.
Turner, B. P., M. G. Ury, Y. Leng, and W. G. Love, 1995, *Illuminating Engineering Society Annual Conference* (Illum. Eng. Soc., New York), Paper 87.
van den Hoek, W. J., T. L. G. Thijssen, A. J. H. van der Heijden, B. Buijsse, and M. Haverlag, 2002, J. Phys. D **35**, 1716.
van den Hoek, W. J., and J. A. Visser, 1981, J. Phys. D **14**, 1613.
van der Weijer, P., and R. M. M. Cremers, 1985a, Opt. Commun. **53**, 109.
van der Weijer, P., and R. M. M. Cremers, 1985b, Opt. Commun. **54**, 273.
van der Weijer, P., and R. M. M. Cremers, 1985c, J. Appl. Phys. **57**, 672.
van de Sande, M. J., and J. J. A. M. van der Mullen, 2002, J. Phys. D **35**, 1381.
van Dijk, J., B. Hartgers, J. Jonkers, and J. van der Mullen, 2000, J. Phys. D **33**, 2798.
van Erk, W., and T. Rietveld, 1986, in *Proceedings of the 4th International Symposium on the Science and Technology of Light Sources LS-4*, Karlsruhe, Germany (University of Karlsruhe, Karlsruhe, Germany), p. 235.
van Tongeren, H., 1975, Philips Res. Rep., Suppl. **3**, 1.
van Tongeren, H., and J. Heuvelmans, 1974, J. Appl. Phys. **45**, 3844.
van Trigt, C., 1969, Phys. Rev. **181**, 97.
van Trigt, C., 1970, Phys. Rev. A **1**, 1298.
van Trigt, C., 1971, Phys. Rev. A **4**, 1303.
van Trigt, C., 1976a, Phys. Rev. A **13**, 726.
van Trigt, C., 1976b, Phys. Rev. A **13**, 734.
Vermeersch, F., and W. Wieme, 1991, in *Optogalvanic Spectroscopy*, edited by R. S. Stavart and J. E. Lawler, IOP Conf. Proc. No. 113 (Institute of Physics, London), p. 109.
Verstegen, J. M. P. J., 1974, Light. Res. Technol. **6**, 31.
Verstegen, J. M. P. J., D. Radielovic, and L. E. Vrenken, 1974, J. Electrochem. Soc. **121**, 1627.
Verweij, W., 1961, Philips Res. Rep., Suppl. **2**, 1.
Vollkommer, F., and L. Hitzschke, 1998, in *Proceedings of the 8th International Symposium on the Science and Technology of Light Sources LS-8*, Greifswald, edited by G. Babucke (Institute for Low Temperature Plasma Physics, Greifswald, Germany), p. 51.
Vos, T., F. Ligthart, M. Hendrix, T. Stommen, U. Chittka, J. v. d. Mullen, and W. v. d. Bosch, 1998, in *Proceedings of the 8th International Symposium on the Science and Technology of*

Light Sources LS-8, Greifswald, edited by G. Babucke (Institute for Low Temperature Plasma Physics, Greifswald, Germany), p. 288.
Vriens, L., 1973, Phys. Rev. Lett. **30**, 585.
Vriens, L., 1978, J. Appl. Phys. **49**, 3814.
Vriens, L., and M. Adriaansz, 1974, J. Appl. Phys. **45**, 4422.
Vriens, L., R. A. J. Keijser, and F. A. S. Ligthart, 1978, J. Appl. Phys. **49**, 3807.
Vriens, L., and A. H. M. Smeets, 1980, Phys. Rev. A **22**, 940.
Walsh, P. J., 1957, Phys. Rev. **107**, 338.
Wamsley, R. C., J. E. Lawler, J. H. Ingold, L. Bigio, and V. D. Roberts, 1990, Appl. Phys. Lett. **57**, 2416.
Wamsley, R. C., K. Mitsuhashi, and J. E. Lawler, 1993a, Rev. Sci. Instrum. **64**, 45.
Wamsley, R. C., K. Mitsuhashi, and J. E. Lawler, 1993b, Phys. Rev. E **47**, 3540.
Wamsley, R. C., T. R. O'Brian, K. Mitsuhashi, and J. E. Lawler, 1991, Appl. Phys. Lett. **59**, 2947.
Wani, K., 1994, J. Appl. Phys. **75**, 4917.
Wannier, G. H., 1953, Bell Syst. Tech. J. **32**, 170.
Warren, R., 1955, Phys. Rev. **98**, 1658.
Waymouth, J. F., 1959, J. Appl. Phys. **30**, 1404.
Waymouth. J. F., 1971, *Electric Discharge Lamps* (MIT, Cambridge, MA).
Waymouth, J. F., 1982, J. Light Visual Environ. **6** (2), 5.
Waymouth, J. F., 1989, in *Plasma Diagnostics, Volume 1: Discharge Parameters and Chemistry*, edited by O. Auciello and D. L. Flamm (Academic, San Diego), p. 47.
Waymouth, J. F., 1993, in *Microwave Discharges, Fundamentals and Applications*, Vol. 302 of *NATO ASI Series B: Physics*, edited by C. M. Ferreira and M. Moisan (Plenum, New York), p. 427.
Waymouth, J. F., and F. Bitter, 1956, J. Appl. Phys. **27**, 122.
Weibel, E. S., 1967, Phys. Fluids **10**, 741.
Weinmüller, F., 1986, in *Proceedings of the 4th International Symposium on the Science and Technology of Light Sources LS-4*, Karlsruhe, Germany (University of Karlsruhe, Karlsruhe, Germany), p. 243.
Weizel, W., and W. Thouret, 1952, Z. Phys. **131**, 170.
Wharmby, D. O., 1980, Light. Res. Technol. **12**, 221.
Wharmby, D. O., 1986, in *Radiative Processes in Discharge Plasmas*, Vol. 149 of *NATO Advanced Study Institute Series B: Physics*, edited by J. M. Proud and L. H. Luessen (Plenum, New York), p. 327.
Wharmby, D. O., 1993, IEE Proc., Part A: Phys. Sci., Meas. Instrum., Manage. Educ. **140**, 465.
Wharmby, D. O., 1997, in *Lamps and Lighting*, edited by J. R. Coaton and A. M. Marsden (Arnold, London), p. 216.
Wickliffe, M. E., and J. E. Lawler, 1997, J. Opt. Soc. Am. B **14**, 737.
Wickliffe, M. E., J. E. Lawler, and G. Nave, 2000, J. Quant. Spectrosc. Radiat. Transf. **66**, 363.
Winkler, R. B., J. Wilhelm, and R. Winkler, 1983a, Ann. Phys. (N.Y.) **40**, 90.
Winkler, R. B., J. Wilhelm, and R. Winkler, 1983b, Ann. Phys. (N.Y.) **40**, 119.
Yousfi, M., G. Zissis, A. Alkaa, and J. J. Damelincourt, 1990, Phys. Rev. A **42**, 978.
Yuasa, K., K. Yamashina, and T. Sakurai, 1997, Jpn. J. Appl. Phys., Part 1 **36**, 2340.
Zissis, G., P. Bénétruy, and I. Bernat, 1992, Phys. Rev. A **45**, 1135.
Zissis, G., J. J. Damelincourt, and Z. Bezanbary, 2001, *Proceedings of the 2001 IEEE Industry Applications Conference* (IEEE, Piscataway, NJ).
Zollweg, R. J., R. W. Liebermann, and D. K. McLain, 1981, J. Appl. Phys. **52**, 3293.
Zollweg, R. J., J. J. Lowke, and R. W. Liebermann, 1975, J. Appl. Phys. **46**, 3828.
Zubler, E. G., 1988, Ed., *High Temperature Lamp Chemistry II*, Proceedings No. 88-4, Symposium Proceedings of the Electrochemical Society Meeting, Atlanta, May 15–20, 1988.
Zwicker, H., 1968, in *Plasma Diagnostics*, edited by H. Lochte-Holtgreven (Wiley, New York), p. 214.